Imperial College London
Department of Physics

# Terahertz Sensing with Spoof Plasmon Surfaces

Binghao Ng

Submitted in partial fulfilment of the requirements for the degree of
Doctor of Philosophy in Physics and Diploma of Imperial College London
September 2014

*To my wife, Joanne,*

*and our parents*

# DECLARATION OF AUTHORSHIP

I, Binghao Ng, declare that this thesis entitled, "Terahertz Sensing with Spoof Plasmon Surfaces" and the work presented in it are my own. I confirm that:

- This work was done wholly or mainly while in candidature for a research degree at this University.
- Where any part of this thesis has previously been submitted for a degree or any other qualification at this University or any other institution, this has been clearly stated.
- Where I have consulted the published work of others, this is always clearly attributed.
- Where I have quoted from the work of others, the source is always given. With the exception of such quotations, this thesis is entirely my own work.
- I have acknowledged all main sources of help.
- Where the thesis is based on work done by myself jointly with others, I have made clear exactly what was done by others and what I have contributed myself.

Signed: Binghao Ng

Date: 16 September 2014

The copyright of this thesis rests with the author and is made available under a Creative Commons Attribution Non-Commercial No Derivatives licence. Researchers are free to copy, distribute or transmit the thesis on the condition that they attribute it, that they do not use it for commercial purposes and that they do not alter, transform or build upon it. For any reuse or redistribution, researchers must make clear to others the licence terms of this work.

# ACKNOWLEDGEMENTS

I owe a great debt of gratitude to my PhD supervisors Prof. Stefan Maier (Imperial College London), Prof. Minghui Hong (National University of Singapore) and Prof. Yun Fook Liew (A*STAR) for their support and for trusting me to deliver results on my work. I am also grateful to Prof. Norbert Klein for the interesting and inspiring discussions during our meetings.

I would like to thank my friends and colleagues in London and Singapore for their friendship and all the fond memories created during the course of this PhD. In particular, I would like to express my heartfelt thanks to Dr. Stephen Hanham, Dr. Antonio I. Fernández-Domínguez and Dr. Vincenzo Giannini for unreservedly sharing with me their knowledge and experience. And also, I am really fortunate to have been able to enlist the help of Dr. Jianfeng Wu to fabricate the samples for my projects. Without his help, much of the work here would not have been possible.

Lastly, I would like to thank my wife, Joanne, for her unwavering support during the long, and sometimes trying, PhD years. It would not have been possible without her by my side.

# LIST OF PUBLICATIONS

The work presented in this thesis has been published in the following peer-reviewed journal articles:

- **B. Ng**, S. M. Hanham, J. F. Wu, A. I. Fernández-Domínguez, N. Klein, Y. F. Liew, M. B. H. Breese, M. H. Hong and S. A. Maier. "Broadband Terahertz Sensing on Spoof Plasmon Surfaces". ACS Photonics, **1** (2014), 1059.

- **B. Ng**, J. F. Wu, S. M. Hanham, A. I. Fernández-Domínguez, N. Klein, Y. F. Liew, M. B. H. Breese, M. H. Hong and S. A. Maier. "Spoof Plasmon Surfaces: A Novel Platform for THz Sensing". Adv. Opt. Mat., **1** (2013), 543. *Featured in August Issue as Cover Page and "Best of Advanced Optical Materials 2013".*

- **B. Ng**, S. M. Hanham, V. Giannini, Z. C. Chen, M. Tang, Y. F. Liew, N. Klein, M. H. Hong, and S. A. Maier. "Lattice Resonances in Antenna Arrays for Liquid Sensing in the Terahertz Regime". Opt. Express, **19** (2011), 14653.

The results were also reported at the following scientific conferences:

- **B. Ng**, S. M. Hanham, M. H. Hong and S. A. Maier. Narrowband to Broadband Sensing with Spoof Plasmon Surfaces. *Gordon Research Seminars and Conferences on Plasmonics. Oral and Poster Presentation.*

- S. M. Hanham, M. Navarro-Cia, **B. Ng**, H. Aouani, M. Rahmani, N. Klein and S. A. Maier. Exploiting plasmonics for THz and infrared sensing. *Proc. SPIE 9102, Terahertz Physics, Devices, and Systems VIII: Advanced Applications in Industry and Defense*, 91020J (May 21, 2014)

- **B. Ng**, S. M. Hanham, N. Klein, M. H. Hong and S. A. Maier. Broadband Terahertz Sensing on Spoof Plasmon Surfaces. *2014 MRS Spring Meeting, Boston. Poster Presentation.*

- **B. Ng**, J. F. Wu, S. M. Hanham, A. I. Fernández-Domínguez, N. Klein, Y. F. Liew, M. B. H. Breese, M. H. Hong and S. A. Maier. Sensing with Terahertz Spoof Plasmons. *2013 MRS Fall Meeting, Boston. Oral Presentation.*

Other publications (not included in this PhD thesis):

- J. F. Wu, **B. Ng**, H. Liang, M. B. H. Breese, M. H. Hong, S. A. Maier, H. O. Moser and O. Hess "Chiral Metafoils for Terahertz Broadband High-Contrast Flexible Circular Polarizers". Phys. Rev. Appl., **2** (2014), 014005.
- J. F. Wu, **B. Ng**, S. P. Turaga, M. B. H. Breese, S. A. Maier, M. H. Hong, A. A. Bettiol and H. O. Moser "Free-standing Terahertz Chiral Meta-foils Exhibiting Strong Optical Activity and Negative Refractive Index". Appl. Phys. Lett., **103** (2013), 141106.
- Y. G. Chen, T. S. Kao, **B. Ng**, X. Li, X. G. Luo, B. Luk'yanchuk, S. A. Maier and M. H. Hong. "Hybrid Phase-change Plasmonic Crystals for Active Tuning of Lattice Resonances". Opt. Express, **21** (2013), 13691.

# ABSTRACT

Terahertz (THz) radiation ($\approx 0.1-10\times10^{12}$ Hz) is non-ionizing and its photon energies correspond to the rotational and vibrational modes of many complex molecules. Hence many substances of interest for biological and security applications can be detected using THz light; making THz spectroscopy an ideal tool for bio- and security sensing. However, a size mismatch between the photon wavelength and the size of many commonly sensed targets, and a lack of powerful sources hamper the progress of THz technology towards more widespread real-world applications.

The focus of this thesis is to use novel concepts in the field of metamaterials to overcome or side step some of these challenges. In particular, the use of confined electromagnetic surface modes, such as lattice resonances and spoof plasmons, on metamaterial surfaces to conduct THz sensing is investigated. Different ways in which sensing information can be extracted from these specially structured metamaterial surfaces are explored so as to demonstrate the feasibility and versatility of metamaterial surfaces in THz sensing applications.

The application of lattice resonances to detect refractive index changes caused by various fluids on an array of metallic rods is first reported in this thesis. This can be seen as a prelude to the work presented in later chapters where strongly confined spoof plasmons are employed for THz sensing. A metamaterial surface supporting spoof plasmons (simply termed as a Spoof Plasmon Surface (SPS)), consisting of a linear array of metallised sub-wavelength grooves, is filled with various fluids and shown to be capable of high performance refractive index sensing in an Otto prism setup. Sharp phase changes, readily available from THz time-domain spectroscopy (THz-TDS), associated with the coupling of THz radiation to spoof plasmons are used as the readout response in this case to indicate changes in the refractive indices of the fluids filling the grooves. Building upon the initial work on spoof plasmon sensing, further investigations demonstrate the feasibility of SPSs as a versatile

platform on which various forms of sensing information can be extracted by using THz radiation that is coupled in and out of spoof plasmons via the scattering edge coupling scheme. The time-domain signal from the SPS is analysed using a short-time Fourier transform (STFT), enabling the extraction of the broadband spoof plasmon dispersion with a single measurement as well as the attenuation coefficient with a minimum of two measurements. Broadband sensing is demonstrated, again by filling the grooves with various fluids, which results in changes in the spoof plasmon dispersion and attenuation coefficients. In addition, the observation of the absorption peak of $\alpha$-lactose monohydrate at 1.37 THz due to the enhanced light-matter interactions on an SPS is demonstrated and opens the door towards a more spectroscopic approach to THz sensing using SPSs.

# CONTENTS

**Abstract** **vii**

**Contents** **ix**

**List of Figures** **xi**

**List of Tables** **xiii**

**1 Introduction** **1**
1.1 THz Technology: Promises and Challenges . . . . . 1
1.2 Translating Metamaterials Concepts to THz Applications . . . . . 7
1.3 Structure of the PhD program & Thesis . . . . . 14

**2 Theory** **17**
2.1 Introduction . . . . . 17
2.2 Maxwell's Equations . . . . . 17
2.3 Lattice Resonances in Diffractively Coupled Antennas . . . . . 18
2.4 Surface Plasmon Polaritons at Metal-Dielectric Interfaces . . . . . 21
2.5 Coupled Mode Theory of Spoof Plasmon Surfaces . . . . . 25
2.6 Fourier Analysis of Time-Domain Signals . . . . . 34

**3 Refractive Index Sensing via Lattice Resonances** **41**
3.1 Introduction . . . . . 41
3.2 Experimental & Simulation Methods . . . . . 41
3.3 Characteristics of Lattice Resonances . . . . . 44
3.4 Fluid Refractive Index Sensing with Lattice Resonances . . . . . 47
3.5 Evaluating Lattice Resonance Sensing: What Comes Next? . . . . . 52

**4 Spoof Plasmon Surfaces as a Platform for Terahertz Sensing Applications** **55**
4.1 Introduction . . . . . 55
4.2 Spoof Plasmons on a Linear Array of Subwavelength Grooves . . . . . 56
4.3 Optical Lithography of Metallized Sub-wavelength Groove Arrays . . 58
4.4 Otto Prism Coupling to Spoof Plasmons . . . . . 60
4.5 Narrowband Refractive Index Sensing on the SPS . . . . . 66
4.6 Narrowband Data: Surely this can't be all? . . . . . 75

**5 Broadband Sensing with Spoof Plasmon Surfaces 77**
5.1 Introduction . . . 77
5.2 SPS Description & Bandstructure Calculation . . . 78
5.3 Scattering Edge Coupling to Spoof Plasmons . . . 79
5.4 Extracting Spoof Plasmon Dispersion Relations . . . 85
5.5 Broadband Refractive Index Sensing . . . 89
5.6 THz Surface-enhanced Absorption Spectroscopy . . . 96
5.7 Spoof Plasmon Sensing: Are we there yet? . . . 100

**6 Conclusions & Future Work 103**

**Bibliography 109**

**Appendix A THz Time-Domain Spectroscopy: A Short Overview 121**
A.1 Introduction . . . 121
A.2 Basic Operating Principles . . . 121
A.3 Quasi-Optical Terahertz Time-Domain Spectrometer . . . 125
A.4 Teraview Spectra 3000 . . . 126

**Appendix B Simulation Methods 129**
B.1 Introduction . . . 129
B.2 Finite-Difference Time-Domain . . . 129
B.3 Finite-Element Analysis . . . 131
B.4 Analytical Approach . . . 132

**Appendix C Advanced Optical Materials Vol. 1 August Issue Cover Page 135**

# LIST OF FIGURES


1.1 Security applications of THz radiation . . . . . 2
1.2 Diagram illustrating interesting bio-chemical signatures in THz regime . 3
1.3 Examples of THz biochemical sensing . . . . . 4
1.4 Comparing metamaterials and real materials . . . . . 8
1.5 An example of a complicated 3D metamaterial structure . . . . . 10
1.6 Examples of lattice resonances in diffractively coupled antenna array . . 13
1.7 Example of Spoof Plasmon Surface . . . . . 14
1.8 Mindmap of PhD work . . . . . 16

2.1 Physical interpretation of lattice resonances . . . . . 19
2.2 SPP dispersion relation . . . . . 22
2.3 Sketch of Couple Mode Method system . . . . . 26
2.4 Unit cell of an array of subwavelength grooves . . . . . 32
2.5 Analytical Spoof Plasmon Dispersion . . . . . 33
2.6 Fourier series decomposition of a square wave. . . . . 35
2.7 Explanation of short-time Fourier transform . . . . . 39

3.1 THz antenna schematic and sensing configuration . . . . . 43
3.2 THz antennas in a homogeneous environment . . . . . 45
3.3 Fluid refractive index sensing with lattice resonances . . . . . 49
3.4 Electric field distribution of guided modes and lattice resonance . . . . . 50
3.5 Lattice resonance shift, $\Delta\lambda_{res}$ plotted against the refractive index $n_{res}$ . . 52

4.1 Analytical & Simulated spoof plasmon dispersion relations . . . . . 57
4.2 Confinement length $L_z$, of spoof plasmons on square PEC grooves . . . . 59
4.3 Schematic diagram and optical microscope image of SPS . . . . . 60
4.4 Spoof plasmon dispersion of square and slanted-wall PEC grooves . . . . 61
4.5 Otto prism coupling configuration and reflection spectra at various $g$ . . 62
4.6 Phase jumps at resonant coupling to spoof plasmons . . . . . 65
4.7 Calculated spoof plasmon dispersion relations for the various fluids . . . 67
4.8 Reflection spectra of various fluids filling SPS grooves . . . . . 69
4.9 Phase change spectra for the various fluids . . . . . 70
4.10 Phase jump spectra of various fluids filling SPS grooves . . . . . 71
4.11 Resonance frequencies of various fluids $f_{sp}$, plotted against refractive indices 72

5.1 SPS design and bandstructure . . . . . 78
5.2 Scattering edge coupling to spoof plasmons . . . . . 80

5.3 Effect of time-frequency filtering . . . . . 84
5.4 Spectrogram at various $D$ . . . . . 85
5.5 Schematic description of dispersion extraction . . . . . 86
5.6 Extracted broadband SPS dispersion . . . . . 89
5.7 Refractive indices of fluids used . . . . . 90
5.8 Spoof plasmon dispersion relation of various fluids . . . . . 91
5.9 Spoof plasmon attenuation of various fluids . . . . . 93
5.10 Absorption spectrum of $\alpha$-lactose monohydrate . . . . . 97
5.11 Normalised spectrogram of lactose powder on the SPS . . . . . 98
5.12 Spoof plasmon detection of $\alpha$-lactose monohydrate powder . . . . . 99

6.1 Alternative spoof plasmon excitation methods . . . . . 106
6.2 Concept drawing of SPS sensor incorporated with microfluidic channels . 107
6.3 Schematic of SPS interferometer . . . . . 108

A.1 Schematic diagram of THz-TDS . . . . . 122
A.2 Photoconductive Antenna . . . . . 123
A.3 THz light emission and detection . . . . . 124
A.4 Photograph of the quasi-optical THz-TDS . . . . . 125
A.5 Typical Signal from Quasi-optical THz-TDS . . . . . 126
A.6 Photo of Teraview Spectra 3000 . . . . . 127

B.1 Example of staircase mesh . . . . . 130
B.2 Example of triangular mesh . . . . . 132

# LIST OF TABLES

3.1 Table of lattice resonance wavelength $\lambda_{res}$, and corresponding refractive index $n_{res}$ . . . . . 51

4.1 Table of calculated and experiment $f_{sp}$ for the various fluids . . . . . 68
4.2 Summary of Figure-of-Merits for the various fluids tested. . . . . 73

CHAPTER 1

# INTRODUCTION

## 1.1 TERAHERTZ TECHNOLOGY: PROMISES AND CHALLENGES

Terahertz (THz) or sub-millimetre radiation is loosely defined as electromagnetic waves with frequencies from $0.1 \times 10^{12}$ Hz to $10 \times 10^{12}$ Hz and has an equivalent blackbody temperature of roughly 5 K to 464 K. Consequently, THz spectroscopy has traditionally been used in the field of astronomy as much of the light from the Big Bang has cooled into the sub-millimetre frequency band and many important chemical species such as water and oxygen have their thermal emission peaks or first rotational or vibrational line emissions in the low THz regime. For example, astronomers have used the radiation from interstellar dust to study the early universe as well as for atmospheric observations [1–3].

In recent years, researchers have also been interested in other applications of THz radiation. High speed wireless communications is one major area of growth in an attempt to satiate the ever burgeoning demand for higher data transfer rates needed for high definition media content streaming and the increasing number of mobile technology users [4, 5]. Another area of focus for THz research is standoff imaging for security applications owing to the ability of THz radiation to penetrate common materials such as fabric and paper as well as the existence of spectral fingerprints of many materials of interest at THz frequencies [6–9]. Looking at Fig. 1.1 (a), we can see that THz radiation is capable of penetrating clothes, revealing a concealed knife due to the high reflectivity of metals to low frequency light [6]. Another example is shown by Kawase *et al.* [10] in Fig. 1.1(b), where the spectral fingerprints of complex molecules in the THz regime is used to identify illicit drugs concealed in an envelope.

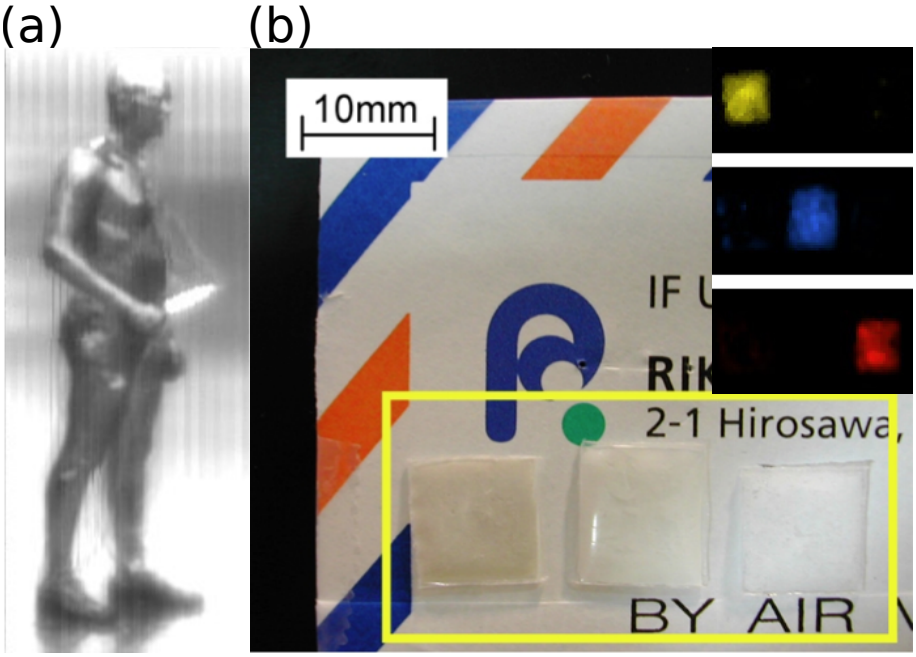



Figure 1.1: (a) THz image of a man concealing a knife. Reprinted with permission from [6]. Copyright 2007, IEEE. (b) THz spectral imaging of illicit drugs such as methamphetamine concealed in an envelope. (Inset) Artificially coloured spectral image of the concealed drugs demonstrating the ability of THz radiation to differentiate between drugs. Reprinted with permission from [10]. Copyright 2003, OSA.

The idea of using THz light to uniquely identify substances as shown in Ref. [10] leads us to consider an area of research in which THz technology shows immense promise: bio-chemical sensing. There are two main reasons why bio-chemical sensing is advantageous at THz frequencies. Firstly, THz radiation is non-ionising, owing to its low photon energies. This means that samples probed by THz light can then be passed on to other sensing or detection methods such as Fourier Transform Infrared Spectroscopy (FTIR) or ultra-violet - visible (UV-VIS) spectroscopy to gain complete information about the substance over a broad band of frequencies.

Secondly, many complex molecules have unique interactions with light at THz frequencies such as molecular rotations, low frequency phonons, collective vibrational modes and molecule conformational modes as illustrated in Fig. 1.2. Hence, THz radiation allows us not only to uniquely identify certain biochemical substances but

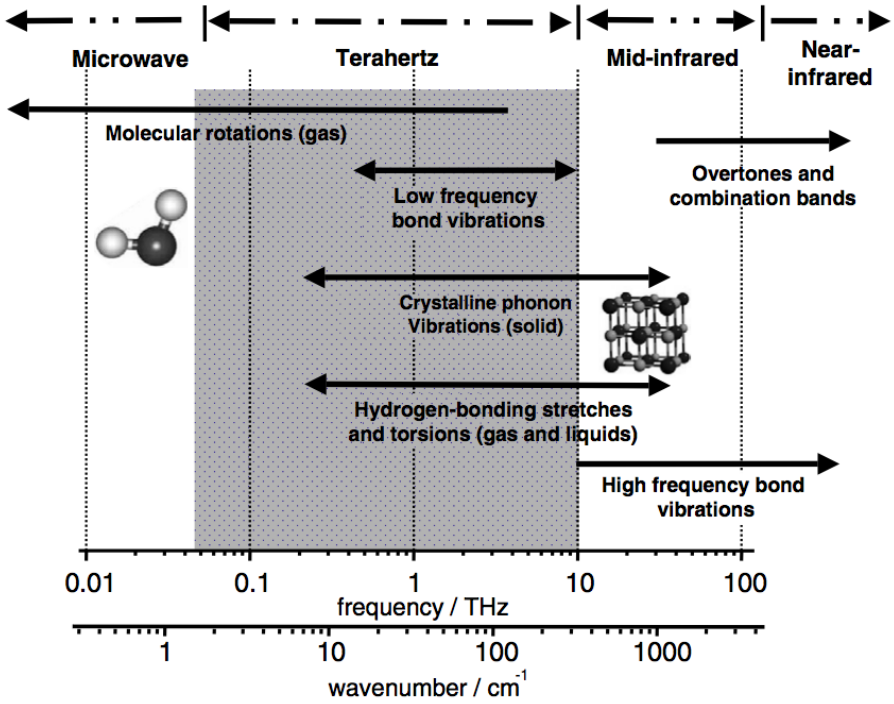



Figure 1.2: Diagram illustrating interesting bio-chemical signatures in the THz regime. Reprinted with permission from [11]. Copyright 2006, IOP Publishing.

also to study their physical structure and intra- and inter-molecular interactions as exemplified by the following examples. Figure 1.3(a) shows the THz absorption spectra of water vapour at various humidity levels [12]. The sharp absorption peaks are due to mainly to rotational modes of the water molecule in vapour form. In general, water itself has been widely studied due to its ubiquitous nature and its importance in various settings ranging from atmospheric observations to biological systems [12–17]. Fig. 1.3(b) shows the absorbance spectra of the photoactive protein bacteriorhodopsin and shows how the THz absorption of the protein can change in response to a change from its rest state (green line) to the M state (blue line) which is associated with a conformational change in the protein [15,18]. At the same time, Markelz also highlighted, in Refs. [18,19], the use of THz spectroscopy to study the optical responses of DNA and proteins to changes in environmental conditions like temperature and hydration levels, and structural changes of the biological

sample itself like the denaturing of DNA. Figure 1.3(c) shows spectral signatures of double-stranded, small-interfering RNA stretched through a nanofluidic channel demonstrated by Brown *et al.* [20]. The last example raised is that of lactose which is a common excipient in the pharmaceutical industry [11]. In Fig. 1.3(d) which shows the absorption spectra of $\alpha$-lactose monohydrate (dashed line) and anhydrous $\alpha$-lactose (black line), one can clearly see the differences between the two different forms of $\alpha$-lactose. This is important as the final form of the ingredients present in drugs can affect drug performance [21].

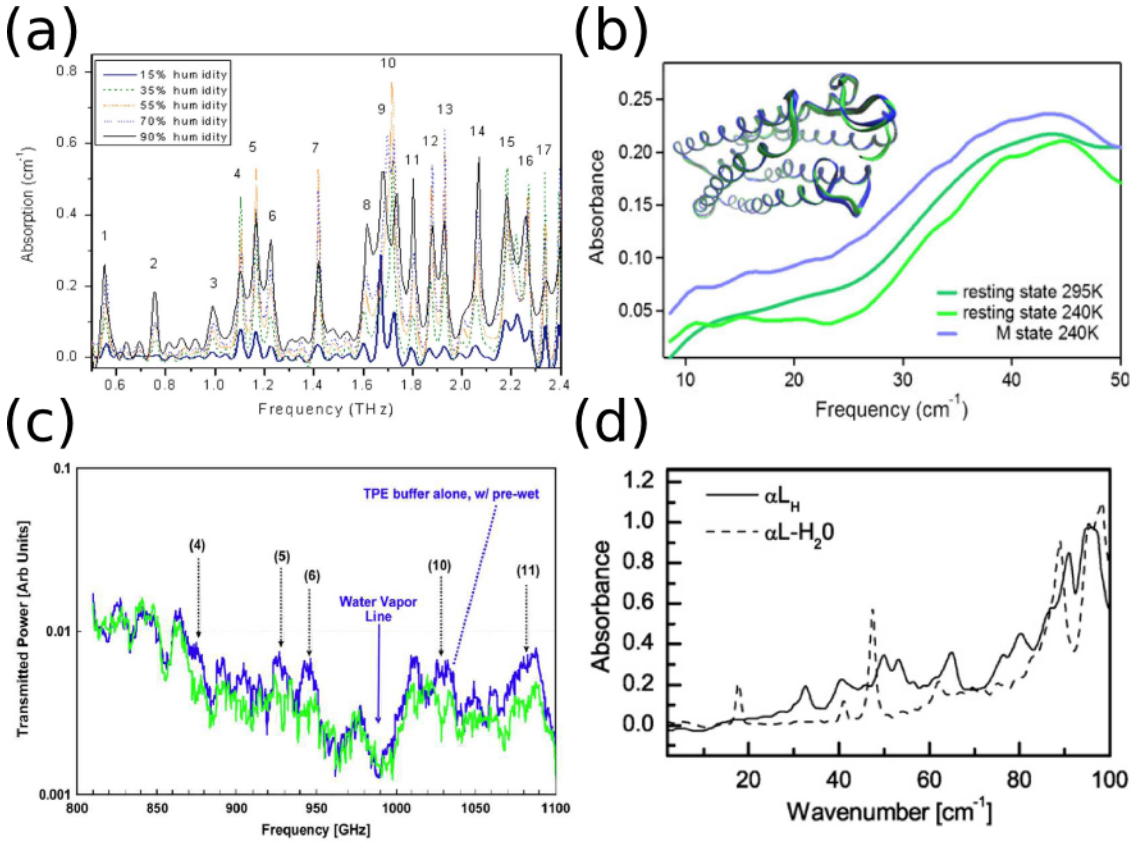



Figure 1.3: (a)Absorbance spectra of water vapour at various humidity levels. Reprinted with permission from [12]. Copyright 2006, AIP Publishing LLC. (b) Absorbance spectra of the photoactive protein bacteriorhodopsin. Reprinted with permission from [15]. Copyright 2012, Springer. (c) Transmission spectrum of RNA stretched through nanofluidic channels showing several spectral peaks. Reprinted with permission from [20]. Copyright 2010, IEEE. (d) Absorbance spectra of $\alpha$-lactose monohydrate and anhydrous $\alpha$-lactose. Reprinted with permission from [22]. Copyright 2007, Elsevier.

THz spectroscopy has also been used to study a wide variety of substances such as saccharides [23–25], polar liquids [26], drugs [27], explosives [6, 8, 28], oils [29–31] and even skin [32, 33]. It is impossible to comprehensively cover the huge body of work done on using THz radiation for biological and chemical studies. Nonetheless, we can see from the examples cited above how THz radiation can be harnessed to complement current characterisation technologies for biochemical sensing as well as have a palpable impact in commercial settings such as drug production.[1]

The logical question to ask then is, why is THz spectroscopy not more widely used in real-world sensing applications? One of the main reasons for this is the lack of convenient yet powerful THz sources. This has led to a lack of signal-to-noise ratio in sensing experiments involving biological systems consisting of an aqueous environment which is extremely absorbing due to its polar nature [3]. The most common form of THz generation is that of pulsed laser excitation of photoconductive antennas on semiconductor substrates which result in a picosecond electromagnetic pulse with a Fourier counterpart in the THz (see Appendix A). However pulsed laser excitation of photoconductive antennas can only generate up to microwatts of power [40]. Other THz sources include free electron lasers and synchrotrons [41]. However these sources, though high powered, are costly and, not to mention, the size of a small building.

The problem of the lack of powerful yet convenient sources is somewhat alleviated with the development of quantum cascade lasers (QCLs) [42, 43], photomixing techniques [44, 45] and nonlinear frequency difference THz sources [46]. However, challenges remain. For example, QCLs are capable of emitting THz radiation up to milliwatt power levels but they require liquid nitrogen cooling. Moreover, QCLs are narrowband sources and hence are not suited for spectroscopic purposes. THz generation via photomixing allows for better spectral power density but it is a frequency domain technique and is unable to capture time-domain data like a THz

[1] For extensive reviews, see [11, 15, 18, 21, 34–39].

time-domain spectrometer (THz-TDS) which is useful for studying carrier and solvation dynamics [47, 48]. Even then, the power generated by photomixing is often only in the tens of microwatts and often does not have the bandwidth of a THz-TDS. Nonlinear frequency difference THz generation is capable of tens of milliwatts of THz power but again shares the same drawbacks as other frequency domain techniques such as photomixing [46].

To side-step the problem of the lack of strong sources, especially in the case of probing strongly absorbing aqueous biological systems, researchers have tried to reduce the sample volumes to increase the signal-to-noise ratio. However this immediately leads us to another problem which is the lack of light-matter interaction due to a length scale mismatch between the photon wavelength and the sample size/volume. In general, cell sizes are on the order of tens of microns and biological species such as proteins are even smaller [49]. On top of that, microfluidic channels or very thin cuvettes on the order of a few tens of microns are used to not only limit the amount of absorption that results from the water environment suspending the biological substance but also due to the fact that the samples, especially in a practical setting, are available only in small amounts. All this means that in a traditional transmission spectroscopy scenario, the overall typical sample length is very small compared to the free space wavelength.

Efforts have again been made to side-step this issue by probing the biological samples embedded in polyethylene powder matrices [18] or using attenuated total reflection (ATR) spectroscopy [50, 51]. But they too present problems. For example, embedding biological substances in polyethylene matrices means that they are no longer in their natural environment. ATR spectroscopy allows for the probing of samples via localised evanescent waves but it does not offer the opportunity to tailor optical responses to specific applications like metamaterials as the confinement depends solely on the refractive index of the prism used.

An alternative perspective can be taken with regards to the lack of THz power and the length scale mismatch between THz wavelengths and typical sample sizes. Instead of trying to increase the amount of power at our disposal, we can take steps to make better use of the power we already have. For example, one way to counter the problem of sensing small volume samples would be to confine the THz light to small volumes so as to increase light-matter interactions. In this way, we would no longer need to rely on conventional methods, such as transmission/reflection spectroscopy [11–15] and ATR spectroscopy [16, 50, 51], which are the main sensing techniques used in previously reported work. This can be achieved with the help of metamaterials as we shall see in the next section.

## 1.2 TRANSLATING METAMATERIALS CONCEPTS TO THZ APPLICATIONS

A *metamaterial* can be described as a *collection* of constituent elements much smaller than the incident wavelength of light which has *bulk* optical properties as a result of the *structure* of the individual elements rather than the *material* from which the elements are made. To highlight the similarities and differences between a metamaterial and a normal material, we have to first look at materials in the way we usually know it.

A normal bulk material is an ordered (crystalline) or disordered (amorphous) collection of atoms. This is depicted in Fig. 1.4. The bulk optical properties are then determined by the aggregate response of all the atoms to light as well as their arrangement. In the case of dielectrics, the polarisability of the atoms are responsible for the dielectric constant of the material. In metals, the number of free electrons in the conduction band will determine the plasma frequency of the metal, which in turn affects the way the metal responds to light. And also, if the atoms are placed in an ordered array, i.e. in a crystal lattice, that will lead to the formation of band structure and the existence of optically active phonons that will also change the way the material responds to light. In short, it is the *nature* of the constituent atoms that

determines the overall optical properties of the material. But as the wavelength of light is much greater than the size of the atoms, any incident light does not interact with each individual atoms but with the material as a whole (classically speaking of course).

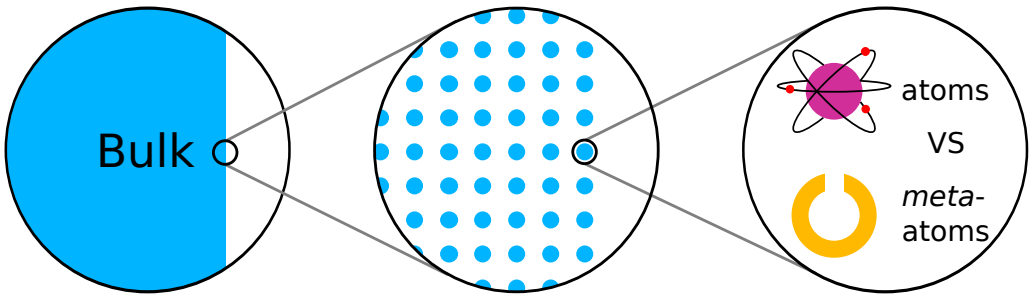



Figure 1.4: Comparing metamaterials and real materials

With the advent of micro- and nano-fabrication technology, we are now able to define structures that are much smaller than the wavelength of light with very high quality. This is especially true at THz frequencies where the photon wavelengths are of the order of hundreds of microns. What this means is that researchers can now think about actually *replacing* the actual atoms with *meta-atoms*, which are sub-wavelength structures that interact in an engineered fashion with light as depicted in Fig. 1.4. This in turn would lead to an overall optical response of the collection of meta-atoms which is determined by the structure of the meta-atom itself. At the core of the idea of metamaterials is the notion that the way light interacts with its surroundings can be designed using an *effective refractive index* which is achieved via careful engineering of the meta-atoms. In a way, this has allowed researchers to unleash their imagination and consider refractive index regimes, such as negative refractive indices, that were thought impossible as well as to come up with creative ways to control light.

The beginnings of the field of metamaterials is widely attributed to Prof. Sir John Pendry and a group of his peers in the late 1990's, where they showed that the

optical properties of an array of specially structured elements can be effectively engineered depending on the geometrical properties of the individual elements and that the entire phenomenon can be easily understood in terms of effective material properties such as an effective refractive index [52–55]. Since then, there has been an explosion in metamaterials research interest due to the possibility of manifesting exotic optical phenomena and the empowerment of researchers to engineer optical behaviour according to their needs. The first of such optical phenomena is negative refractive index which is achieved when both the effective permittivity and effective permeability of the metamaterial are negative [56–61]. This had led to investigations in reversed Cherenkov radiation [62,63] and perfect lenses [55,64,65]. Although the idea of negative refractive indices was conceived as early as 1968 by Veselago [66], it did not gain traction as such negative refractive index materials did not exist in nature. It was only with the advent of metamaterials that researchers were able to realise negative refractive index. The ability to explore refractive index regimes non-existent in nature has also led researchers to consider metamaterials with an effective permittivity equal to or near zero which can act as optical conduits or elements in optical circuitry [67–71]. Taking the engineering of optical properties even further, researchers were even able to design a spatial distribution of refractive index to constitute optical cloaks, a device of science fiction and fairytales [72–76].

Metamaterials are very well placed to help address problems in THz technology such as those mentioned in the previous section. First of all, micro-fabrication which has reached an extremely mature stage of development is very capable of manufacturing high quality sub-wavelength structures that serve as meta-atoms in metamaterials. This allows researchers to be very creative in designing structures to manifest a desired optical response such as the complicated 3D micro-structures shown in Fig. 1.5 [77, 78]. Secondly, the ability to freely engineer the optical response of metamaterials has led to a huge amount of research on THz components such as tuneable modulators [79–82], optical filters with a chiral response [78,83–85], flexible

metamaterials that can be conformed to non-planar geometries [86–89], metamaterials with very sharp resonances [90, 91] and much more.

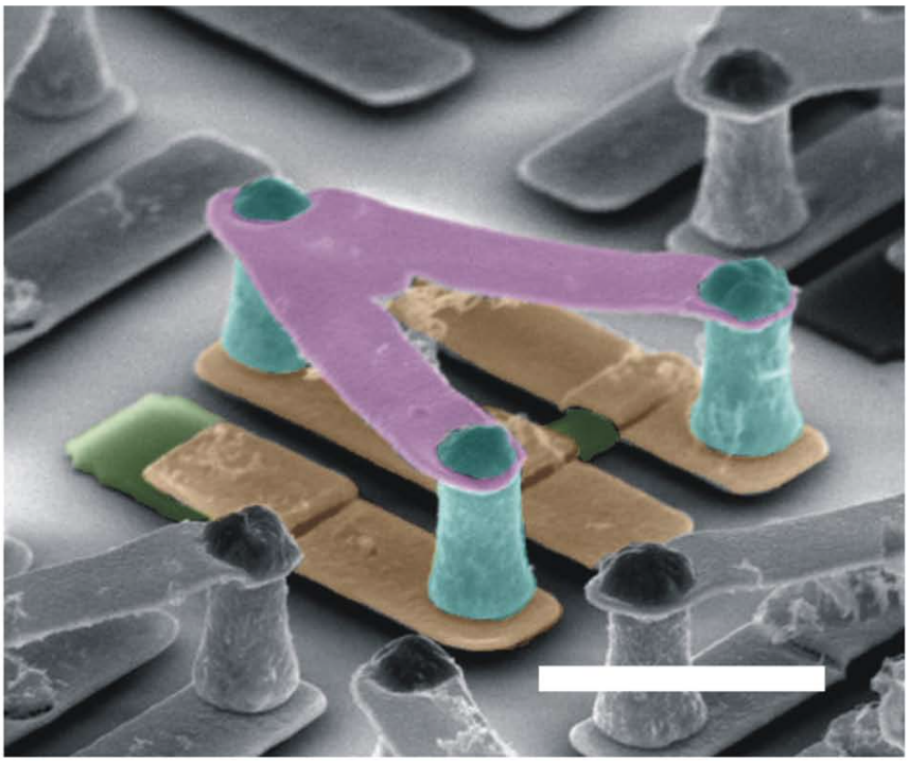


Figure 1.5: An example of a complicated 3D metamaterial structure. Reprinted with permission from [78]. Copyright 2012, Nature Publishing Group.

The opportunity to apply metamaterials to conduct THz refractive index sensing did not go unnoticed by researchers as well where extremely strong field enhancements at specific locations on the meta-atoms make the optical response of the metamaterial very sensitive to dielectric changes at those locations [92, 93]. Sadly, the work conducted on THz metamaterial sensing is not as varied as the research done to try to use metamaterials as THz optical components; thus far it has been focussed solely on utilising localised hot spots in resonant structures as the sensing mechanism and on detecting simple refractive changes [92] or thin film layers [93, 94]. As shall be seen in the rest of this thesis, we take THz metamaterials sensing one step further by considering the use of confined surface waves on THz metamaterial surfaces for sensing. Particularly, the use of surface wave will expand the sensing region beyond

that of localised spots on resonant structures and increase the interaction between the EM fields and the analytes. Moreover, at the end of this thesis, it will be shown how metamaterials supporting strongly confined surface waves could potentially be used to take a more spectroscopic approach to THz sensing by detecting spectral fingerprints of materials instead of simply detecting refractive index changes.

It is easy to notice the overlap in ideas and approaches between metamaterials research in the visible and THz frequency regimes. This is because Maxwell's equations scale with frequency. For example, the study of Fano resonances in the visible regime [95–98] has led to corresponding studies in the THz [91, 99, 100]. The only thing that is not constant over the two frequency ranges are material properties. Whereas metals exhibit plasmonic properties in the visible regime, in THz metals behave much like perfect electrical conductors (PECs) which do not support strongly confined surface waves. Even so, plasmonic properties can be manifested at THz frequencies using semiconductors such as InSb [101, 102]. This leads us to consider how metamaterial concepts in the visible can be borrowed to solve problems in THz sensing, just as metamaterials has led to the design of novel THz optical components as previously illustrated. For the purpose of this thesis, two ideas in metamaterials research are pertinent and during the course of this thesis the translation of these ideas to THz frequencies and their application to address challenges to THz sensing will be shown.

The first is that of lattice resonances via diffractively coupled antennas which are first explored by Markel [103, 104] and Zou *et al.* [105]. Basically, such lattice resonances are a result of the reinforcement of the individual antenna resonances by light scattered from neighbouring antennas in an array and can be thought of as a surface wave propagating in the plane of the antennas. The theory behind this is briefly explained in Section 2.3. This idea is further explored in [106–109] at visible frequencies. In Ref. [106], sharp lattice resonances are shown to exist in nano parti-

cle arrays and are tuneable via a change in the spacings between the nano particles as shown in Fig. 1.6(a). Vecchi *et al.* subsequently showed that the fluorescence emission of a photoactive molecule can be enhanced due to the lattice resonance acting as an effective decay pathway for the molecule, indicating that the EM fields at lattice resonance frequencies interact strongly with the dielectric environment of the antenna array [108]. The top left panel of Fig. 1.6(b) shows the fluorescence enhancement of the photoactive molecule at various excitation angles. As can be seen, the maximum enhancements occur when the lattice resonances are present (see top right panel, Fig. 1.6(b)). The bottom panel of Fig. 1.6(b) shows the fluorescence enhancements at specific excitation angles and enhancements as large as seven times were observed. This is attributed to the de-localised nature of the lattice resonance which allows light to interact with more of the photoactive molecules as compared to when only localised antenna resonances are used to enhance excitations, according to Vecchi *et al.*. In Chapter 3, we show how the de-localised and tuneable nature of lattice resonances can be exploited to conduct refractive index sensing in the THz regime.

The second important piece of metamaterials research is that of spoof plasmons. Work on spoof plasmons began initially with investigations on extraordinary optical transmission (EOT) where it was found that light transmission through periodically perforated metal films was much larger than expected [110]. It was subsequently discovered that EOT is strongly mediated by electromagnetic surface modes propagating on the structured metallic surfaces [111–115]. Researchers then went on to study in detail the nature of the surface modes and show that strongly confined surface waves can even be supported on corrugated PEC surfaces [116–120]. These electromagnetic surface modes on corrugated metallic surfaces are coined *spoof* or *designer* plasmons for their tuneable dispersion relation with respect to geometrical parameters as well as the resemblance of the dispersion relation to that of conventional surface plasmon polaritons (SPPs) in the visible regime. For example, in an

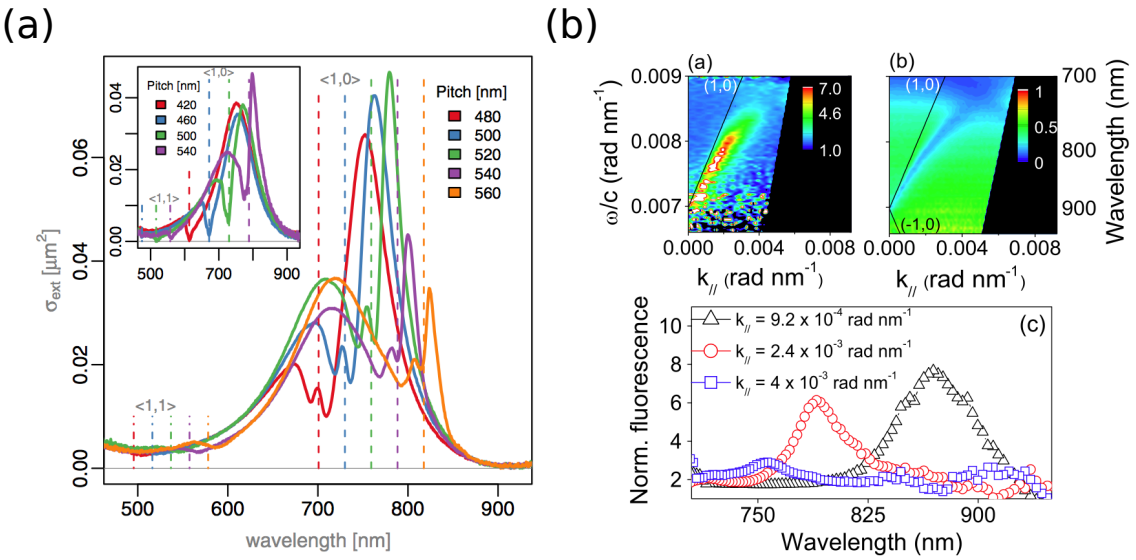



Figure 1.6: (a) Example of lattice resonance tuning via changing the periodicity of the antenna array. Reprinted with permission from [106]. Copyright 2008, American Physical Society. (b) Enhancement of fluorescence emission via lattice resonances as demonstrated by [108]. (Top left panel) Fluorescence enhancement at various excitation frequencies and angles. (Top right panel) Dispersion diagram of lattice resonance. (Bottom panel) Fluorescence enhancements at specific incident angles. Reprinted with permission from [108]. Copyright 2009, American Physical Society.

experiment done by Hibbins *et al.* at GHz frequencies [121], it was shown that a periodic array of subwavelength PEC holes depicted in Fig. 1.7(a) supports spoof plasmons with dispersion given in Fig. 1.7(b).

The sharp deviation of the dispersion relation from the light line implies strong field confinement and is evidenced by the calculated field distribution of the spoof plasmons in Fig. 1.7(c). Such confinement of fields is not possible on flat metal-dielectric interfaces at low frequencies such as THz as only unconfined Sommerfield-Zenneck waves can propagate [122], and is a result of the design of subwavelength corrugations on the metal surface. The ability to freely engineer the surface dispersion relation led to a great deal of experimental and theoretical work investigating the properties of spoof plasmons supported by corrugated metallic surfaces of various geometries for their wave guiding capabilities [123–133]. Such structured surfaces supporting surface waves are also known as slow wave antennas and have been

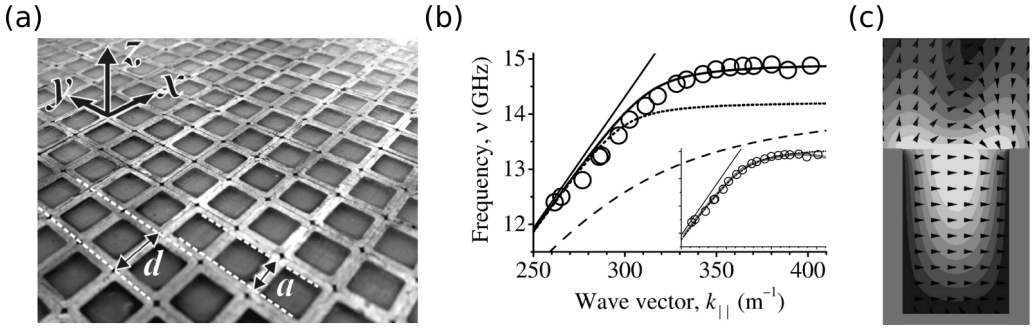



Figure 1.7: (a) A photograph and (b) the dispersion relation of a corrugated PEC surface consisting of a periodic array of subwavelength holes supporting spoof plasmons. (c)Field distribution around the grooves due to spoof plasmons. Reprinted with permission from [121]. Copyright 2008, OSA.

studied in microwave engineering under the transmission line framework [134, 135]. In Chapters 4 and 5, we will describe how the field confinements enable by spoof plasmons allows us to better utilise the limited power of current THz sources and increase light-matter interactions for sensing applications.

## 1.3 STRUCTURE OF THE PHD PROGRAM & THESIS

This PhD was sponsored by the Agency of Science, Technology and Research, A*STAR in Singapore and conducted under the A*STAR-Imperial Program (AIP) where work was conducted in Singapore as well as the United Kingdom. This enabled the utilisation of equipment and and expertise at both A*STAR and Imperial College London. The fabrication of samples was done mainly in A*STAR while the simulations and characterisation were performed in Imperial College London.

The focus of this thesis is to use novel concepts in the field of metamaterials to address some of the challenges of THz research. In particular, the use of confined electromagnetic surface modes, such as lattice resonances and spoof plasmons, on metamaterial surfaces to conduct THz sensing is investigated. Different ways in which sensing information can be extracted from these specially structured metamaterial surfaces are explored so as to demonstrate the feasibility and versatility of

metamaterial surfaces in THz sensing applications.

In the first two chapters, the background and motivations under which the research work is carried out as well as the basic theory concepts are introduced. Chapter 3 describes the application of lattice resonances to detect refractive index changes caused by various fluids on an array of metallic rods. This can be seen as a prelude to the work presented in Chapters 4 and 5, which detail the use of strongly confined spoof plasmons for THz sensing. In Chapter 4, a metamaterial surface supporting spoof plasmons (simply termed as a Spoof Plasmon Surface (SPS)), consisting of a linear array of metallised sub-wavelength grooves which are filled with various fluids, is shown to be capable of high performance refractive index sensing in an Otto prism setup. Sharp phase changes, readily available from THz-TDS, associated with the coupling of THz radiation to spoof plasmons are used as the readout response in this case to indicate changes in the refractive indices of the fluids filling the grooves. Building upon the work in Chapter 4, Chapter 5 further demonstrates the feasibility of SPSs as a versatile platform on which various forms of sensing information can be extracted. THz radiation is coupled in and out of spoof plasmons using the scattering edge coupling scheme. The time-domain signal from the SPS is analyzed using short-time Fourier transform (STFT), enabling the extraction of the broadband spoof plasmon dispersion with a single measurement as well as the attenuation coefficient with a minimum of two measurements. Broadband sensing is demonstrated again by filling the grooves with various fluids, which results in changes in the spoof plasmon dispersion and attenuation coefficients. Additionally, a proof-of-concept demonstration of THz surface-enhanced absorption spectroscopy is shown using $\alpha$-lactose monohydrate powder deposited on the SPS. In Chapter 6, the thesis is concluded with a summary of results and a short description of the future work that can be done.

The work carried out is represented in the mind map shown in Fig. 1.8.

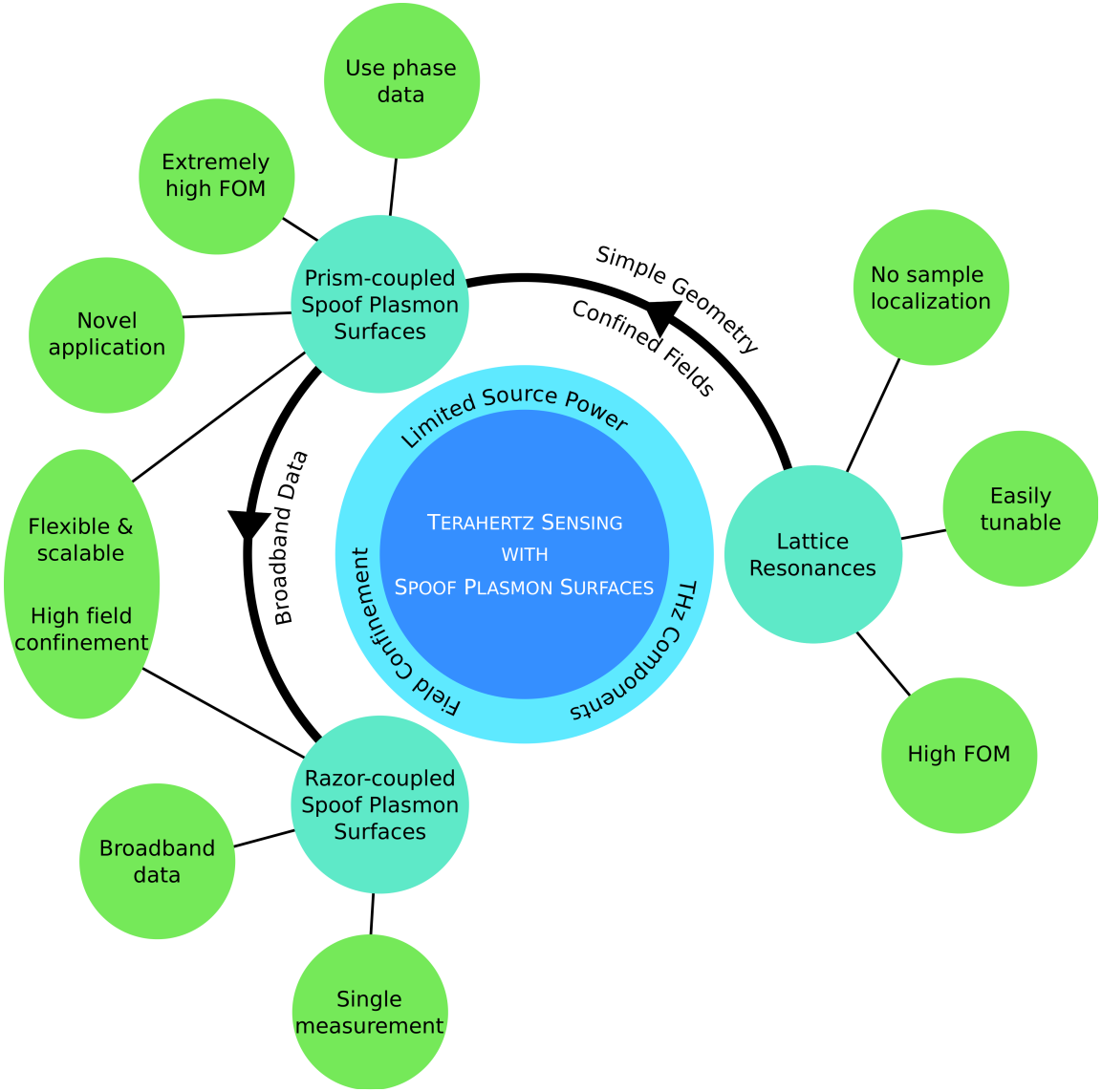



Figure 1.8: Mindmap of PhD work

CHAPTER 2

# THEORY

## 2.1 INTRODUCTION

The main branches of theory relevant to this thesis are outlined in this chapter. First, we start with Maxwell's equations followed by a description of lattice resonances mediated by diffractively coupled dipoles, relevant to work presented in Chapter 3. A brief introduction to surface plasmon polaritons (SPPs) on metal-dielectric interfaces which leads to a coupled mode description of spoof plasmons on corrugated metallic surfaces is then given. This provides the theoretical framework upon which the work in Chapters 4 and 5 is built. Lastly, Fourier transform, used everywhere in the thesis to process data from the THz-TDS, is described. SI units are used throughout this thesis.

## 2.2 MAXWELL'S EQUATIONS

Classical electrodynamics is governed by the Maxwell's equations [136],

$$\nabla \cdot \mathbf{D} = \rho_f, \tag{2.1}$$

$$\nabla \cdot \mathbf{B} = 0, \tag{2.2}$$

$$\nabla \times \mathbf{E} = -\frac{\partial \mathbf{B}}{\partial t}, \tag{2.3}$$

$$\nabla \times \mathbf{H} = \mathbf{j}_f + \frac{\partial \mathbf{D}}{\partial t}, \tag{2.4}$$

where $\mathbf{E}$ and $\mathbf{B}$ are the vector electric field and magnetic flux density, respectively, $\rho_f$ is the free charge density and $\mathbf{j}_f$ is the free charge current density.

$\mathbf{D}$ and $\mathbf{H}$ are the electric displacement and magnetic fields, respectively, and are

related to $\mathbf{E}$ and $\mathbf{B}$ by the constitutive relations,

$$\mathbf{D} = \epsilon_r \epsilon_0 \mathbf{E}, \tag{2.5}$$

$$\mathbf{B} = \mu_r \mu_0 \mathbf{H}, \tag{2.6}$$

where $\epsilon_0$ and $\mu_0$ are the permittivity and permeability of free space and $\epsilon_r$ and $\mu_r$ are the relative permittivity and permeability of the material.

The boundary conditions required to solve the above differential equations are simply that the components of $\mathbf{E}$ and $\mathbf{H}$ tangential to an interface between two media, let's say $i$ and $j$, are continuous across the interface. This can be straightforwardly written as,

$$\mathbf{n} \times (\mathbf{E}_i - \mathbf{E}_j) = 0, \tag{2.7}$$

$$\mathbf{n} \times (\mathbf{H}_i - \mathbf{H}_j) = 0, \tag{2.8}$$

where $\mathbf{n}$ is the unit vector normal to the interface between the two media and $\mathbf{E}_i$ and $\mathbf{H}_i$ ($\mathbf{E}_j$ and $\mathbf{H}_j$) are the electric and magnetic fields in media $i$ (media $j$), respectively. It is also assumed that $\mathbf{j}_f = 0$, which is valid for dielectrics.

Using Equations (2.1) to (2.4) the Helmholtz equations, which describe the propagation of electromagnetic waves in a homogeneous, linear and isotropic media with optical constants $\epsilon_r$ and $\mu_r$ can be derived to give,

$$\left(\nabla^2 - \epsilon_0 \epsilon_r \mu_0 \mu_r \frac{\partial^2}{\partial t^2}\right) \mathbf{E} = 0, \tag{2.9}$$

$$\left(\nabla^2 - \epsilon_0 \epsilon_r \mu_0 \mu_r \frac{\partial^2}{\partial t^2}\right) \mathbf{B} = 0, \tag{2.10}$$

where $\nabla^2$ is the Laplace operator and $\rho_f$ and $\mathbf{j}_f$ are assumed to be zero.

## 2.3 LATTICE RESONANCES IN DIFFRACTIVELY COUPLED ANTENNAS

Consider a periodic 1D chain of dipole-like spheres in vacuum with radius $a$, and lattice constant $P$, illuminated normally by light polarized in a direction perpendicular to the chain axis, as shown in the top panel of Fig. 2.1.

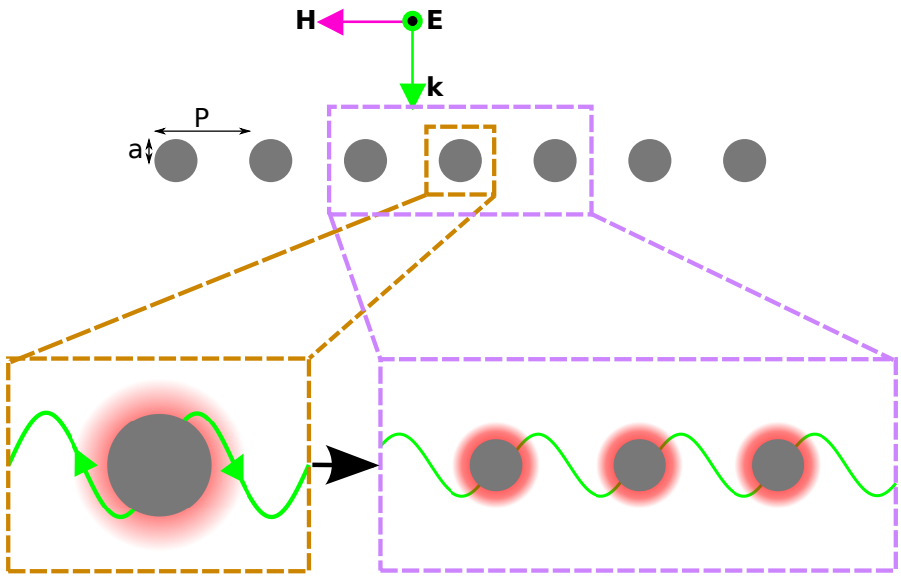



Figure 2.1: (Top panel) Schematic of particle chain with particle radius, $a$, and lattice constant, $P$. (Bottom left panel, orange box) Each individual particle undergoes a dipolar resonance and scatters light in the direction of the particle chain. (Bottom right panel, purple box) The scattered light can reinforce the dipolar resonance of the neighbouring particles when the wavelength of the light is equal to $P$.

As given by Markel [103, 104], the dipole amplitude of particle $m$, $d_m$, taking into account the incident light and the radiated fields of the other dipoles in the chain is given by

$$d_m = \alpha \left[ E_0 + \sum_{m' \neq m} W_{m-m'}(kP) d_{m'} \right], \tag{2.11}$$

where $k = 2\pi/\lambda$ is the incident wavevector, $m$ and $m'$ are the dipole indices, $\alpha$ is the polarizability of the dipole, $E_0$ is the incident field amplitude and

$$W_p(x) = k^3 \left( x^{-1}/|p| + ix^{-2}/|p|^2 - x^{-3}/|p|^3 \right) \exp(ix|p|)$$

is the dipole interaction term in which $p = m - m'$ and $x = kP$.

Solving Eq. (2.11) gives an *effective* dipole amplitude for such a particle in the chain [104]

$$d_m = \frac{a^3 E_0}{a^3/\alpha - (ka)^3 S(kP)}, \tag{2.12}$$

where $S(x) = 2\sum_{m>0}(1/(xm) + i/(xm)^2 - 1/(xm)^3)\exp(imx)$ encapsulates the dipole interactions from the chain elements.

When the wavelength of the incident light is close to the lattice constant of the chain, there is a divergence in $d_m$ [105] (for a detailed theoretical analysis, see [104, 105]). As a result, there is a narrow dip in the transmission of an incident plane wave caused by the coupling of the diffractive modes to the dipole resonances of the individual particles. This resonance is a *collective* mode which is due to the periodicity of the chain and the interaction between the dipoles. This theoretical framework in one dimension can be extended to describe a 2D grating as well [105, 106].

A physical interpretation of lattice resonances in diffractively coupled dipoles is shown by the bottom panels of Fig. 2.1. When light is incident on a small sphere, it is scattered in a dipole-like fashion by the sphere and is the strongest when the wavelength of the incident light corresponds the the dipole resonance of the sphere (see orange box). This scattered light then propagates in the plane of the particle chain. Now if the wavelength of the scattered light also corresponds to the interparticle distance, $P$, the scattered light will arrive at the neighbouring particles in-phase with the dipolar oscillations of the particles themselves thus interfering constructively and reinforcing the dipole resonance of each sphere as shown in the purple box in Fig. 2.1. This is the reason why when the phase-matching conditions are met, there is a sharp dip in the transmission through the particle chain. The wavelengths at which such lattice resonances take place is closely related to the positions of Rayleigh anomalies in a grating [137] and can be estimated by

$$k_0^2 = (k_0 \sin(\theta))^2 + \left(N\frac{2\pi}{P}\right)^2, \tag{2.13}$$

where $\theta$ is the angle of incidence, $k_0$ is the free space wavevector, $k_0 \sin(\theta)$ is the wavevector parallel to the particle chain and $N$ is the diffraction order. This is because Rayleigh anomalies are a result of the passing of diffraction orders from propagating to evanescent modes. At the Rayleigh anomaly point, light is scattered

by the grating in such a way that it propagates in the plane of the grating itself and thus is able to interact strongly with the individual particles. In a way, one can view such lattice resonances as part of the general class of Wood's anomalies [138–140] as well as a surface wave propagating in the plane of the particle chain.

## 2.4 SURFACE PLASMON POLARITONS AT METAL-DIELECTRIC INTERFACES

Before we move on to the theoretical framework of spoof plasmons, conventional Surface Plasmon Polaritons (SPPs), defined as collective electron density waves propagating along and evanescently decaying away from a metal-dielectric interface, will be briefly described here in order to understand the impetus for using metamaterials to engineer tightly confined surface modes. The discussion presented here will be brief as this is not the focus of the thesis. An excellent exposition of SPPs is given by S. A. Maier [141].

We begin by considering a general interface in 2-D between two media with permittivities, $\epsilon_1$ and $\epsilon_2$, as shown in the inset of Fig. 2.2. Assuming a harmonic time dependence (i.e. fields are proportional to $e^{-i\omega t}$), $\mathbf{j}_f = 0$ and $\mu_r = 1$, we have from Eqs. (2.3) and (2.4),

$$\nabla \times \mathbf{E} = i\omega\mu_0\mathbf{H}, \tag{2.14}$$

and

$$\nabla \times \mathbf{H} = -i\omega\epsilon_0\epsilon_r\mathbf{E}, \tag{2.15}$$

which gives us the relation of the E-field components to the H-field components.

If we then confine ourselves to TM modes (i.e. $H_x = H_z = E_y = 0$) for now and we look for solutions to Eqs. (2.14) and (2.15) of the form $H_y \propto e^{i\beta x}e^{-k_z z}$, where $\beta$ is the propagation constant of the wave in the x-direction and $k_z$ is the wavevector in

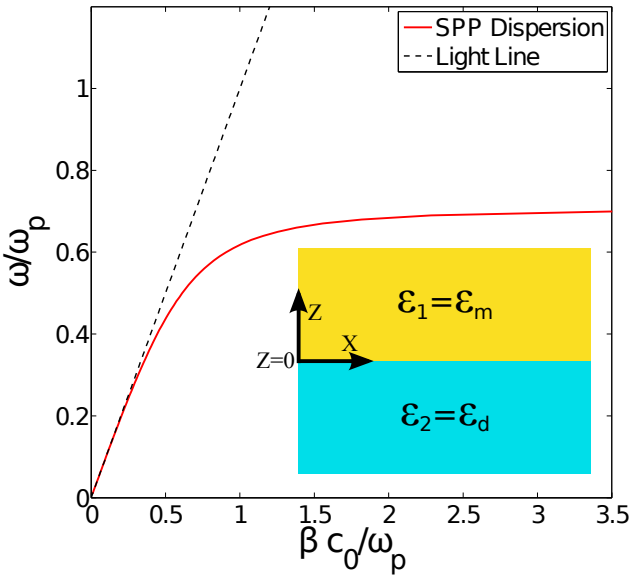



Figure 2.2: Dispersion relation of SPP at a metal-dielectric interface assuming a lossless Drude model for the permittivity of the metal $\epsilon_m(\omega)$, with a plasma frequency $\omega_p$. (Inset) Schematic of metal-dielectric interface.

the z-direction, we would arrive at the following set of equations,

$$\begin{aligned} H_y(z) &= A_1 e^{i\beta x} e^{-k_{z1} z}, \\ E_x(z) &= \frac{i A_1 k_{z1}}{\omega \epsilon_0 \epsilon_1} e^{i\beta x} e^{-k_{z1} z}, \\ E_z(z) &= -\frac{A_1 \beta}{\omega \epsilon_0 \epsilon_1} e^{i\beta x} e^{-k_{z1} z}, \end{aligned} \tag{2.16}$$

for $z > 0$ and

$$\begin{aligned} H_y(z) &= A_2 e^{i\beta x} e^{k_{z2} z}, \\ E_x(z) &= -\frac{i A_2 k_{z2}}{\omega \epsilon_0 \epsilon_2} e^{i\beta x} e^{k_{z2} z}, \\ E_z(z) &= -\frac{A_2 \beta}{\omega \epsilon_0 \epsilon_2} e^{i\beta x} e^{k_{z2} z}, \end{aligned} \tag{2.17}$$

for $z < 0$. Note that $A_1$ and $A_2$ are the amplitude of the H-fields and $k_{z1}$ and $k_{z2}$ are defined such that the solutions decay evanescently away from $z = 0$. We have also assumed that the fields are constant in the y-direction in the 2-D case (i.e. $\partial/\partial y = 0$).

Applying the boundary conditions given by Eqs. (2.7) and (2.8) at $z = 0$ to Eqs. (2.16) and (2.17), we arrive at the following relation,

$$\frac{k_{z1}}{k_{z2}} = -\frac{\epsilon_1}{\epsilon_2}. \tag{2.18}$$

Given that the values of $k_{z1}$ and $k_{z2}$ are both positive, since the signage is taken care of explicitly in Eqs. (2.16) and (2.17), this condition means that $\epsilon_1$ and $\epsilon_2$ have opposite signs. If we describe the permittivity of a metal, $\epsilon_m$ using the lossless Drude model as given by,

$$\epsilon_m(\omega) = 1 - \frac{\omega_p^2}{\omega^2}, \tag{2.19}$$

where $\omega = 2\pi/f$ is the angular frequency and $f$ is the frequency of the incident light, we would see that Eq. (2.18) is well satisfied by metals below the plasma frequency, $\omega_p$. Hence we see at the first instance that one of the conditions for SPP is such that the interface between the two media is made up of a metal below its plasma frequency ($\epsilon_m < 0$) and a dielectric ($\epsilon_d > 0$).

Returning to the Helmholtz equation given in Eq. (2.10) and putting in the conditions of a TM wave in 2-D, we get

$$\frac{\partial^2}{\partial z^2} H_y + (\epsilon_r k_0^2 - \beta^2) H_y = 0, \tag{2.20}$$

which applies in both $z < 0$ and $z > 0$ half spaces and $\epsilon_r$ is the relative permittivity of the media in which the Helmholtz equation is applied.

If we now let $\epsilon_1 = \epsilon_m(\omega)$ and $\epsilon_2 = \epsilon_d$ and solve Eq. (2.20) for $k_z$, we arrive at the following relations,

$$k_{z1}^2 = \beta^2 - \epsilon_m(\omega) k_0^2, \tag{2.21}$$

$$k_{z2}^2 = \beta^2 - \epsilon_d k_0^2. \tag{2.22}$$

Equations (2.21) and (2.22) are basically expressions of conservation of momentum and show that in order for the surface wave to be evanescent normal to the interface,

$\beta^2 > \epsilon_r k_0^2$. Using Eqs. (2.18), (2.21) and (2.22), we can solve for $\beta$ to arrive at

$$\beta = k_0 \sqrt{\frac{\epsilon_m(\omega)\epsilon_d}{\epsilon_m(\omega) + \epsilon_d}}, \tag{2.23}$$

which gives the dispersion relation of the SPP propagating along the metal-dielectric interface.

The red solid line in Fig. 2.2 plots the SPP dispersion assuming a lossless Drude model for $\epsilon_m(\omega)$ (see Eq. (2.19)). The axes are normalised to the plasma frequency of the metal, $\omega_p$. The deviation of the SPP dispersion from the light line at $\omega/\omega_p \approx 0.6$ corresponds to the confinement of light to the interface as can be seen from Eqs. (2.21) and (2.22). Most importantly, note that at frequencies that are small compared to the plasma frequency, the SPP dispersion is very close to the light line, indicating that the SPP fields are very poorly confined. These unconfined SPPs are also known as Sommerfeld-Zenneck waves [122] and are common at low frequencies such as the THz on flat metal surfaces, namely gold, whose plasma frequency is of the order of $10^{15}$ Hz. Hence one can see that at THz frequencies, in order to attain high field confinements for increased light-matter interactions which are important for THz sensing (see Chapter 1), one cannot simply use metals that only support the tightly confined SPPs at visible frequencies. A way to circumvent this issue would be to lower the *effective* plasma frequency by corrugating the metal surface as shall be seen in the next section.

The above mathematical procedure can be used to show that TE waves are not supported. And of course, much can be said of introducing loss in the description of the permittivity of metals to more accurately model the SPP dispersion. But that is not within the scope of this thesis. What is important is to understand that unstructured metal surfaces that are used widely in plasmonics research are inadequate for THz sensing purposes due to their high plasma frequencies. The reader is referred to Ref. [141] for a more in depth discussion of the plasmonic properties of metals in the visible regime.

## 2.5 COUPLED MODE THEORY OF SPOOF PLASMON SURFACES

In this section, a brief overview of the Coupled Mode Method (CMM) will be given with the aim of showing how strongly confined electromagnetic surface modes can be manifested on corrugated metallic surfaces. The basic idea behind CMM is that by expanding the fields within a multilayer system, such as the one seen in Fig. 2.3, by a suitable set of basis functions and applying appropriate boundary conditions at different interfaces in the system, the relationship between the fields in different parts of the system can be obtained. From there, CMM has been widely used to calculate transmission and reflection spectra of metamaterials such as hole or groove arrays with much success [111,119,120,125,142,143]. Here, we shall only discuss the application of CMM with regards to bound surface modes on groove arrays. Only the essential mathematics to give the reader a feel for CMM will be covered. For a full discussion of CMM and its applications to metamaterials see [119,144–146].

### 2.5.1 BASIC PROBLEM SETUP

Consider a generic system like a perfect electric conductor (PEC) film of thickness, $h$, periodically perforated with rectangular holes of widths, $a_x$ and $a_y$, as shown in Fig. 2.3(a). The periodicities are $P_x$ and $P_y$ in the x- and y-directions, respectively. The system can be divided into three regions: I ($z < 0$), II ($0 < z < h$) and III ($z > h$) (see Fig. 2.3(b)).

In regions I and III, the EM fields can be expressed as an expansion of Bloch waves of the form $\sim e^{i\mathbf{k}_{mn}\mathbf{r}}$ with

$$\mathbf{k}_{mn} = \mathbf{k}_i + m\frac{2\pi}{d_x}\mathbf{x} + n\frac{2\pi}{d_y}\mathbf{y}, \tag{2.24}$$

where $\mathbf{k}_{mn}$ is the transverse wave vector (i.e. in the x-y plane) and $\mathbf{k}_i$ is the transverse incident wave vector. Note that $\boldsymbol{r}$ is the transverse position vector.

By definition, the Bloch waves are orthogonal to each other. Mathematically, this

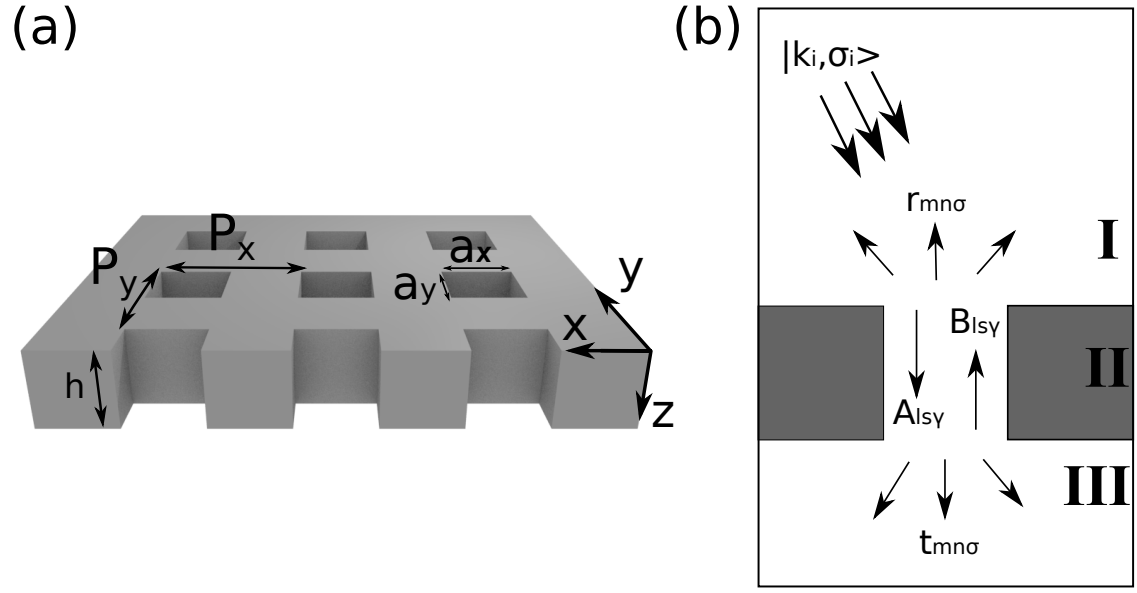



Figure 2.3: Sketch of Coupled Mode Method (CMM) system. (a) The system used here is a perfect electric conductor (PEC) film of thickness, $h$, periodically perforated with rectangular holes of widths, $a_x$ and $a_y$. The periodicities are $P_x$ and $P_y$ in the x- and y-directions, respectively. (b) Cross section of the unit cell.

means that,

$$\langle \mathbf{k}_{mn}, \sigma \mid \mathbf{k}_{m'n'}, \sigma' \rangle = \delta_{mm'}\delta_{nn\prime}\delta_{\sigma\sigma'}, \tag{2.25}$$

where $\sigma$ is the index denoting the two polarizations (s- and p-polarizations).

In region II, the EM fields can be expressed as an expansion of waveguide modes present in the holes. This is valid since we have assumed that the film is a PEC in regions other than the holes. The waveguide modes are denoted by $\mid \mathbf{q}_\alpha, \gamma \rangle$, where $\gamma$ denotes the polarization of the mode (TE or TM). The exact form of the waveguide modes will depend on the shape of the holes. Similar to the propagating light in Regions I and III, the waveguide modes are orthogonal to each other as in Eq. (2.26).

$$\langle \mathbf{q}_\alpha, \gamma \mid \mathbf{q}_{\alpha'}, \gamma' \rangle = \delta_{\alpha\alpha'}\delta_{\gamma\gamma'}, \tag{2.26}$$

where $\alpha$ denote the waveguide mode index.

We are now in a position to give a general description of the fields in the system as a superposition of the eigenfields having clarified their relationship with each

other above. In Region I, the transverse fields (in the x- and y-planes, denoted by subscript $t$) can be expressed as the sum of the incident light with the reflected light in the various diffraction orders as in Eqs. (2.27) and (2.28).

$$|\mathbf{E}_t^I\rangle = |\mathbf{k}_0, \sigma_0\rangle e^{ik_{z0}z} + \sum_{mn\sigma} r_{mn\sigma}|\mathbf{k}_{mn}, \sigma\rangle e^{-ik_{zmn}z}, \tag{2.27}$$

$$-\mathbf{u}_z \times |\mathbf{H}_t^I\rangle = Y^I_{\mathbf{k}_0\sigma_0}|\mathbf{k}_0, \sigma_0\rangle - \sum_{mn\sigma} Y^I_{\mathbf{k}_{mn}\sigma} r_{mn\sigma}|\mathbf{k}_{mn}, \sigma\rangle e^{-ik_{zmn}z}, \tag{2.28}$$

where $\mathbf{u}_z$ is the unit vector in the z-direction, $\mathbf{k}_0$ is the incident transverse wavevector, $\mathbf{k}_{mn}$ is the transverse wavevector of order $(m, n)$, as defined in Eq. (2.24), $k_{zmn} = \sqrt{\epsilon_I k_0^2 - |k_{mn}|^2}$, $r_{mn\sigma}$ is the reflection coefficient for the corresponding diffractive order and $Y_{\mathbf{k}_{mn}\sigma}$ is the mode admittances which are equal to $Y_0 k_{zmn}/k_0$ for TE modes and $Y_0 \epsilon_I k_0/k_{zmn}$ for TM modes. Note that $\epsilon_I$ is the permittivity of Region I and $Y_0 = \sqrt{\epsilon_0/\mu_0}$ is the admittance of free space.

In Region II, the fields outside the holes are zero since the structure is a perfect electrical conductor; within the holes fields can be expressed as a superposition of waveguide modes, $|\mathbf{q}_\alpha, \gamma\rangle$.

$$|\mathbf{E}_t^{II}\rangle = \sum_\alpha [A_\alpha e^{iq_{\alpha z}z} + B_\alpha e^{-iq_{\alpha z}z}]|\mathbf{q}_\alpha, \gamma\rangle, \tag{2.29}$$

$$-\mathbf{u}_z \times |\mathbf{H}_t^{II}\rangle = \sum_\alpha Y_\alpha^{II} [A_\alpha e^{iq_{\alpha z}z} - B_\alpha e^{-iq_{\alpha z}z}]|\mathbf{q}_\alpha, \gamma\rangle, \tag{2.30}$$

where $q_{\alpha z} = \sqrt{\epsilon_{II} k_0^2 - |\mathbf{q}_\alpha|^2}$ and $Y_\alpha^{II}$ is $Y_0 q_{\alpha z}/k_0$ for TE modes and $Y_0 \epsilon_{II} k_0/q_{\alpha z}$ for TM modes. $\epsilon_{II}$ is the permittivity of the waveguide in Region II.

The fields in Region III can be defined in a similar fashion as Region I. Here we use primed quantities to differentiate them from their counterparts in Eqs. (2.27) and (2.28).

$$|\mathbf{E}_t^{III}\rangle = \sum_{mn\sigma} t_{mn\sigma} e^{ik'_{zmn}(z-h)}|\mathbf{k}_{mn}, \sigma\rangle, \tag{2.31}$$

$$-\mathbf{u}_z \times |\mathbf{H}_t^{III}\rangle = \sum_{mn\sigma} Y^{III}_{\mathbf{k}_{mn}\sigma} t_{mn\sigma} e^{ik'_{zmn}(z-h)}|\mathbf{k}_{mn}, \sigma\rangle, \tag{2.32}$$

where $t_{mn\sigma}$ is the transmission coefficient for the various diffraction orders, $k'_{zmn} = \sqrt{\epsilon_{III}k_0^2 - |\mathbf{k}_{mn}|^2}$ and $Y^{III}_{\mathbf{k}_{mn}\sigma}$ is similarly defined as in Region I. $\epsilon_{III}$ is the permittivity of Region III.

We now proceed with the usual process of enforcing the continuity of the transverse fields across boundaries to link the fields in the three regions together. At $z = 0$,

$$|\mathbf{k}_0, \sigma_0\rangle + \sum_{mn\sigma} r_{mn\sigma}|\mathbf{k}_{mn}, \sigma\rangle = \sum_{\alpha}[A_\alpha + B_\alpha]|\mathbf{q}_\alpha, \gamma\rangle, \tag{2.33}$$

and

$$Y^I_{\mathbf{k}_0\sigma_0}|\mathbf{k}_0, \sigma_0\rangle - \sum_{mn\sigma} Y^I_{mn\sigma} r_{mn\sigma}|\mathbf{k}_{mn}, \sigma\rangle = \sum_{\alpha} Y^{II}_{\alpha}[A_\alpha - B_\alpha]|\mathbf{q}_\alpha, \gamma\rangle. \tag{2.34}$$

At $z = h$,

$$\sum_{\alpha}[A_\alpha e^{iq_\alpha h} + B_\alpha e^{-iq_\alpha h}]|\mathbf{q}_\alpha, \gamma\rangle = \sum_{mn\sigma} t_{mn\sigma}|\mathbf{k}_{mn}, \sigma\rangle, \tag{2.35}$$

and

$$\sum_{\alpha} Y^{II}_{\alpha}[A_\alpha e^{iq_\alpha h} - B_\alpha e^{-iq_\alpha h}]|\mathbf{q}_\alpha, \gamma\rangle = \sum_{mn\sigma} Y^{III}_{\mathbf{k}_{mn}\sigma} t_{mn\sigma}|\mathbf{k}_{mn}, \sigma\rangle. \tag{2.36}$$

Equations (2.33) and (2.35) giving the continuity equations for the transverse electric fields are valid over the whole unit cell. For Eqs. (2.34) and (2.36), the magnetic field continuity relations are only valid over the non-PEC regions. This is because of discontinuities in surface current at the PEC interfaces according to Faraday's law. We now proceed to project the continuity equations related to the transverse electric fields over Bloch waves, $|\mathbf{k}_{mn}, \sigma\rangle$, as given in Eq. (2.24) over the entire unit cell. The corresponding equations for the transverse magnetic fields are projected over the waveguide modes within the corrugations of the PEC surface, $|\mathbf{q}_\alpha, \gamma\rangle$. This procedure of projection of the equations over the basis functions can be thought of as a *dot product* in function space[1] and greatly simplifies the equations by eliminating the non-interacting modes.

[1] $\int \langle\phi|\psi\rangle d\mathbf{r}$

Projecting Eq. (2.33) onto plane waves (using the orthogonality relations),

$$\delta_{m0}\delta_{n0}\delta_{\sigma\sigma_0} + r_{mn\sigma} = \sum_{\alpha} Y_{\alpha}^{II}[A_{\alpha} + B_{\alpha}]\langle \mathbf{k}_{mn}, \sigma | \mathbf{q}_{\alpha}, \gamma \rangle. \tag{2.37}$$

Projecting Eq. (2.34) onto waveguide modes (using the orthogonality relations),

$$Y_{\mathbf{k}_0\sigma_0}^{I}\langle \mathbf{q}_{\alpha}, \gamma | \mathbf{k}_0, \sigma_0 \rangle - \sum_{mn\sigma} Y_{\mathbf{k}_{mn}\sigma}^{I} r_{mn\sigma}\langle \mathbf{q}_{\alpha}, \gamma | \mathbf{k}_m n, \sigma \rangle = Y_{\alpha}^{II}[A_{\alpha} - B_{\alpha}]. \tag{2.38}$$

Similar operations on Eqs. (2.35) and (2.36) yields the following,

$$t_{mn\sigma} = \sum_{\alpha}[A_{\alpha}e^{iq_{\alpha}h} + B_{\alpha}e^{-iq_{\alpha}h}]\langle \mathbf{k}_{mn}, \sigma | \mathbf{q}_{\alpha}, \gamma \rangle, \tag{2.39}$$

$$Y_{\alpha}^{II}[A_{\alpha}e^{iq_{\alpha}h} - B_{\alpha}e^{-iq_{\alpha}h}] = \sum_{mn\sigma} Y_{\mathbf{k}_{mn}\sigma}^{III} t_{mn\sigma}\langle \mathbf{q}_{\alpha}, \gamma | \mathbf{k}_{mn}, \sigma \rangle. \tag{2.40}$$

Note here that expressions such as $\langle \mathbf{k}_{mn}, \sigma | \alpha \rangle$ are actually the overlap integrals which are defined as

$$\langle \mathbf{k}_{mn}, \sigma | \mathbf{q}_{\alpha}, \gamma \rangle = \int d\mathbf{r}\langle \mathbf{k}_{mn}, \sigma | \mathbf{r} \rangle \langle \mathbf{r} | \mathbf{q}_{\alpha}, \gamma \rangle = \kappa, \tag{2.41}$$

gives how well one mode couples to another. In the particular case illustrated in Eq. (2.41), the overlap integral gives a measure of how well light in the waveguide mode $|\mathbf{q}_{\alpha}, \gamma\rangle$, couples into the Bloch wave $|\mathbf{k}_{mn}, \sigma\rangle$.

Further algebraic manipulation of Eqs. (2.37) to (2.40) will result in two tight-binding equations that would link the fields in all three regions of the system to each other,

$$\left(G_{\alpha\alpha'}^{I} - \epsilon_{\alpha}\right) E_{\alpha} + \sum_{\alpha \neq \alpha'} G_{\alpha\alpha'}^{I} E_{\alpha'} - G_{\alpha}^{V} E_{\alpha}' = I_{\alpha}, \tag{2.42}$$

and

$$\left(G_{\alpha\alpha'}^{III} - \epsilon_{\alpha}\right) E_{\alpha}' + \sum_{\alpha \neq \alpha'} G_{\alpha\alpha'}^{III} E_{\alpha'}' - G_{\alpha}^{V} E_{\alpha} = 0. \tag{2.43}$$

The quantities in the above tight-binding equations are defined as follows:

$$\begin{aligned} I_\alpha &= 2iY^I_{\mathbf{k}_0\sigma_0}\langle \mathbf{q}_\alpha, \gamma|\mathbf{k}_0, \sigma_0\rangle, \\ G_{\alpha\alpha'} &= i\sum_{mn\sigma} Y_{mn\sigma}\langle \mathbf{k}_{mn}, \sigma|\mathbf{q}_{\alpha'}, \gamma\rangle\langle \mathbf{q}_\alpha, \gamma|\mathbf{k}_{mn}, \sigma\rangle, \\ G^V_\alpha &= \frac{Y^{II}_\alpha}{\sin(q_{\alpha z}h)}, \\ \epsilon_\alpha &= Y^{II}_\alpha \cot(q_{\alpha z}h), \\ E_\alpha &= A_\alpha + B_\alpha, \\ E'_\alpha &= -[A_\alpha e^{iq_{\alpha z}h} + B_\alpha e^{-iq_{\alpha z}h}]. \end{aligned} \tag{2.44}$$

$I_\alpha$ is related to the incident illumination in Region I. $E_\alpha$ and $E'_\alpha$ are the field amplitudes of the waveguide modes at the input (I–II) and output (II–III) interfaces, respectively. $\epsilon_\alpha$ gives the effect of the EM fields at the interfaces, namely I–II and II–III, on itself via the corrugations. $G^V_\alpha$ gives the effect of the fields at one interface on the other which is why $G^V_\alpha$ is the coefficient of $E'_\alpha$ in Eq. (2.42) and of $E_\alpha$ in Eq. (2.43). $G_{\alpha\alpha'}$ describes how light is coupled from waveguide mode $|\mathbf{q}_\alpha, \gamma\rangle$ to diffractive order $\langle \mathbf{k}_{mn}, \sigma|$ and into waveguide mode $|\mathbf{q}_{\alpha'}, \gamma\rangle$, essentially describing the interaction between the corrugations. From this one can see that all the interactions have been incorporated into the coupled equations Eqs. (2.42) and (2.43).

### 2.5.2 BOUND MODES ON LINEAR ARRAY OF SUBWAVELENGTH GROOVES

Having setup the problem in the previous section, it is easy to see how the calculations can become very involved as a large enough number of Bloch waves and waveguide modes, as well as their coupling to one another, needs to be considered. However, precious insights can be gained by simply considering the lowest order and the most dominant modes in the system. Hence, we now shift our focus onto bound surface modes given by the tight-binding equations on a linear array of subwavelength grooves. We consider here a 2D system with a unit cell consisting of a groove

in PEC shown in Figure 2.4 with a period of $P$, a groove width of $a$ and a groove depth of $h$ as well as the following simplifications to the system:

- we take only the fundamental TM waveguide mode, $\alpha = 0$ into consideration. This is valid if $a$ is subwavelength resulting in the fundamental waveguide mode being the only propagating mode.
- we consider only the zero diffraction order p-polarized waves. This is analogous to the metal-dielectric case in the visible light regime where only p-polarized waves give rise to surface plasmons polaritons. And also, the consideration of solely the zero diffraction order is akin to treating the groove array as a metamaterial with an overall aggregate optical response and the incident light being *insensitive* to the periodicity of the system. Note that this assumption begins to break down near the Brillouin zone edge (i.e. $P/\lambda \sim 0.5$) as the corrugations are no longer deeply subwavlength (see Fig. 4.1). In this case, higher diffraction orders need to be taken into account in order to accurately model the metamaterial.

The 2D PEC groove and the above simplifications have quite a few implications on the coupled equations, Eqs. (2.42) and (2.43). First of all, Region III as in Fig. 2.3(b) is now a PEC region. This means that we are only left with Eq. (2.42) since the fields in Region III are zero and $E'_\alpha = 0$ since the interface II–III is now a dielectric–PEC interface in the grooves. The coupling between the interfaces is now irrelevant, hence $G^V_\alpha = 0$. Lastly, the term $\sum_{\alpha \neq \alpha'} G^I_{\alpha\alpha'} E_{\alpha'}$ is zero as we only consider the fundamental waveguide mode. This leaves us with a single equation describing the whole system, $\left(G^I_{\alpha\alpha} - \epsilon_\alpha\right) E_\alpha = I_\alpha$.

To look for the bound modes existing in the system, we further allow $I_\alpha \to 0$. This is because the bound modes should result in a non-zero field amplitude at the interfaces despite an arbitrarily small illumination. Consequently for a non-trivial

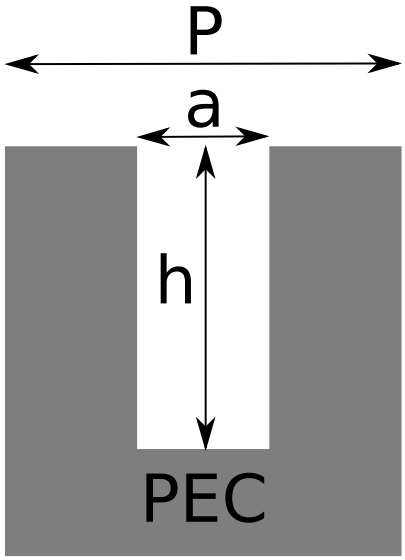



Figure 2.4: Unit cell of an array of subwavelength grooves with period, $P$, groove width, $a$ and depth, $h$.

solution to the tight-binding equation, we must have that the dispersion relation of the bound modes is given by

$$G_{00}^{I} - \epsilon_0 = 0, \tag{2.45}$$

which leads us to

$$\frac{G}{\epsilon} = 1, \tag{2.46}$$

where we have discarded the subscripts and superscripts since they are now superfluous.

Using the definitions given in Eq. (2.44), we have

$$1 = \frac{-Y_{\mathbf{k},p}^{2}|\kappa|^4}{\epsilon^2}, \tag{2.47}$$

where $\kappa$ is the overlap integral given by Eq. (2.41).

For the fundamental TM waveguide mode which has the simple form $\sqrt{1/aP}$, $\kappa$ is given by

$$\kappa = \sqrt{\frac{1}{aP}}\frac{2\sin\left(\frac{a}{2}k_0\right)}{k_0} \sim \sqrt{\frac{a}{P}}, \tag{2.48}$$

in the limit of $ak_0/2$ is small.

Using Eqs. (2.47) and (2.48) and solving for $k_{//} = \sqrt{\epsilon_I k_0^2 - k_z^2}$, gives a dispersion relation for bound modes existing on a linear array of subwavelength grooves as,

$$k_{//} = \sqrt{\epsilon_I} k_0 \sqrt{1 + \frac{\epsilon_I}{\epsilon_{II}} \left(\frac{a}{P}\right)^2 \tan^2\left(\sqrt{\epsilon_{II}} k_0 h\right)}. \tag{2.49}$$

As can be seen, the dispersion relation is quadratic in frequency like that of surface plasmon polaritons in the visible regime at a metal-dielectric interface (note the $k_0$ factor on the RHS of Eq. (2.49)). Hence, such bound modes are termed *spoof plasmons* [116]. The confinement length $L_z$ of the spoof plasmons normal to the metamaterial surface is given by,

$$L_z = \left(k_{//}^2 - k_0^2\right)^{-1/2}, \tag{2.50}$$

and is essentially the deviation of the dispersion relation from the light line. Hence, the spoof plasmon dispersion ($\epsilon_I = \epsilon_{II} = 1$, $P = h$ and $a = P/3$) shown in Fig. 2.5 which deviates significantly from the light line signifies that the mode is evanescent perpendicular to the corrugated PEC surface and is tightly confined in this region.

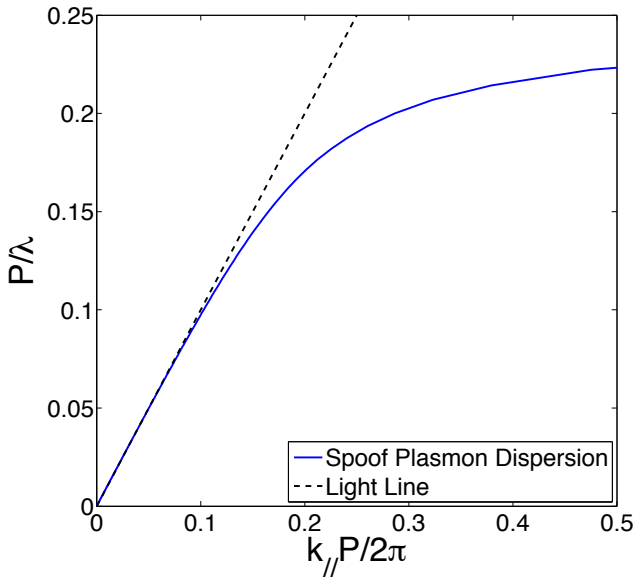



Figure 2.5: Analytical spoof plasmon dispersion given by Equation 2.49.

## 2.6 FOURIER ANALYSIS OF TIME-DOMAIN SIGNALS

Fourier transforms which relate real quantities such as time $t$, to their counterparts in the reciprocal space, frequency $f$, are frequently used in this thesis to process time-domain signals to give frequency space spectra. We begin with the basic Fourier series before moving on to Fourier transforms in its continuous and discrete variable forms. Lastly, short-time Fourier transforms for the time-frequency analysis of dispersive time-domain data is presented. The purpose of this section is to give the reader some background on the key method used in processing the raw data obtained from experiments in this thesis. For the full mathematical properties of Fourier series and transforms, the reader is referred to Ref. [147].

### 2.6.1 FOURIER SERIES

The Fourier series asserts that any periodic function $s(t)$, with period $P$, can be fully replicated by an infinite sum of periodic sinusoidal functions. It is given by

$$s_N(t) = \frac{A_0}{2} + \sum_{n=1}^{\infty} \left[ a_n \sin\left(\frac{2\pi nt}{P}\right) + b_n \cos\left(\frac{2\pi nt}{P}\right) \right], \tag{2.51}$$

where $P$ is the period of the original function and $a_n$ and $b_n$ are the Fourier coefficients for the sine and cosine components, respectively.

This is most easily visualised in the Fourier series decomposition of a square wave shown in Fig. 2.6 as the blue solid line. The red line gives the resultant Fourier series representation as an increasing number terms are included in $s_N(t)$ from the top panel to the bottom panel. As can be clearly seen, $s_N(t)$ slowly builds up to the original function $s(t)$ as terms with higher frequencies are slowly added in varying *amounts*.

We can simplify Eq. (2.51) by taking advantage of the Euler notation for complex

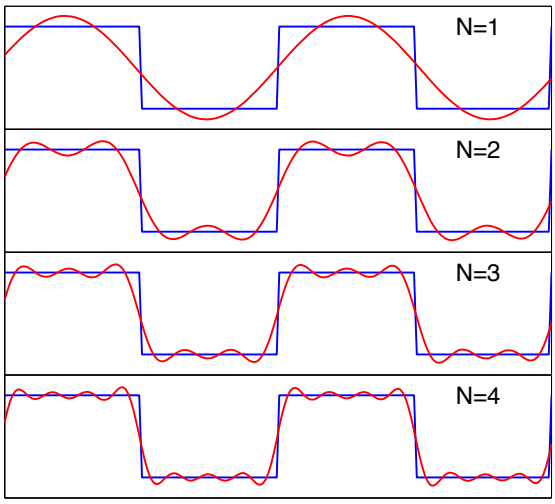



Figure 2.6: Fourier series decomposition of a square wave.

numbers ($e^{ix} = \cos(x) + i\sin(x)$) to give

$$s(t) = \sum_{n=-\infty}^{n=+\infty} \left[c_n e^{i2\pi nt/P}\right], \tag{2.52}$$

where $c_n$ is now a complex Fourier coefficient and the Fourier series is defined based on a set of complex harmonic functions $e^{i2\pi nt/P}$.

To calculate a particular Fourier coefficient $c_m$, we simply multiply $s(t)$ by $e^{-i2\pi mt/P}$ and integrate over the length of the signal to give

$$\begin{aligned}\frac{1}{P}\int_{-P/2}^{P/2} s(t)e^{-i2\pi mt/P}\mathrm{d}t &= \frac{1}{P}\int_{-P/2}^{P/2}\left(\sum_{n=-\infty}^{n=+\infty}\left[c_n e^{i2\pi nt/P}\right]\right)e^{-i2\pi mt/P}\mathrm{d}t \\ &= c_m,\end{aligned} \tag{2.53}$$

where we have made use of the orthogonality relation $\int_{-\pi}^{\pi} e^{imx}e^{inx}\mathrm{d}x = \delta_{mn}$ which removes all terms where $n \neq m$.

The Fourier component $c_n$, represents the magnitude of the sinusoidal wave with a frequency $2\pi n/P$ that is present in the original function $s(t)$. Hence, we can see

here how signals in real space are closely related to the reciprocal space spectra and how using Fourier series we can access information about the reciprocal space, at least for periodic functions in this case.

### 2.6.2 CONTINUOUS FOURIER TRANSFORM

By letting the period of the signal tend to infinity and assuming that outside of a given time interval $s(t) = 0$, we can extend the Fourier series to Fourier transforms which account for non-periodic signals and a continuous frequency variable. In its continuous variable form, the Fourier transform of a given signal from the time-domain *s(t)*, to the frequency-domain $S(\omega)$, and vice versa is given by

$$\begin{aligned} S(\omega) &= \mathcal{F}(s(t)) \\ &= \int_{-\infty}^{\infty} s(t) e^{-i\omega t} \mathrm{d}t, \end{aligned} \tag{2.54}$$

and

$$\begin{aligned} s(t) &= \mathcal{F}^{-1}(S(\omega)) \\ &= \frac{1}{2\pi} \int_{-\infty}^{\infty} S(\omega) e^{i\omega t} \mathrm{d}\omega, \end{aligned} \tag{2.55}$$

respectively, where $\omega = 2\pi f$ and $f$ is the frequency in Hertz. $\mathcal{F}$ and $\mathcal{F}^{-1}$ represent the Fourier transform operator and its inverse, respectively. Note the similarities of Eqs. (2.54) and (2.55) to Eqs. (2.52) and (2.53)

In a way, Fourier transforms can be viewed as a dot product in function space between the signal time function *s(t)* and a set of time-harmonic basis functions $e^{-i\omega t}$. For instance, on a two dimensional Cartesian grid, the dot product of an arbitrary column vector $\boldsymbol{a}$, with the unit axis vector $\boldsymbol{x}$ or $\boldsymbol{y}$, will give the component of $\boldsymbol{a}$ in the x- or y- direction. In other words, the operation $\mathbf{a} \cdot \mathbf{x}$ or $\mathbf{a} \cdot \mathbf{y}$ tells us how *similar* $\boldsymbol{a}$ is to $\boldsymbol{x}$ or $\boldsymbol{y}$. Analogously, Eq. (2.54) asks the question, *"How similar is the signal function $s(t)$, to a set of harmonic functions $e^{-i\omega t}$?"* For example, given a

pulse signal in time, $S(\omega)$ gives the the required *amount* of the frequency component $\omega$, to constitute that pulse.

### 2.6.3 DISCRETE FAST FOURIER TRANSFORM

The data obtained in experiments consists of a finite number of discrete points rather than an infinite and continuously varying signal function as assumed in the previous section. As such, we need to have a discretised form of the Fourier transform in order to process experimental data which is most commonly given by the Fast Fourier Transform (FFT). The FFT of a discrete signal $s[t_n]$ with $N$ points sampled at time intervals of $T$ is given by

$$S\left[\omega_k\right] = \sum_{n=0}^{N-1} s[t_n] e^{-i\omega_k t_n}, \tag{2.56}$$

where $k = 0, 1, ..., N-1$, $\omega_k = 2\pi f_k = \frac{2\pi k}{NT}$ is the k$^{\text{th}}$ frequency point, $t_n = nT$ is the n$^{\text{th}}$ time point and the square brackets indicate the discrete nature of the signal $s$.

The key point to note in Eq. (2.56) is that $S[\omega_k]$ is N-point periodic (i.e. $S[\omega_k, n] = S[\omega_k, n+N]$) and is a pulse train in frequency [148]. This means that the FFT essentially treats the finite length time domain signal also as a N-point periodic pulse train in time. This will have a few implications to the properties of the Fourier transform that become crucial considerations when making measurements. First of all, note that $S[\omega_{N-k}] = S[\omega_k]^*$, where $^*$ implies complex conjugate. This means that the frequency resolution of the FFT $\Delta f$, is given by $\frac{1}{2NT}$ and the highest frequency accessible is given by $f_{max} = \frac{N-1}{2NT}$ [148]. These will determine how long the time-domain signal needs to be and what is the desired $T$ value. Secondly, as the time-domain signal is also treated as a pulse train by the FFT, this means that, to the FFT procedure, the start of $s[t]$ is joined to the end of $s[t]$. Hence it is important that both the start and end of $s[t]$ is zero. Otherwise, to the FFT, it would seem as if there is a discontinuity in the signal, resulting in spurious frequency content. A apodization window that slowly tapers the ends of $s[t]$ to zero is usually applied to

the experimentally collected data to counteract this effect. However, the shape and length of the window needs to be carefully chosen to minimise other spectral effects such as spectral leakage and loss of frequency resolution [149, 150].

### 2.6.4 SHORT-TIME FOURIER TRANSFORM

The Fourier transform gives the frequency content of the entire time signal by integrating over the entire signal duration. However, it could well be possible that the time signal is very dispersed (i.e. different frequency components propagate at different velocities and hence arrives at the detector at different times), such as that shown by the black line in Fig. 2.7. Or there might be secondary reflections in the system as shown by the second peak in the signal at around 370 ps in Fig. 2.7. In such situations, a simple frequency analysis of the signal becomes inadequate and it might be necessary conduct a time-frequency analysis by picking out the frequency content of the signal at specific time points.

One common form of time-frequency analysis is called the short-time Fourier transform (STFT) [148] which is given by,

$$S(\tau, \omega) = \int_{-\infty}^{\infty} s(t) w(t - \tau) e^{-i\omega t} dt, \tag{2.57}$$

where $s(t)$ is the time-domain signal, $w(t)$ is the window function and $S(\tau, \omega)$ is the STFT at time $\tau$. Note that we have reverted to the continuous variable representation for simplicity.

The window function $w(t)$, usually has a Gaussian-like profile that is non-zero within a certain window duration $L_w$. The maximum value of $L_w$ is equal to the duration of $s(t)$, $L_s$. This is because if $L_w = L_s$, the STFT is simply a normal Fourier transform with an apodization window applied (see previous section). In order to properly conduct a time-frequency analysis, $L_w$ has to be shorter than $L_s$ such that anywhere outside of $L_w$, $s(t) = 0$. In this way, as $w(t)$ is slid along $s(t)$, by varying $\tau$, the only non-zero part of the time signal will be in the time range of $\tau \pm L_w/2$ (see

Fig. 2.7). This means that the Fourier transform of $s(t)w(t-\tau)$ will only contain frequency information around the time $\tau$ since the rest of the $s(t)$ is now zero.

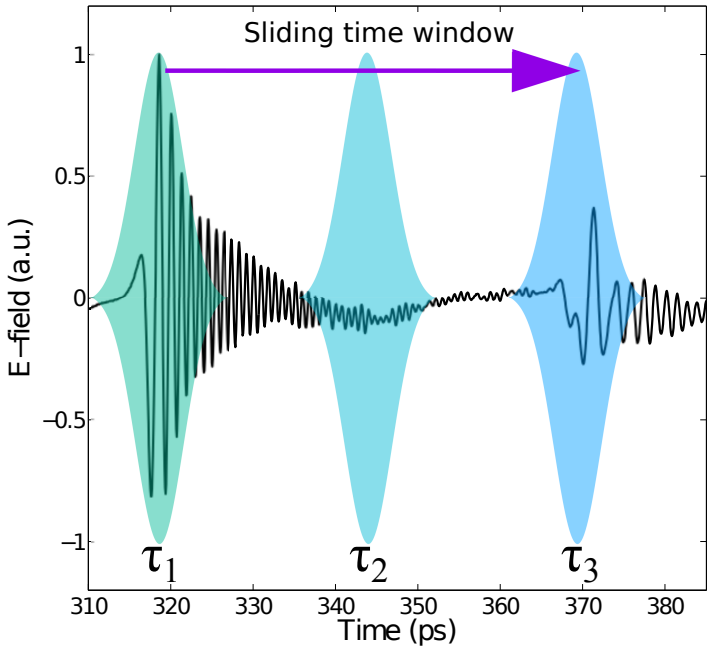



Figure 2.7: Explanation of short-time Fourier transform (STFT). A sliding time window is imposed on the signal to look at the frequency content of the signal at different time points.

Thus a 2D time-frequency plane can be built up by progressively sliding $w(t)$ along the whole of $s(t)$. This allows us to know the frequency components present in $s(t)$ at specific time points $\tau$.

As mentioned in the end of the previous section, the application of a time window will inevitably affect the Fourier transform. In the case of the STFT, the finite length of the time window introduces an uncertainty in the time coordinate of a particular frequency component of $\Delta w$, which is the FWHM of $w(t)$. And that in turn introduces a width in $S(\tau, \omega)$ of $\Delta\omega \sim 1/\Delta w$ (see [148]). We shall see the application of STFT for signal processing in the work presented in Chapter 5.

CHAPTER 3

# REFRACTIVE INDEX SENSING VIA LATTICE RESONANCES

## 3.1 INTRODUCTION

In this chapter, results on utilising lattice resonances, supported on a metallic antenna array, for THz sensing are presented. As mentioned in Chapter 1, such optical coupling effects have been demonstrated in the visible regime [102, 106–108]. Here, we translate this idea to THz frequencies so that we can take advantage of the delocalised nature of the lattice resonances on a 2D array of metallic bars to increase the interaction volume of THz radiation with analytes. In particular, a small fluid chamber containing the antenna array was filled with various fluids and placed in a THz-TDS. Changes in the transmission spectra, in response to the change in the dielectric environment of the antennas, was used to conduct fluid refractive index sensing. Most importantly, the work presented here is the springboard from which we launch into work on spoof plasmon sensing in the later chapters.

## 3.2 EXPERIMENTAL & SIMULATION METHODS

The THz antenna array, designed to work in the wavelength range of 200 $\mu$m $< \lambda_0 <$ 600 $\mu$m, was first simulated in a homogeneous and lossless dielectric environment using the finite-difference-time-domain (FDTD) method (FDTD Solutions 6.5, Lumerical Inc.). In this way, the characteristics of the collective antenna resonance mediated by diffractive coupling between individual antennas can be clearly discerned by avoiding spectrum artefacts due to the substrate and maximising the coupling efficiency between antennas [107, 108]. The simulated antennas were assumed to be perfect electric conductor (PEC) slabs with rounded ends and have

dimensions of $l = 85$ $\mu$m, $w = 38$ $\mu$m and a thickness of 200 nm as depicted in Fig. 3.1(a). The PEC antenna was embedded in a 200 $\mu$m $\times$ 220 $\mu$m unit cell with a refractive index of 1.7 and periodic boundary conditions. The system was excited by a plane wave polarised in the x-direction at normal incidence (see Fig. 3.1(a)).

A 2D array of rectangular metal antennas was fabricated via direct laser writing on positive photoresist followed by a liftoff process on 100 $\mu$m thick polyethylene napthlate (PEN) substrates obtained from Dupont Teijin Films (Teonex Q81). A 2.2 $\mu$m thick layer of Microposit S1822 positive photoresist was first spin-coated onto the PEN substrate at 5000 RPM and baked on a hotplate for 1 minute at 110°C. The sample was then placed on a computer controlled stage and exposed to light with a wavelength of 400 nm from a frequency doubled Ti:Sapphire femtosecond laser (Spectra Physics Tsunami, Model 3960, $\tau = 100$ fs, repetition rate=82 MHz). The light was focussed onto the sample via a 100$\times$ microscope objective. The antenna patterns, which were simply rectangles with rounded ends, were then written on the photoresist by moving the sample relative to the focussed light spot using the stage. After the development of the photoresist using the Microposit MF-319 developer to reveal the inverse antenna array, 5 nm of Cr followed by 200 nm of Au was deposited on the sample via electron beam evaporation. Finally, any unwanted photoresist and metal was removed via acetone ultrasonic agitation, leaving behind the final antenna array as shown in Fig. 3.1(b). The final sample consists of a $30 \times 30$ array of $(85 \pm 1)$ $\mu$m $\times$ $(38 \pm 3)$ $\mu$m Au antennas with periods of $P_x = (200 \pm 1)$ $\mu$m and $P_y = (221 \pm 1)$ $\mu$m in the x- and y-direction, respectively as shown in Fig. 3.1(b). As can be seen, the fabricated antennas closely resemble the simulated ones. The entire sample measures 6.6 mm by 6.6 mm and is sufficiently large such that the 3 mm diameter THz beam from the THz-TDS, used to characterise the sample, is well within the sample area.

Fluid refractive index sensing was performed using a THz-TDS (TPS3000, Tera

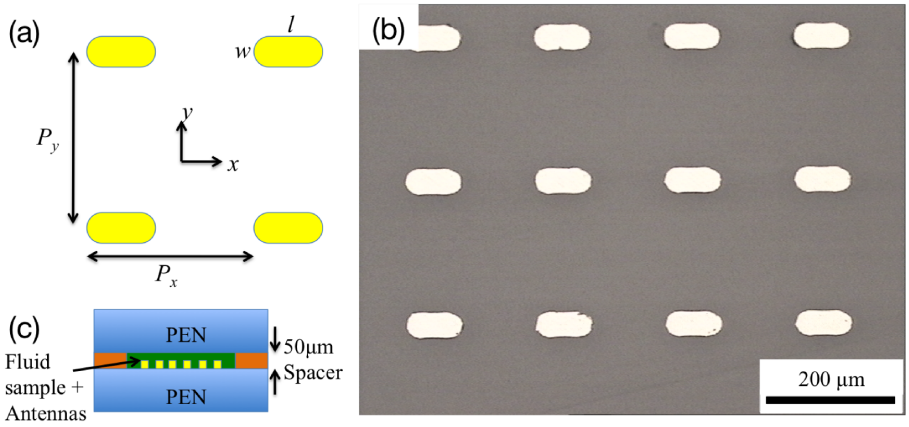



Figure 3.1: (a) Schematic diagram of THz antenna array with antennas of length $l$, width $w$ and periods $P_x$ and $P_y$ in the x and y directions, respectively. (b) Optical microscope image of THz antenna array. (c) Schematic diagram of the fluid chamber assembly used for transmission measurements. Reprinted with permission from [151]. Copyright 2011, OSA.

View Inc.) and a small fluid chamber as shown in Fig. 3.1(c). The fluid chamber consists of a 100 $\mu$m thick PEN substrate which supports the antenna array, a 50 $\mu$m spacer and another 100 $\mu$m thick PEN film as the capping layer. THz radiation was normally incident and polarised in the x-direction. Gaseous nitrogen (control), methanol, ethanol and liquid paraffin were used to fill the chamber and demonstrate refractive index sensing. The transmission spectra for the fluids with the antenna array present was measured and normalised to that without the antennas in order to monitor the changes in the optical response as the dielectric environment of the antennas was varied. All measurements were made in a nitrogen purged chamber to reduce the effects of water absorption (see Appendix A).

To quantitatively analyse the performance of lattice resonance refractive index sensing, a Figure-of-Merit (FOM) defined by Eq. (3.1) [152] was extracted from the experimental results,

$$FOM = \frac{\Delta\lambda_{res}/\Delta n}{\Gamma}, \tag{3.1}$$

where $\Delta\lambda_{res}$ is the change in resonance wavelength, $\Delta n$ is the change in refractive index and $\Gamma$ is the full width at half maximum (FWHM) of the resonance.

The rationale behind the FOM is similar to why one uses a thin and narrow pointer on a weighing scale instead of a thick one. The numerator of the FOM gives how much the readout response of the sensing mechanism changes with respect to a change in environmental condition. However if the readout feature, namely the dip in transmission or the pointer on a scale, is very broad, it is very hard to discern small changes in the conditions of the system. Ideally, one would like a system where there is a large change to a small perturbation in the system while at the same time a very narrow readout feature to facilitate the discernment of the smallest change possible.

## 3.3 CHARACTERISTICS OF LATTICE RESONANCES

The simulation results of an infinite antenna array embedded in a homogeneous environment with a refractive index of 1.7 are presented here. Figure 3.2(a) shows the transmission spectrum of the simulated antenna array (red-solid line). The first features to note are the Rayleigh anomalies denoted by the blue-dashed lines whose positions are given by $(n_{env}k_0)^2 = (2N\pi/P_x)^2 + (2M\pi/P_y)^2$, where $n_{env}$ is the refractive index of the environment and $(N, M)$ represents the diffraction order, similar to that defined in Section 2.3. Note that only the (1,1) and (0,1) order Rayleigh anomalies can be seen here. The (1,0) Rayleigh anomaly is not clearly resolved due to the symmetry of the system [102]. At $\lambda = 281$ $\mu$m (Fig. 3.1(a), red square), there is a broad dip in transmission which is due to the dipolar resonance of the individual antennas. Lastly, near the (0,1) Rayleigh anomaly, at $\lambda = 389$ $\mu$m (Fig. 3.1(a), green circle), there is a sharp dip in transmission as a result of the resonant interactions between the antennas as they become diffractively coupled (see Section 2.3). Note that the position of the lattice resonance is approximately $1.7P_y$, in accordance to the theoretical expectation that the lattice resonance occurs when the wavelength is approximately equal to the periodicity of the grating and near the particle resonance.

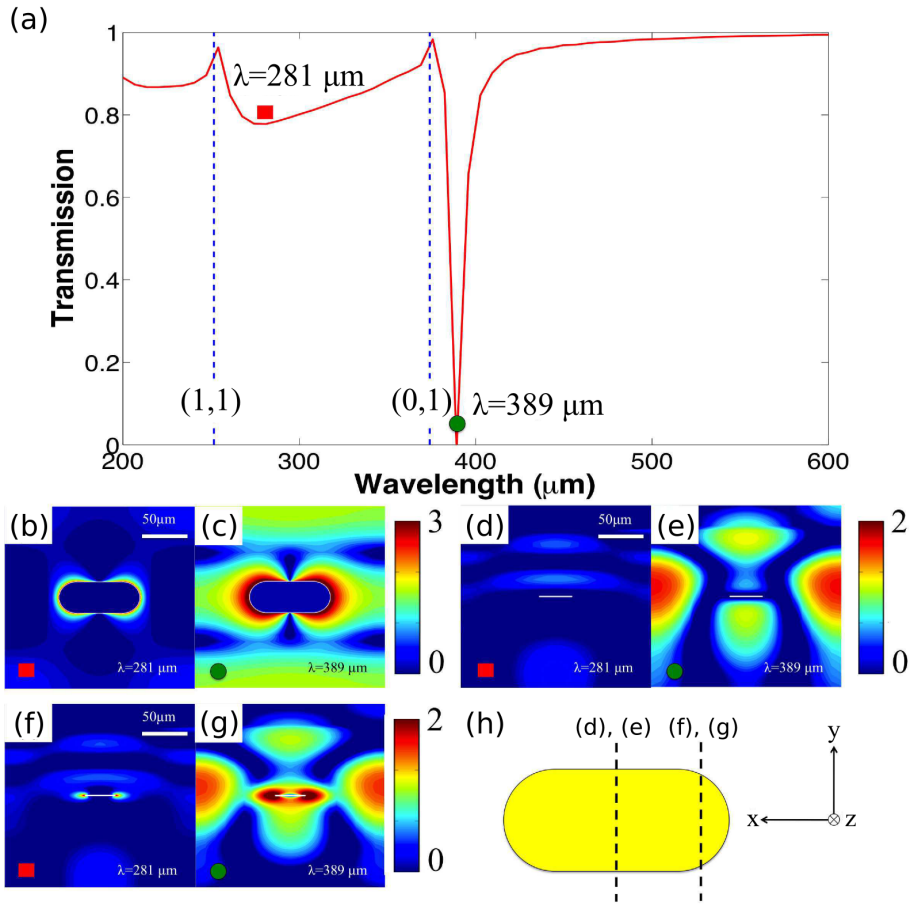



Figure 3.2: (a) Simulated transmission spectrum of the THz antenna array ($l = 85$ $\mu$m, $w = 38$ $\mu$m, $P_x = 200$ $\mu$m and $P_y = 220$ $\mu$m) embedded in an infinite homogeneous medium of $n = 1.7$. (0,1) and (1,1) Rayleigh anomalies (blue dashed lines) occur at $\lambda = 374$ $\mu$m and $\lambda = 251$ $\mu$m, respectively. The geometrical dipole resonance (red square) and the lattice resonance (green circle) can also be clearly seen. (b, c) Log-scale electric field intensity distributions in the z-normal plane at $\lambda = 281$ $\mu$m and $\lambda = 389$ $\mu$m. (d - g) Log-scale electric field intensity distributions in the x-normal plane cutting through the center of the antenna ((d) and (e)) and at 32.5 $\mu$m offset from the center in the x-direction ((f) and (g)) at $\lambda = 281$ $\mu$m and $\lambda = 389$ $\mu$m. The white line marks out the antenna position. (h) Diagram indicating the coordinate system and the cutting planes of (d, e) and (f, g). Reprinted with permission from [151]. Copyright 2011, OSA.

To further understand the nature of the lattice resonance supported by an antenna array, we now look at the field distributions around the antenna at $\lambda = 281$ $\mu$m and $\lambda = 389$ $\mu$m (see Fig. 3.1(b)–(h)). Figure 3.1(b) and (c) show the log-scale electric field intensity distributions in the z-normal planes at $\lambda = 281$ $\mu$m and $\lambda = 389$ $\mu$m,

respectively. As can be seen in Fig. 3.1(b), the geometrical half-wavelength mode of the antenna results in a dipole-like field distribution at $\lambda = 281$ $\mu$m. Meanwhile, at the lattice resonance point (Fig. 3.1(c)), the fields become very delocalised with significant field enhancements in the region between the antennas, indicating that there are strong interactions between neighbouring antennas. At the same time, the region of high field enhancement in the immediate vicinity of the antenna is larger than that shown in Fig. 3.1(b) since at the lattice resonance point there is a divergence in $d_m$ (see Section 2.3).

Figure 3.1(d) and (e) show the log-scale electric field intensity in the x-normal plane cutting through the center of the antenna which is depicted as the white line. Again, at the antenna geometrical half-wavelength resonance point (Fig. 3.1(d)), there is almost no field enhancement between the neighbouring antennas while at the lattice resonance point (Fig. 3.1(e)), there is a significant concentration of electric field. This is in line with the physical interpretation of lattice resonances given in Section 2.3 that light scattered off the individual antennas propagate in the plane of the array and interacts with the neighbouring antennas in a way which reinforces the dipole-like resonance of the individual antennas. A similar picture is painted by Fig. 3.1(f) and (g) which show the x-normal plane electric field distribution at a 32.5 $\mu$m offset from the center in the x-direction. The locations of the x-normal planes are shown in Fig. 3.1(h).

At this point we can begin to see how lattice resonances can be applied to THz sensing. First of all, the position of the lattice resonance is related to the refractive index of the environment and can be tuned by simply changing the geometrical parameters of the array. Moreover, the fact that the entire environment is used to provide the phase-matching conditions required for the lattice resonance means that the whole sample is *probed*. The delocalised nature of the lattice resonance is in sharp contrast with previously proposed THz sensing methods where the optical

response of a metamaterial, such an array of split-ring resonators, is only sensitive to changes in specific electric field hot spots [153]. This means that complicated surface functionalisation processes to localise analytes in specific spots with high field concentration may not be needed when sensing via lattice resonances.

However, there are also some caveats to take note of in a practical sensing situation which is discussed in detail by Auguiè *et al.* in Ref. [154]. As the lattice resonance can be thought of as a surface wave propagating in the plane of the antenna array, a refractive index difference between the substrate and the sensed sample as well as the presence of losses will impede the surface wave's ability to propagate towards and interact with the neighbouring antennas. Hence in the idealised case here with no losses, light scattered by the antennas is capable of propagating indefinitely along the plane of the array and interacts with, theoretically speaking, an infinite number of neighbouring antennas. In experiments, a refractive index difference between substrate and sample will result in a de-phasing of the surface wave while losses cause the attenuation of the scattered light as it propagates. All this means that the lattice resonance will have a finite spatial range of interaction and individual antennas will not interact will all the other antennas in the array. Consequently, the contribution to $d_m$ in Eq. (2.11) from the second term in the square brackets will be diminished, resulting in a weaker lattice resonance. Nonetheless, diffractive coupling between antennas can still be achieved by reducing the refractive index contrast between the substrate and the sensed analyses [107, 154]. Bearing these conditions in mind, we now move on to the experimental results on fluid sensing via lattice resonances.

## 3.4 FLUID REFRACTIVE INDEX SENSING WITH LATTICE RESONANCES

In the fluid sensing experiments, PEN was chosen as the substrate for the following reasons:

1. PEN has a refractive index of approximately 1.6 which is a good match for the fluids being tested.

2. It is relatively low loss.

3. It is cheap and flexible and thus making it potentially viable as a disposable sensor chip.

Figure 3.3 shows the experimental (red-solid lines) and simulated (black-dashed lines) transmission spectra for nitrogen, liquid paraffin, ethanol and methanol. The lattice resonance positions are demarcated by the red arrows. As can be seen, there is a good qualitative agreement between the experimental and simulated results. The simulations were carried out again with the FDTD method, taking into account the fluid chamber in the unit cell. The resultant data was then processed in the same way as the experiments. The fluid dielectric constants used were experimentally obtained according to the parameter extraction method given by Duvillaret et al. [155] via a Matlab code written by Dr. Stephen Hanham.

We first note that the lattice resonance for nitrogen (Fig. 3.3(a)) is much weaker than those of the liquid samples. This is mainly because of the refractive index mismatch between the substrate and nitrogen which results in the weaker diffractive coupling between antennas as mentioned before.

The dips prior to the lattice resonances are attributed to guided modes which exist within the substrate or superstrate due to phase matching from the antenna array itself [154]. This is illustrated in Fig. 3.4, which shows the electric field distribution in the x-normal plane of the fluid chamber at $\lambda = 276$ $\mu$m, 346 $\mu$m and 367 $\mu$m, respectively (from left to right), for the nitrogen case. As can be seen in the panel corresponding to the lattice resonance at $\lambda = 367$ $\mu$m, the field distribution is very similar to that of Fig. 3.2(e). While for the transmission dips at $\lambda = 276$ $\mu$m and 346 $\mu$m (see Fig. 3.3(a)), we can see that the fields are concentrated in the bottom

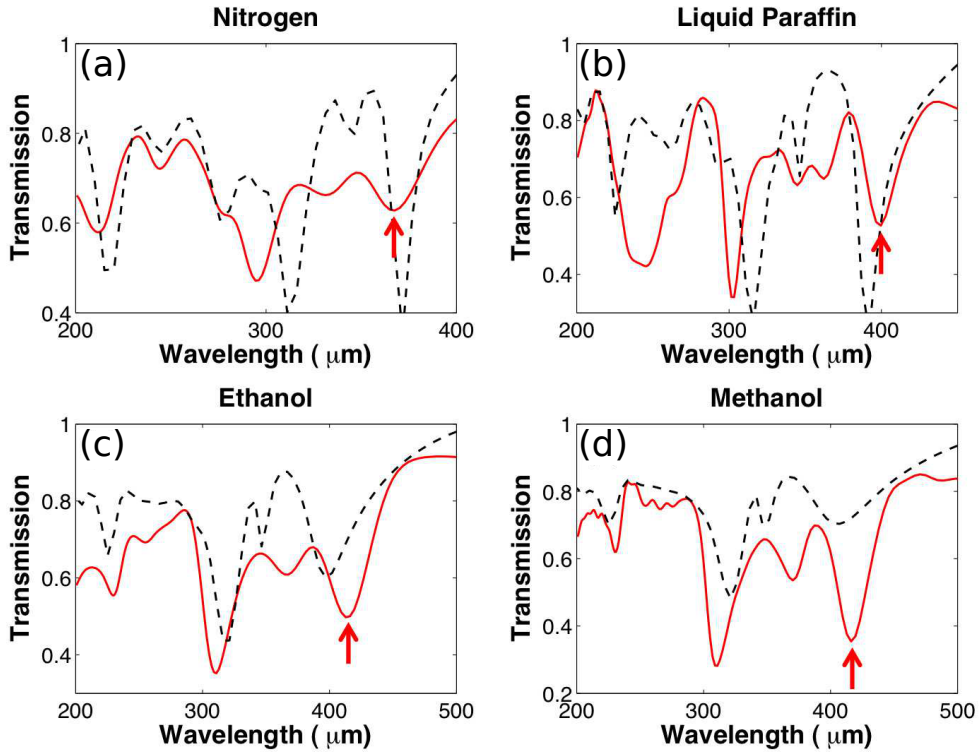



Figure 3.3: (a)–(d) Experimental (red solid lines) and simulated (black dashed lines) transmission spectra for nitrogen, liquid paraffin, ethanol and methanol, respectively. The lattice resonance is marked by the red arrow. Transmission dips at wavelengths smaller than that of the lattice resonance are due to guided modes that exist in the substrate and superstrate. Reprinted with permission from [151]. Copyright 2011, OSA.

and top PEN layer, respectively, and corresponds to guided modes within the PEN layer. Another thing to note is the geometrical half wavelength mode of the antenna is now obscured by the dips in transmission due to the guided modes.

A closer examination of Fig. 3.3 will reveal that the guided mode resonances are sometimes sharper than the lattice resonance (for example, the dip at $\lambda \approx 300$ $\mu$m in Fig. 3.3(b)). Naively speaking, the guided modes could potentially be an even better mechanism to conduct sensing than lattice resonance if we look at the metric of performance set out in Eq. (3.1). However, guided modes depend critically on the sample or substrate thickness and refractive indices, and may exhibit cutoff

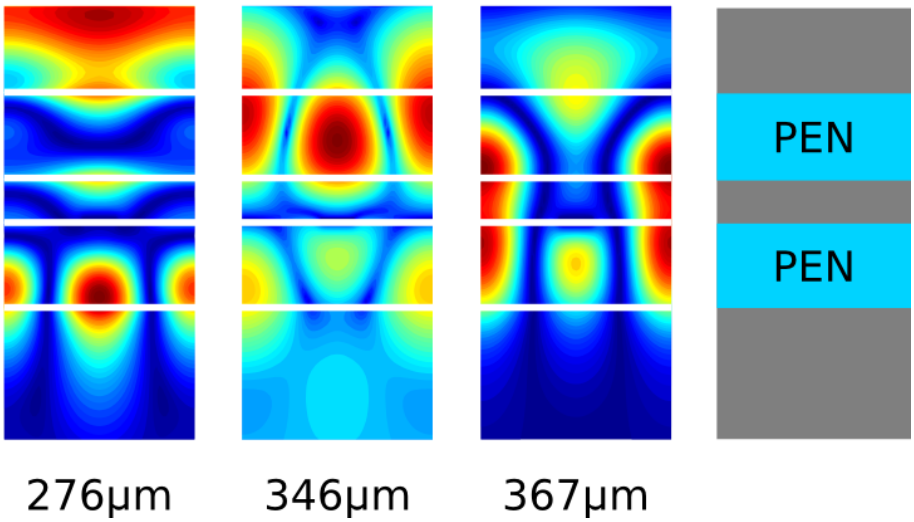



Figure 3.4: Electric field distribution of guided modes ($\lambda$ = 276 $\mu$m and 346 $\mu$m) and lattice resonance ($\lambda$ = 367 $\mu$m) (from left to right). The PEN boundaries are shown by the white lines. The right-most panel shows the schematic of the cross section.

behaviour. Lattice resonances on the other hand depend only on the geometrical parameters of the array and thus is more robust when it comes to sensing applications. One way of circumventing the problem of guided modes obscuring the transmission spectrum would be to use thinner substrates to shift the guided modes out of the desired frequency regime.

Table 3.1 gives the lattice resonance wavelengths $\lambda_{res}$, and the corresponding refractive indices $n_{res}$, of the fluids characterised. As can be seen, the lattice resonance red-shifts as $n_{res}$ increases. This indicates that the lattice resonance is indeed sensitive to environmental changes. Taking a closer look at the properties of the resonance, we note that the Q-factor of the antenna array is around 20. This is almost double that reported for Split-Ring Resonator (SRR) metamaterials (Q-factor $\approx$ 10) [156] and is at least comparable to that of asymmetric SRRs supporting sharp Fano resonances [91]. As such, the potential for lattice resonance to conduct THz sensing is at least on par with the previously proposed metamaterial sensing methodologies.

Table 3.1: Table of lattice resonance wavelength $\lambda_{res}$, and corresponding refractive index $n_{res}$, for nitrogen, liquid paraffin, ethanol and methanol

| **Fluid Sample** | **Resonance Wavelength,** $\lambda_{res}$ | **Refractive Index** $n_{res}$ |
|---|---|---|
| Nitrogen | 367 $\mu$m | 1.00 |
| Liquid Paraffin | 400 $\mu$m | 1.49 |
| Ethanol | 412 $\mu$m | 1.60 |
| Methanol | 416 $\mu$m | 1.71 |

By plotting the shift in resonance $\Delta\lambda_{res}$, against sample refractive index $n_{res}$, as shown in Fig. 3.5, the sensitivity of the lattice resonance to refractive index changes, $\xi = \Delta\lambda_{res}/\Delta n_{res}$ (also the numerator of the FOM) can be extracted. The data is well fitted to the linear equation, $\Delta\lambda_{res} = 70.73n_{res} - 70.82$. From this linear fit equation, it can be seen that $\xi = 70.73$ $\mu$m/RIU, where RIU stands for Refractive Index Unit, and the FOM is 3.80. The $\xi$ and FOM values are valid for fluid samples that are 50 $\mu$m thick. For samples of other thicknesses, the interaction volume between the fields and the fluid will be different and hence would result in different $\xi$ and FOM values. At the point of publication of the above results [151], the closest comparison, to the best of our knowledge, in terms of metamaterials sensing was in the mid-IR regime where the highest FOM obtained from simulation was 2.86 [157].

As the strength of lattice resonances mediated by diffractively coupled antennas is strongly dependent on the range of interaction of the surface wave $L_x$, propagating along the plane of the antenna array, one would expect that the diameter of the incident light beam $d_{beam}$, in experiments to play a role in the actual measured strength of the lattice resonance. In general, the more neighbouring antennas the lattice resonance surface wave interacts with, the stronger the resonance. However, if $L_x \ll d_{beam}$, then any increase in beam diameter will not significantly increase the strength of the lattice resonance as most of the collective interactions would have been captured within the beam. The reverse would be true if $L_x \sim d_{beam}$ and an increase in $d_{beam}$ will be expected to result in a stronger lattice resonance. $L_x$ can

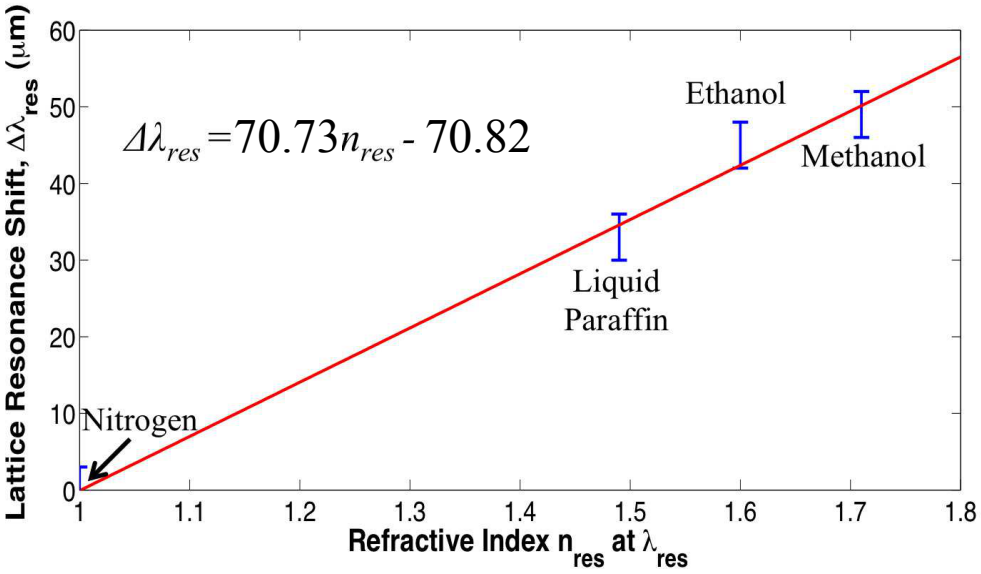



Figure 3.5: Lattice resonance shift, $\Delta\lambda_{res}$ plotted against the refractive index $n_{res}$ at $\lambda_{res}$. The data is well described by the equation $\Delta\lambda_{res} = 70.73n_{res} - 70.82$ (red line) for 50 $\mu$m thick samples. Reprinted with permission from [151]. Copyright 2011, OSA.

be estimated by [107],

$$L_x = \frac{1}{\Delta k_x}, \tag{3.2}$$

where $\Delta k_x$ is the width of the resonance in k-space and is estimated from the FWHM of the lattice resonance. It was found that $L_x \sim 1$ mm for the fluids tested and thus is comparable to $d_{beam}$. Hence it is expected that if a larger beam was used to illuminate the antenna array, more of the diffractive coupling interactions would have been captured and a stronger lattice resonance would have been observed. One can see the effect of capturing more of the inter-antenna interactions by looking at the simulation result (Fig. 3.2(a)) which shows a much stronger lattice resonance due to a plane wave illumination of an infinite array.

## 3.5 EVALUATING LATTICE RESONANCE SENSING: WHAT COMES NEXT?

In this chapter, fluid refractive index sensing via lattice resonances is demonstrated. The ability to tune the positions of the lattice resonances via the geometric param-

eters of the antenna array makes lattice resonances a flexible way to conduct THz sensing over a large range of wavelengths. In addition, the delocalised nature of the lattice resonance means that the entire fluid sample is probed and is not only sensitive to dielectric changes in specific electric field hot spots. Also, we showed that the lattice resonance sensing performance is at least comparable to that of previously proposed metamaterial sensing methods.

However, the lattice resonance sensing method also suffers from a few drawbacks. First of all, the guided modes which obscure the transmission spectra are hard to get rid of. Although using thinner substrates is one way of circumventing the problem, it can make the sensor fragile due to its thinness. Secondly, the weakening of the resonance due to a refractive index contrast between the substrate and sensed fluid is unavoidable in a practical situation and is a handicap when designing sensors for various sensing purposes since one would be limited by the availability of materials.

An ideal sensing mechanism should give the maximum field confinement so as to make the best use of the limited power available in the THz and allow for small sample volumes to be sensed (see Chapter 1). At the same time, the ability to freely engineer the optical response of the sensor without compromising the integrability of the sensor into a lab-on-chip configuration as well as be limited by the choice of materials is important in a real-world setting where sensed analytes might need to undergo other forms of characterisation or are in small quantities. These requirements led to the exploration of the use of spoof plasmons for THz sensing discussed in the following chapters.

CHAPTER 4

# SPOOF PLASMON SURFACES AS A PLATFORM FOR TERAHERTZ SENSING APPLICATIONS

## 4.1 INTRODUCTION

We see from the conclusions of the previous chapter that lattice resonance based sensing suffers from some drawbacks when it comes to practical sensing applications. Here, we turn our attention to spoof plasmons in an attempt to push THz sensing, with all its potential benefits, one step closer to real world applications using metamaterials. As we shall see in the following chapters, metamaterial surfaces supporting tightly confined spoof plasmons, which we simply term Spoof Plasmon Surfaces (SPSs), go some way in addressing some of the difficulties faced.

SPSs have been widely studied for their waveguiding potential as well as the plethora of interesting optical effects that can be manifested on them [123, 125, 128, 133, 158, 159]. However, very little scientific effort has been devoted to the exploitation of these novel structures to overcome problems in THz sensing. In this chapter, we present the results of using a SPS consisting of a linear array of subwavelength grooves to demonstrate refractive index sensing. First, the general characteristics of spoof plasmons supported on our SPS will be discussed to lay out some general guidelines for SPS design. Next, spoof plasmons, coupled into via an Otto prism setup, are shown to be capable of high performance narrowband THz sensing as the grooves of the SPS are filled with various fluids. In particular, the phase jumps that occur at the spoof plasmon coupling frequency are used as the readout response, instead of the conventional amplitude response.

## 4.2 SPOOF PLASMONS ON A LINEAR ARRAY OF SUBWAVELENGTH GROOVES

Let us begin by looking at the general properties of spoof plasmons supported on a linear array of subwavelength PEC grooves. The dispersion relation of spoof plasmons for square PEC grooves, obtained from the coupled mode method under certain simplifications (see Section 2.5 and Eq. (2.49)), is reproduced here for convenience.

$$k_{//} = k_0\sqrt{1 + \frac{1}{\epsilon_{II}}\left(\frac{a}{P}\right)^2 \tan^2\left(\sqrt{\epsilon_{II}}k_0 h\right)}, \tag{4.1}$$

where $k_0$ is the free space wavevector, $k_{//}$ is the wavevector of the spoof plasmon in the direction of propagation, $a$ is the width of the groove, $P$ is the period of the grooves and $\epsilon_{II}$ is the permittivity of the material filling the grooves. The region above the SPS is assumed to be air.

Although Eq. (4.1) is derived from a very idealised scenario, there are precious insights that can be drawn from this simple analytical expression. First of all, it can be seen that $a/P$ gets larger, $k_{//}$ gets larger as well, indicating that the fields become more confined at a given frequency with wider grooves. This is seen in Fig. 4.1(a) where the analytical spoof plasmon dispersion for $a = 30$ $\mu$m and $h = 30$ $\mu$m (blue line) deviates more strongly from the light line than that of $a = 10$ $\mu$m and $h = 30$ $\mu$m (red line). Of course, it will not escape notice that following this path of reasoning, at $a/P = 1$ the spoof plasmon dispersion will be even more confined even though the surface will now be flat with no grooves to speak of at all! However, that is not the case as $h$ will be equal to zero, resulting in $k_{//} = k_0$ which is what is expected for flat PEC surfaces where only Sommerfeld-Zenneck surface waves propagate [122].

The next point to note in Eq. (4.1) is that $k_{//}$ diverges when $\sqrt{\epsilon_{II}}k_0 h \to \pi/2$. This gives a criteria for the cutoff frequency of the SPS which is given by

$$\sqrt{\epsilon_{II}}h = \frac{\lambda_0}{4}, \tag{4.2}$$

and it gives an estimate for the operating frequency range of the SPS. In addition, from Eq. (4.2), it can be seen that a deeper groove will cause the spoof plasmon be more confined at a given frequency as shown in Fig. 4.1 by the dispersion relations for $a = 30$ $\mu$m and $h = 30$ $\mu$m (blue line) and $a = 30$ $\mu$m and $h = 40$ $\mu$m (green line). Note that Eq. (4.2) is valid only for the first spoof plasmon mode. For an SPS with deeper grooves, higher order spoof plasmon modes can be supported as shown by Jiang *et al.* [160].

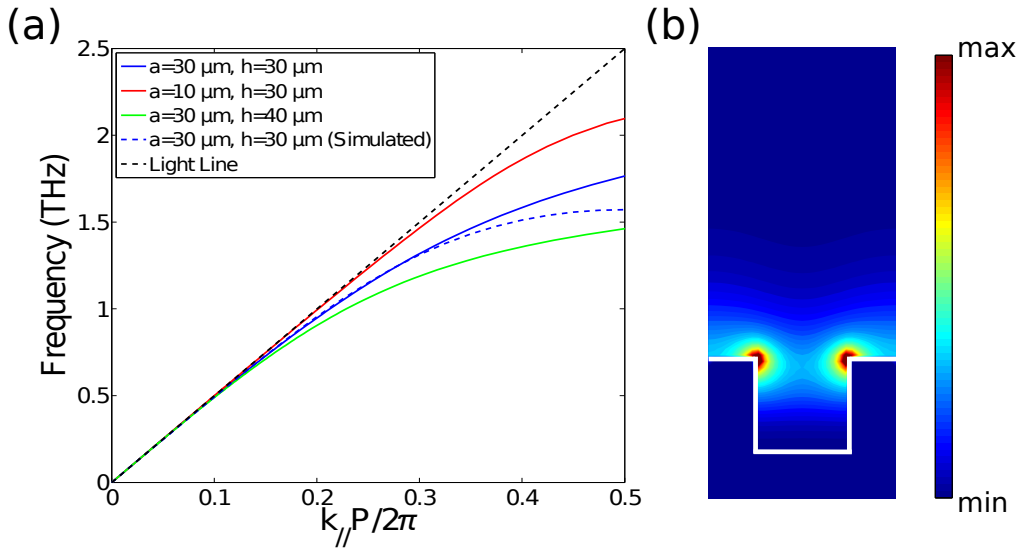



Figure 4.1: (a) Analytical spoof plasmon dispersion relations for a linear array of square PEC grooves with $a = 30$ $\mu$m and $h = 30$ $\mu$m (blue line), $a = 10$ $\mu$m and $h = 30$ $\mu$m (red line) and $a = 30$ $\mu$m and $h = 40$ $\mu$m (green line). The simulated spoof plasmon dispersion for $a = 30$ $\mu$m and $h = 30$ $\mu$m is depicted as the blue-dashed line. The light line is given by the black-dashed line. (b) Electric energy density around the groove at the Brillouin zone edge for $a = 30$ $\mu$m and $h = 30$ $\mu$m. The white line demarcates the groove.

The blue-dashed line in Fig. 4.1(a) shows the simulated spoof plasmon dispersion for $a = 30$ $\mu$m and $h = 30$ $\mu$m, calculated using the Eigenmode solver in the commercial software CST Microwave Studio. Compared to the analytical solution given by the blue line, the simulated solution is noticeably different near the Brillouin zone edge (i.e. $k_{//}P/2\pi = 0.5$) due to the fact that Eq. (4.1) does not take into account diffraction effects which come into play [146]. Nonetheless, one can see that

both simulated and analytical curves agree reasonably well with each other. The analytical solution can be made to fully agree with the simulated spoof plasmon dispersion by taking into account higher diffraction orders and more waveguide modes in the grooves (see Section 2.5). Figure 4.1(b) shows the corresponding simulated electric energy density in the vicinity of the groove at $k_{//}P/2\pi = 0.5$. The white line demarcates the groove. It is obvious from this plot that the spoof plasmons propagating on the SPS are very tightly confined to the surface of the SPS.

Using the definition of confinement length (see Eq. (2.50)) together with Eq. (4.1), the confinement of the spoof plasmons to the SPS surface can be simply written as,

$$L_z = (k_0)^{-1} \left( \frac{1}{\epsilon_{II}} \left( \frac{a}{P} \right)^2 \tan^2 \left( \sqrt{\epsilon_{II}} k_0 h \right) \right)^{-1/2}, \tag{4.3}$$

and is plotted in Fig. 4.2 for the $a = 30$ $\mu$m and $h = 30$ $\mu$m case. For example, at 1.5 THz, the electromagnetic fields are confined to a region that is of the order of $\lambda_0/4$ (or less since the simulated dispersion curves which take into account all diffraction orders and waveguide modes show that the spoof plasmons are actually more strongly confined than analytically suggested near the Brillouin zone edge).

This tight confinement of fields in the vicinity of the SPS surface means that the spoof plasmons are very sensitive to changes in the dielectric environment. Thus the potential of spoof plasmons for sensing begins to become clear at this stage. In the rest of this chapter, the first steps taken in this PhD towards actually applying spoof plasmons to THz sensing are described.

## 4.3 OPTICAL LITHOGRAPHY OF METALLIZED SUB-WAVELENGTH GROOVE ARRAYS

Our SPS, consisting of a linear array of subwavelength grooves (shown in Fig. 4.3(a)), was fabricated by Dr. Jianfeng Wu (National University of Singapore) via conventional UV photolithography of a positive photoresist on a glass substrate. A thick

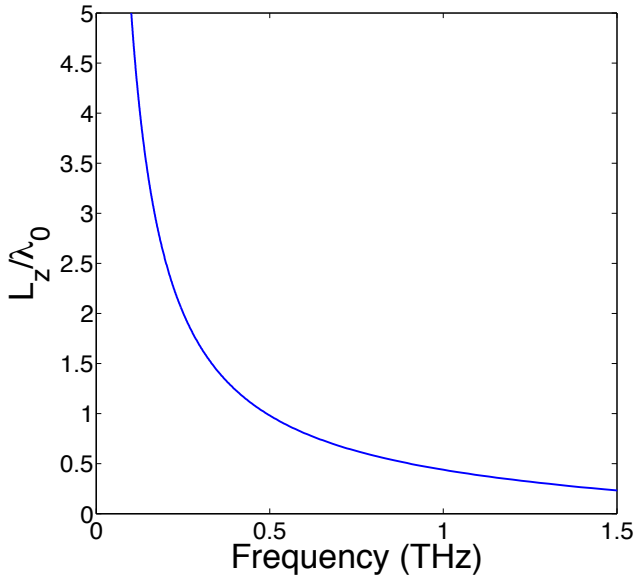



Figure 4.2: Confinement length $L_z$, of spoof plasmons on square PEC grooves with $a = 30\ \mu$m and $h = 30\ \mu$m.

layer of AZ 9620 positive photoresist was first coated onto a glass substrate via a two-step spin coating process. In the first spin coating step, the AZ 9620 was spun at 1350 RPM for 1 min followed by a soft bake at 110°C for 80 seconds. The second spin coating step was performed at the same spin speed followed by a soft bake at 110°C for 180 seconds, giving a final photoresist thickness of approximately 28 $\mu$m. The photoresist is then exposed to UV light ($\lambda = 405$ nm) via a pre-fabricated photomask in a mask & bond aligner (Karl Suss, MA8/BA6) with a dosage of 1000 mJ cm$^{-2}$ and developed with AZ 400K developer to reveal the photoresist groove array. Lastly, 600 nm of gold is sputtered onto the photoresist groove array (AJA International Inc., ATC 1800V) to give the final SPS with an overall sample area of 18 mm$\times$34 mm. As the gold layer is much thicker than the skin depth of gold at THz frequencies ($\sim$ 80 nm at 1 THz), the final structure closely approximates a corrugated PEC surface.

Figure 4.3(b) shows an optical microscope image of the fabricated SPS with the following dimensions as labelled in Fig. 4.3(a): $h = 27\,\mu$m, $w_t = 37\,\mu$m, $w_b = 25\,\mu$m

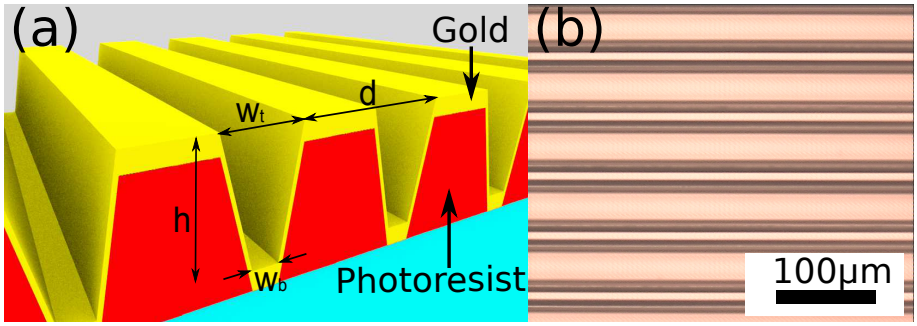



Figure 4.3: (a) 3D image of spoof plasmon metamaterial. The red region depicts the photoresist grooves and the yellow region depicts the gold film. (b) Optical microscope image of the fabricated groove array.

and $d = 60\,\mu$m. A period of $60\,\mu$m implies that diffraction effects are only manifested above 2.5 THz. Below this frequency the SPS features are subwavelength and the SPS operates within the so-called metamaterial regime. The slanted walls of the grooves are a consequence of the photolithography of the thick photoresist layer which results in photoresist at the top receiving more UV light exposure than at the bottom. This, undoubtedly, will affect the spoof plasmon dispersion as the waveguide modes propagating within the slanted-wall grooves are of a different nature from those propagating in square grooves owing to the fact that the groove width experienced by the fields varies with the depth in the case of the slanted walls. As can be seen in Fig. 4.4, the spoof plasmon on a slanted-wall groove SPS (red line) is less confined that that of a square groove SPS. This reduction in confinement can be intuitively understood by the fact that, in the case of the slanted-wall grooves, the waveguide modes have a greater tendency to be reflected upwards as they propagate within the groove due to a change in groove width with depth.

## 4.4 OTTO PRISM COUPLING TO SPOOF PLASMONS

Spoof plasmons, being bound modes (i.e. they exist below the light line), cannot be coupled into from free space propagating light directly; they need to be phase-matched using a coupling mechanism. Here, we have chosen the conventional Otto

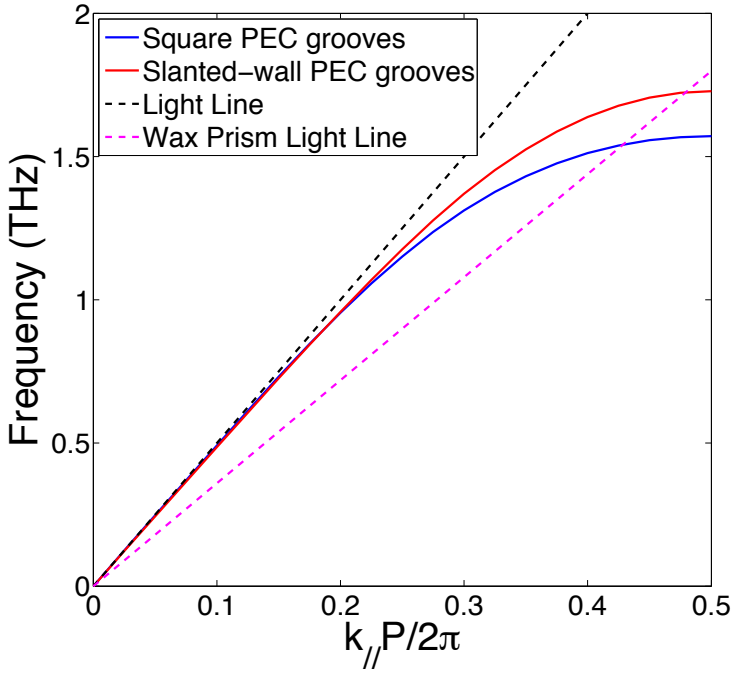



Figure 4.4: Spoof plasmon dispersion of square (blue) and slanted-wall (red) PEC grooves. The slanted-wall groove SPS dispersion relation was obtained by simulating a periodic groove with the geometrical parameters of our SPS in CST Microwave Studio. The black- and magenta-dashed lines give the light line in air and the wax prism, respectively.

prism configuration to couple THz radiation into spoof plasmons on our SPS, as shown in Fig. 4.5(a) [161, 162]. The prism used is a right angled triangular prism made of wax with a refractive index $n_p$, of 1.446. THz radiation from a THz-TDS undergoes Total Internal Reflection (TIR) at the base of the prism and couples evanescently to spoof plasmons on the SPS across a coupling gap $g$ (see Fig. 4.5(a)). Resonant coupling to spoof plasmons occurs when the phase-matching condition given by

$$n_p k_0 \sin\theta_i = k_{//}, \tag{4.4}$$

where $\theta_i \approx 74°$ is the angle of incident from the normal of the base of the prism and $k_{//}$ is the spoof plasmon propagation constant, is met. The Otto prism configuration has previously been used to couple to semiconductor SPPs and surface modes on metallic surfaces in the microwave and THz regime [50, 51, 121, 163–165]. In the case

of Otto prism coupling to semiconductor SPPs, the observed resonance features tend to be quite broad due to high inherent material losses [50, 51]. Thus semiconductor SPPs are not well suited to detect small refractive index changes, which is why we opted to use SPSs instead.

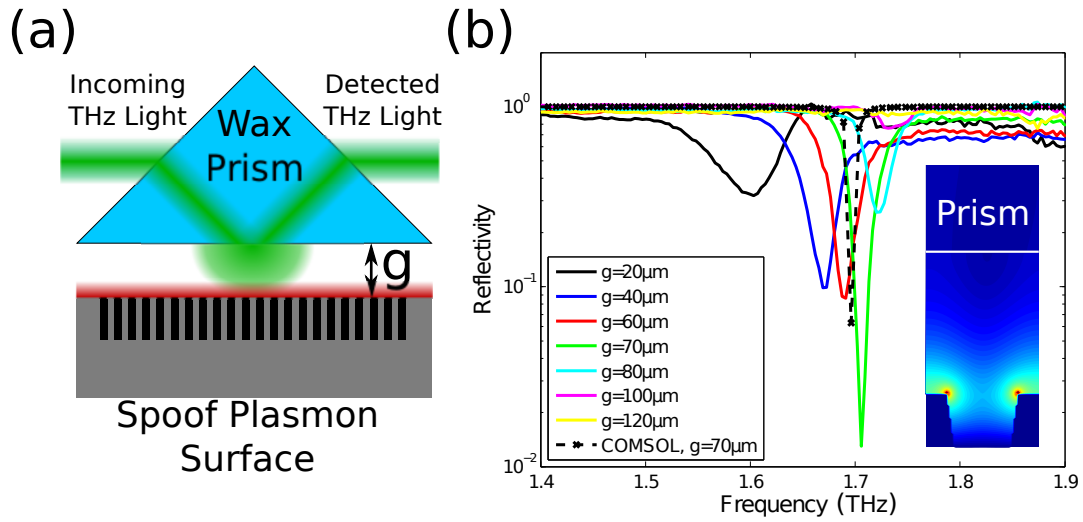



Figure 4.5: (a) Schematic of the Otto Prism setup. (b) Experimental reflectivity spectra for $g = 20\,\mu$m (black), $40\,\mu$m (blue), $60\,\mu$m (red), $70\,\mu$m (green), $80\,\mu$m (cyan), $100\,\mu$m (magenta) and $120\,\mu$m (yellow). Simulated (dashed-cross, black) reflectivity spectrum at strongest spoof plasmon coupling point ($g = 70\,\mu$m) is also shown for comparison. The fluid in the grooves is nitrogen. (Inset) Simulated field distribution at 1.70 THz for $g = 70\,\mu$m. The white line demarcates the prism-coupling gap interface.

The entire Otto prism setup was placed in a nitrogen-purged chamber of a quasi-optical THz-TDS (see Appendix A) and measurements were carried out at less than 5% relative humidity and a frequency resolution of approximately 7 GHz. Changes in reflectivity $R$, and phase $\phi$, can then be monitored by taking the Fourier transform of the time-domain data measured by the THz-TDS. The experimental reflectivity was calculated by normalising the signal reflected off the prism base with the SPS at a coupling gap $g$, beneath the prism $E(\omega, g)$, to the signal in the absence of the SPS beneath the prism, $E(\omega, g \to \infty)$, as given by

$$R = \left| \frac{E(\omega, g)}{E(\omega, g \to \infty)} \right|^2 . \tag{4.5}$$

Dips in the reflectivity spectrum are related to destructive interferences between the incident light, light coupled into spoof plasmons as well as light out-coupled from spoof plasmons into free space radiation [161,162]. They are clear indications of the resonant coupling between THz radiation and spoof plasmons.

The phase change spectrum $\Delta\phi$, is given by the difference in phase of each frequency component of the Fourier transform between the sample and the reference,

$$\Delta\phi = \phi_{sam} - \phi_{ref}, \tag{4.6}$$

where $\phi_{sam}$ and $\phi_{ref}$ are the phase components of the Fourier coefficients of the sample and reference, respectively. Typically, one would expect to see a jump in phase at the resonance frequency [166].

Figure 4.5(b) shows the reflectivity spectra for various $g$ values as well as the simulated reflectivity spectrum at $g = 70$ $\mu$m. Firstly, the reflectivity dips due to resonant coupling to spoof plasmons red-shifts and broadens as the coupling gap is reduced. This is linked to an increase in the effective refractive index of the immediate environment of the SPS. The spoof plasmons coupled via the Otto prism configuration is a *leaky* mode. In other words, since the evanescent light from the prism base can interact with the SPS, the spoof plasmons could likewise extend far enough above the SPS to interact and couple back into propagating light in the prism as well. Thus as the prism is brought closer to the SPS, the spoof plasmon frequency reduces due to the presence of the prism which increases the effective refractive index in the vicinity of the SPS. Coincidentally, this also means that the spoof plasmon has a greater chance of coupling into free space light in the prism and the spoof plasmon lifetime also decreases as the prism is brought closer to the SPS. Thus a broadening of the reflectivity dip is also observed at small $g$ values. At $g = 120$ $\mu$m, almost no dip in reflectivity is observed, indicating that the interaction between the evanescent field from the prism base and the SPS is negligible. In addition, the experimental spoof plasmon frequency $f_{sp}$, is in good agreement with

the prediction from bandstructure calculations (CST Microwave Studio) which gives $f_{sp} = 1.72$ THz, given an experimental frequency resolution of around 16 GHz (see Fig. 4.4, intersection point of slanted-wall PEC grooves dispersion (red-solid line) and prism light line (magenta-dashed line)).

Secondly, we note that the strongest reflectivity dip occurs at the spoof plasmon frequency $f_{sp} = 1.71$ THz for $g = 70$ $\mu$m (green line in Fig. 4.5). This is in good agreement with simulations which predict $f_{sp} = 1.70$ THz at $g = 70$ $\mu$m (black-dashed line in Fig. 4.5). The theoretical reflectivity spectrum was calculated using the commercial software COMSOL Multiphysics with a single groove as the unit cell and Floquet periodic boundary conditions. The surface of the groove was simulated using the surface impedance boundary condition (assuming a Drude permittivity with plasma frequency $\omega_p = 1.367 \times 10^{16}$ rad s$^{-1}$, and collision frequency $\gamma = 4.072 \times 10^{13}$ rad s$^{-1}$), instead of a PEC boundary condition. This was done because COMSOL Multiphysics does the calculation in the frequency domain (i.e. an infinite time period is considered) and if the PEC boundary condition was used all the energy coupled into spoof plasmons would eventually be coupled out resulting in no dip in the reflectivity.

Lastly, it can be seen that the experimental reflectivity dip for $g = 70$ $\mu$m, with a FWHM $\Delta f_{sp}$, of 40 GHz and a Q-factor of approximately 43, is broader and deeper than its simulated counterpart. This broadened resonance is indicative of a shorter spoof plasmon lifetime which means that there are some experimental damping mechanisms which are not fully reflected in our calculations. The deepening of the dip means that these damping channels do not contribute to the SPS reflectivity and can be related to absorption losses such as those due to hot spots at surface imperfections and to diffraction effects caused by the scattering of spoof plasmons at the edges of the sample. On top of that, we note that not all the light out coupled from spoof plasmons can be collected due to the symmetry of the Otto prism setup

and the silicon lenses used in the emitter and detector (see Appendix A), unlike in simulations where all free space propagating light is collected by the monitor.

The inset of Fig. 4.5(b) shows the simulated field distribution at 1.70 THz for $g = 70\ \mu$m. It can be seen that the fields are tightly confined to the SPS surfaces and are well removed from the prism base demarcated by the white line. This relatively high Q-factor (even in the experimental case) means that the spoof plasmons can potentially be used in sensing applications.

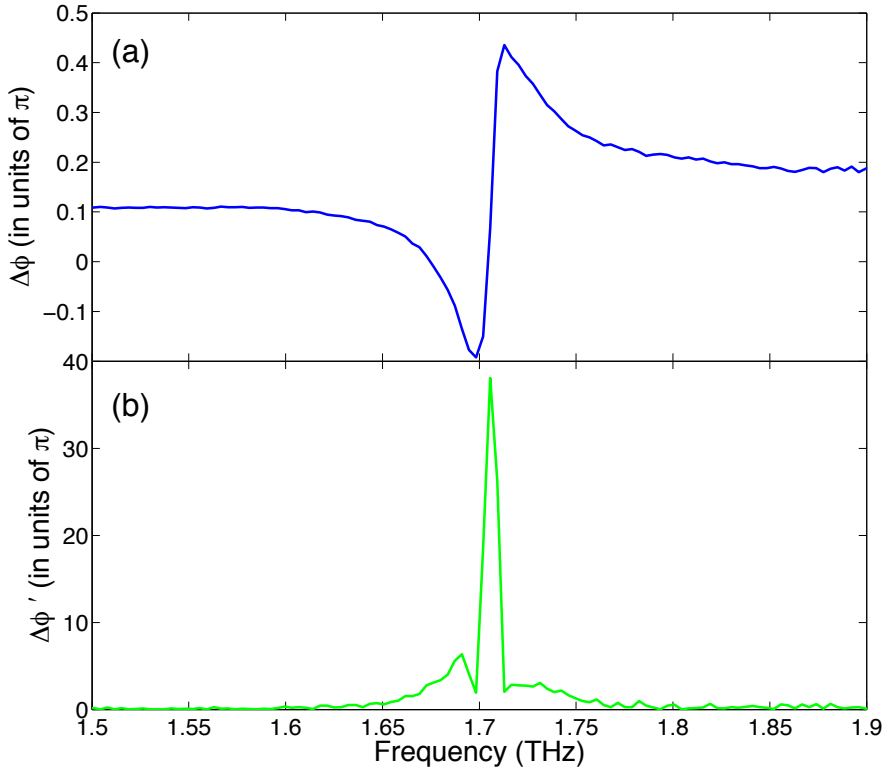



Figure 4.6: Phase change $\Delta\phi$ (a), and absolute gradient of $\Delta\phi$, $\Delta\phi' = |d(\Delta\phi)/df|$ (b) at $g = 70\,\mu$m. Reprinted with permission from [167]. Copyright 2013, Wiley.

Before proceeding on to SPS refractive index sensing, we draw the reader's attention to an oft-neglected source of information in THz metamaterials research, the phase of the electromagnetic fields. Figure 4.6 shows the change in phase between the sample and reference spectra $\Delta\phi$ (see Fig. 4.6(a)) and the absolute gradient of phase change

$\Delta\phi' = |\mathrm{d}(\Delta\phi)/\mathrm{d}f|$ (see Fig. 4.6(b)) for $g = 70$ $\mu$m. A sharp phase change takes place at $f_{sp}$, whereby $\Delta\phi$ exhibits a Fano-like lineshape (see Fig. 4.6(a), blue line). This sharp phase change can be used as the readout response by which refractive index sensing can be carried out, instead of the conventional amplitude response. The absolute gradient of the phase change $\Delta\phi'$, shown by the green line in Fig. 4.6(b) exhibits a sharp peak at $f_{sp}$, corresponding to the sharp phase change. The width of this peak is around 10 GHz, giving a $f_\phi/\Delta f_\phi$ (analogous to the Q-factor) value of 170, where $f_\phi$ and $\Delta f_\phi$ are the peak position and the width of the peak in $\Delta\phi'$, respectively. Note that this peak is four times sharper than its counterpart in amplitude measurements, making phase change a very effective indicator for the SPS to detect small changes in the refractive index of the material filling the groove (recall the definition of FOM in Chapter 3).

## 4.5 NARROWBAND REFRACTIVE INDEX SENSING ON THE SPS

The grooves of the SPS are filled with nitrogen ($n = 1.00$, control), gasoline ($n \approx 1.41$), liquid paraffin ($n \approx 1.49$), glycerin ($n \approx 1.82$) and water ($n \approx 2.1$) as a demonstration of THz spoof plasmon refractive index sensing. The fluids used here provides us with a good spread of refractive index values, enabling us to investigate the efficacy of SPS sensors when subjected to a wide range of refractive index and loss conditions. For example, water has a high refractive index and also extremely high loss [3, 16].

$R$ and $\phi$ were again monitored as the fluids filling the grooves are changed. For all the fluids, $g$ was kept constant at 70 $\mu$m where the strongest spoof plasmon coupling takes place in the case of nitrogen. The samples were washed with deionised water and an additional measurement was taken between different fluids to ensure that the spoof plasmon coupling point remains the same as the nitrogen case (control sample). The reason why $g$ was kept constant will be discussed later in this section.

Figure 4.7 shows the dispersion relation of the spoof plasmons as the SPS grooves are filled with the various fluids calculated using the Eigenmode Solver in CST Microwave Studio. According to Eq. (4.4), $f_{sp}$ is given by the intersection point between the prism light line and the respective spoof plasmon dispersion curves. The predicted $f_{sp}$ for nitrogen, gasoline, liquid paraffin, glycerin and water are 1.72 THz, 1.49 THz, 1.44 THz, 1.28 THz and 1.14 THz, respectively and are summarised in Table 4.1.

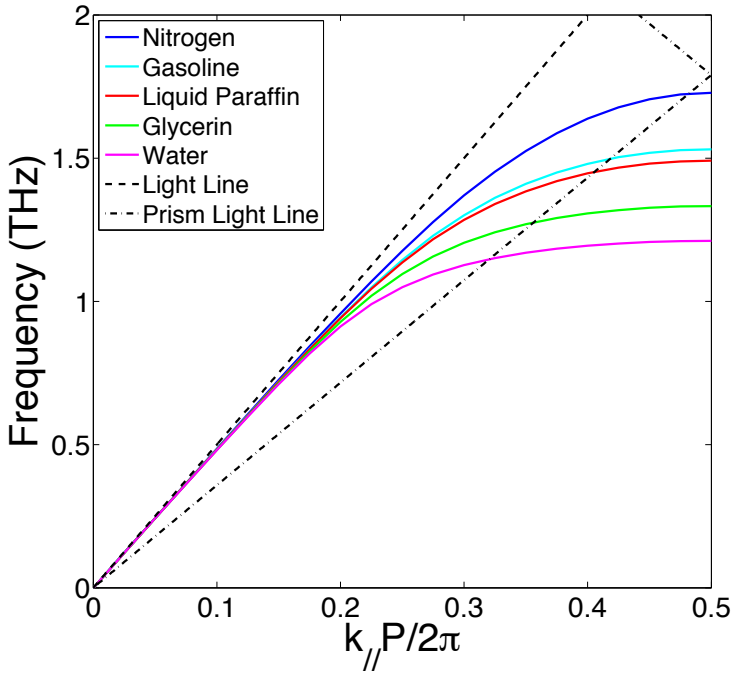



Figure 4.7: Calculated spoof plasmon dispersion relations for nitrogen (blue), gasoline (cyan), liquid paraffin (red), glycerin (green) and water (magenta). The light line in air and the prism are given by the black-dashed and black-dash-dot lines, respectively. The dispersion relations were calculated using the Eigenmode Solver in CST Microwave Studio.

Figure 4.8 plots the reflectivity spectra for the various fluids. It is obvious that as the refractive index of the fluid filling the SPS grooves increase, the reflectivity dip red-shifts. The resonance points are 1.71 THz, 1.53 THz, 1.48 THz, 1.30 THz and 1.17 THz for nitrogen, gasoline, liquid paraffin, glycerin and water, respectively (see Table 4.1). As can be seen, the experimental $f_{sp}$ is in good agreement with

Table 4.1: Table of calculated and experiment $f_{sp}$ for the various fluids

| **Fluid Sample** | **Calculated $f_{sp}$ (THz)** | **Experimental $f_{sp}$ (THz)** |
|---|---|---|
| Nitrogen | 1.72 | 1.71 |
| Gasoline | 1.49 | 1.53 |
| Liquid Paraffin | 1.44 | 1.48 |
| Glycerin | 1.28 | 1.30 |
| Water | 1.14 | 1.17 |

the calculated ones, given a frequency resolution of around 10 GHz in the experimental THz-TDS spectra. For low loss fluids, such as gasoline and liquid paraffin, the widths of the resonance $\Delta f_{sp}$, are 90 GHz and 50 GHz, respectively. As the losses due to the fluid increases, such as for glycerin, the reflection dip broadens significantly to 280 GHz, yielding a Q-factor of around 4.6. With a fluid of very high loss, such as water, $\Delta f_{sp}$ further increases to approximately 390 GHz. Thus, refractive index sensing with amplitude measurements might not be a good option for fluid with high losses. This is because the significant broadening will require a larger refractive index change in order to properly discern any spectral shifts (recall the definition of *FOM* in Chapter 3). Nonetheless, compared to sensing via resonance metamaterials in transmission mode, our Otto prism coupled spoof plasmon sensing concept represents a relevant improvement since the THz signal after passing through a high loss fluid layer would be greatly attenuated, leading to a low signal-to-noise ratio [92–94, 153, 156, 168, 169].

The phase change $\Delta\phi$ spectra for the various fluids are given in Fig. 4.9. The first thing to note is that all the fluids exhibit a phase jump at $f_{sp}$. However, this is not the best way to visualise and compare the results as the $\Delta\phi$ spectra all have different starting points. The difference in starting points is caused by slight differences in sample positions relative to the prism and the prism position relative to the beam, resulting in different *absolute* phases when the sample and reference measurements were made. In order to compare the results, the phase change spectra have to be

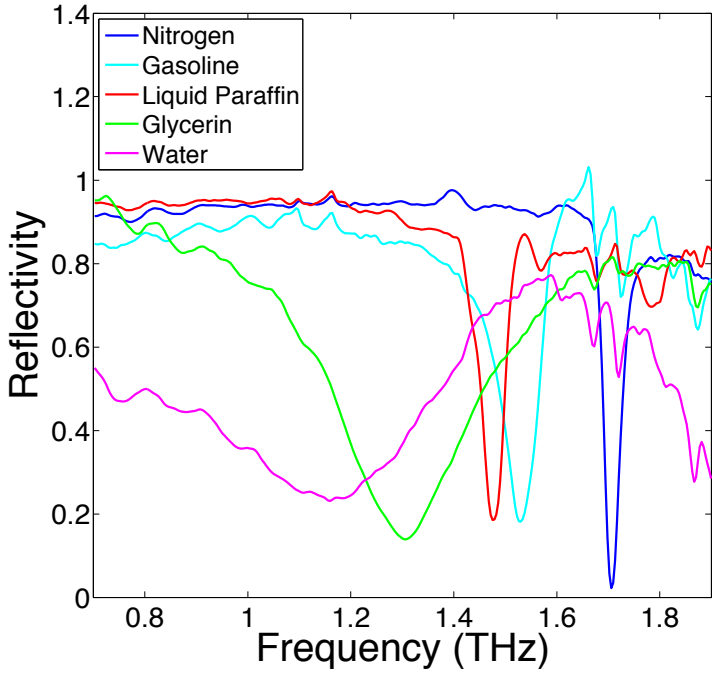



Figure 4.8: Reflection spectra of sample fluids (nitrogen (blue), gasoline (cyan), liquid paraffin (red), glycerin (green) and water (magenta)) at $g = 70\,\mu$m. Reprinted with permission from [167]. Copyright 2013, Wiley.

able to be plotted on the same scale.

To do this, the absolute gradient of phase change $\Delta\phi'$, obtained using fitted $\Delta\phi$ data, is plotted in Fig. 4.10. The phase jumps will then appear as peaks while at the frequencies adjacent to $f_{sp}$, $\Delta\phi'$ will be flat. In this way, the phase jump spectra for all the fluids can be plotted on a common axis and compared. The $\Delta\phi'$ spectra (with the exception of nitrogen) are magnified to enable easy reading. This is because losses in the fluids result in a smaller and more gradual overall phase jump at resonance and hence a smaller $\Delta\phi'$ peak. Remarkably all the peaks in Fig. 4.10 are narrower than the reflectivity dips in Fig. 4.8. The $f_\phi/\Delta f_\phi$ values for nitrogen, gasoline, liquid paraffin, glycerin and water are approximately 170, 44, 78, 18 and 7, respectively. Note that these values are at least twice the Q-factors of the amplitude measurements. In particular, the $f_\phi/\Delta f_\phi$ values for nitrogen and glycerin

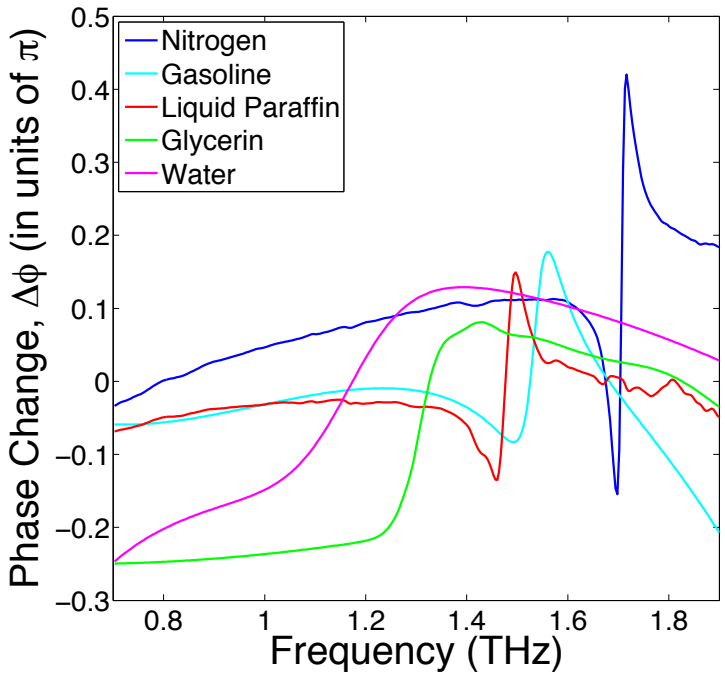



Figure 4.9: Phase change $\Delta\phi$ spectra for nitrogen (blue), gasoline (cyan), liquid paraffin (red), glycerin (green) and water (magenta).

are 4 times as high as its equivalent for amplitude measurements. Our experimental results indicate that the problem of broadening due to losses is mitigated when using phase jumps as the readout response.

A Figure-of-Merit, similar to Eq. (3.1), is then defined as

$$FOM = \frac{1}{\Delta f_{sp}} \frac{\mathrm{d}f_{sp}}{\mathrm{d}n}, \tag{4.7}$$

where $f_{sp}$ is the spoof plasmon frequency, $\mathrm{d}f_{sp}/\mathrm{d}n$ is the change in resonance frequency per refractive index unit (RIU) and $\Delta f_{sp}$ is the width of the resonance. This $FOM$ was calculated for each fluid to quantitatively evaluate our SPS sensor.

The resonance frequencies of the SPS when filled with various fluids are plotted in Fig. 4.11. The blue line shows the linear fit to the experimental data and is given by $f_{sp} = -0.49n + 2.21$, from which we can deduce the sensitivity of the system $\xi = \Delta f_{sp}/\Delta n$ to be 0.49 THz / RIU. Also, if we assume a detection resolution of 10

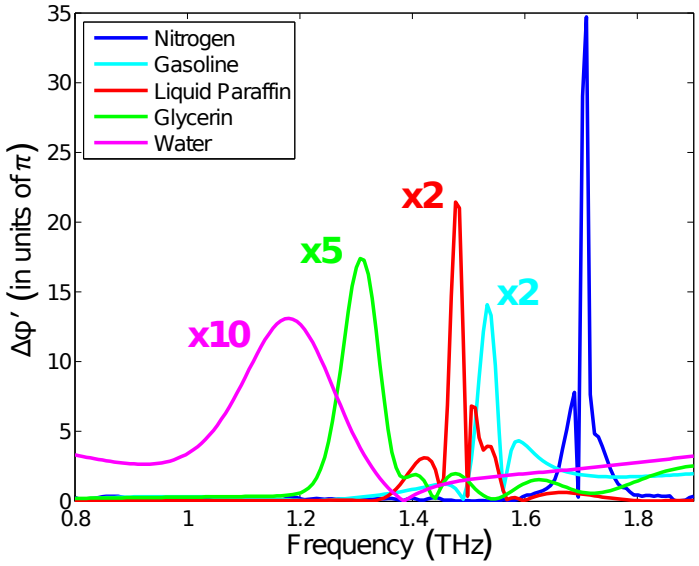



Figure 4.10: Absolute gradient of phase change spectra $\Delta\phi'$ for nitrogen (blue), gasoline (cyan), liquid paraffin (red), glycerin (green) and water (magenta) obtained from fitted $\Delta\phi$ data. The $\Delta\phi'$ spectra for fluids other than nitrogen are magnified for clarity. Reprinted with permission from [167]. Copyright 2013, Wiley.

GHz, the detection limit, which is the minimum change in refractive index that can be detected, is 0.02 RIU. The sensitivity featured in our SPS is higher than previously reported in similar devices [93]. The *FOM* values calculated using Eq. (4.7) for nitrogen, gasoline, liquid paraffin and glycerin are 49, 15, 25 and 7, respectively (see Table 4.2), and are much higher than that presented in Chapter 3 [151] as well as those of THz metamaterial sensors based on SRRs or asymmetric SRRs previously reported in Refs. [91, 92, 94, 157, 170]. This indicates an improvement in the sensing performance of our spoof plasmon sensing approach relative to traditionally proposed THz metamaterial sensors. This is because rather than rely on specific field hot spots to detect refractive index changes (as is the case for SRRs), the SPS generates high field enhancements over many grooves, thus resulting in a large effective interaction volume between the light and fluids. The *FOM* values were calculated using the phase jump spectra data for $\Delta f_{sp}$. Thus we can see that the high *FOM* values were mediated by the sharpness of the phase jumps and the

SPS sensing approach proposed here can be very promising for application in areas where fluids are generally low loss such as the petroleum industry [171]. This is in contrast to the generally broad SPP resonances on semiconductor surfaces, where absorption losses can significantly decrease SPP lifetimes [50, 51]. The *FOM* value for water is only 3 and is lower than the other fluids because it is extremely lossy. However, water often is an insurmountable obstacle when it comes to other forms of THz spectroscopy [3]. Hence, our result here shows that refractive index sensing can still be carried out despite high losses, albeit not as well as compared to the other fluids.

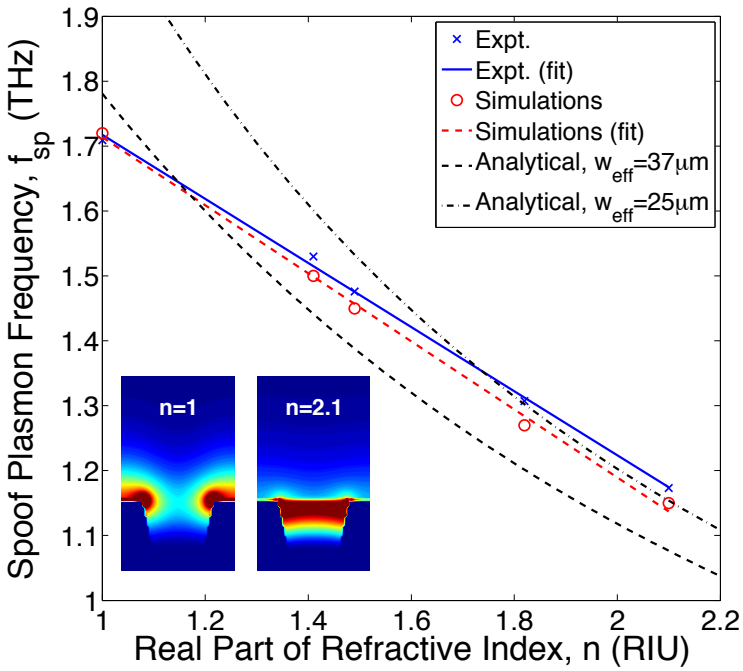



Figure 4.11: Resonance frequencies of various fluids, $f_{sp}$ at $g = 70\,\mu$m plotted against refractive indices for experiments (blue solid, cross), simulations (red dashed, open circle) and analytical expressions with $w_{eff} = 37\ \mu$m (black, dotted) and $w_{eff} = 25\ \mu$m (black, dash-dot). (Inset) Electric energy density distributions for $n = 1$ and $n = 2.1$ at $f_{sp}$. Reprinted with permission from [167]. Copyright 2013, Wiley.

The red-open circles in Fig. 4.11 are the calculated $f_{sp}$ as summarised in Table 4.1. The linear fit to the calculated data is given by the equation $f_{sp} = -0.52n + 2.24$

Table 4.2: Summary of Figure-of-Merits for the various fluids tested.

| **Sample Fluid** | **Figure-of-Merit** |
|---|---|
| Nitrogen | 49 |
| Gasoline | 15 |
| Liquid Paraffin | 25 |
| Glycerin | 7 |
| Water | 3 |

and is in good agreement with the experiments.

We can compare the experimental and simulation results to analytical expectations by referring back to Eq. (4.1), which gives the spoof plasmon dispersion relation for square PEC grooves. The $f_{sp}$ given by the intersection between the prism light line and Eq. (4.1) (see Eq. (4.4)) is solved numerically for the cases of square PEC grooves with an effective width of 37 $\mu$m (i.e. $w_t$) and 25 $\mu$m (i.e. $w_b$) and plotted as the black-dashed and black-dashed-dot lines in Fig. 4.11, respectively. The two analytical cases calculated represent the theoretical limits to the experimental case. As can be seen, the experimental results fall within the bounds of the two analytical curves in Fig. 4.11. The lower (higher) bound is given by the 37 $\mu$m (25 $\mu$m) case as expected from Eq. (4.1). By taking the numerical gradient of the analytical curves, we find the minimum analytical expectations for the sensitivity of the SPS to be 0.40 THz / RIU and 0.47 THz / RIU for the 37 $\mu$m and 25 $\mu$m cases, respectively. Again, these values are similar to that obtained from experiment. We also note that the sensitivity values given by the analytical curves can be higher than experimentally obtained, such as near $n = 1$. This means that SPS-based sensors can potentially be improved or engineered to give better sensing performances than reported here.

One difference between the experimental and analytical results is that the analytical curves follow a $1/n$ trend due to the tangent term in Eq. (4.1) while the trend observed in our experiments is obviously quite linear. The reason for this is because

the slanted walls of the grooves in the experiments result in a varying groove width with the groove depth. We can understand the effect of the slanted walls by looking at the electric energy density distribution in the grooves for a groove refractive index of $n = 1$ and $n = 2.1$ at their respective $f_{sp}$, shown as the insets of Fig. 4.11. For $n = 1$, we can see that the electric energy is concentrated at the top of the groove while for $n = 2.1$, the electric energy resides mainly in the groove. In other words, at $n = 1$, the fields *feel* an effective groove width closer to $w_t$ while at $n = 2.1$ the effective groove width is more similar to $w_b$. This explains why the experimental results are similar to the 37 $\mu$m analytical case near $n = 1$ while the SPS behaviour near $n = 2.1$ approximates square PEC grooves with an effective width of 25 $\mu$m.

Having presented the results obtained from our experiments, it is now a good time to explain the rationale behind keeping $g$ constant. For the work presented in this chapter, the sensing scenario envisioned is one where a known reference fluid (namely nitrogen) is compared to an unknown fluid while keeping all parameters constant. Of course, there are numerous other ways one can conduct spoof plasmon sensing with an Otto prism configuration. One can also, for example, look for the optimum $g$ which gives the strongest coupling for each fluid. Doing this would probably result in better *FOM* due to sharper phase jumps but would not change the sensitivity values by much since $f_{sp}$ does not change much for gaps larger than that which gives the deepest reflectivity dip. This was not done because the THz-TDS used in this experiment has a slow mechanical delay line (see Appendix A.3) which would have made measurements for searching for the optimal $g$ prohibitively long. More importantly, the overall conclusion that SPS can deliver better performance sensing even for high loss fluids as compared to other metamaterial sensing approaches would have remained the same.

## 4.6 NARROWBAND DATA: SURELY THIS CAN'T BE ALL?

In this chapter, the results on THz spoof plasmon refractive index sensing using an Otto prism coupling scheme were presented, with good agreement between theory and simulations. Phase jumps at resonant coupling to spoof plasmons were used as the readout response to deliver superior sensing performance. A $FOM$ as high as 49 was achieved for lossless fluids and $FOM$ values around 20 can be expected for low loss fluids such as gasoline. It is even shown that refractive index sensing might be tenable for high loss fluids such as water. In addition, the SPS sensor can be tailored to the sensing requirements by using alternative geometries such as annular holes [128] or complementary SRRs [127]. Lastly, it is not difficult to see the potential for SPS sensors to be integrated with microfluidics or surface functionalisation to conduct material characterisation that is complementary to other techniques such as mid-IR spectroscopy.

The question that then follows is: *is that all we can do with spoof plasmons?* Sensing can be divided into two broad categories that are epitomised by two questions.

1. *How much is there?* This is the question asked when an unknown analyte is compared to a known reference. A change in sensor response can be attributed to a known change in system conditions via techniques such as surface functionalisation or a prior knowledge of the substances present.

2. *What is present?* In this case, the substances present are unknown. Hence information from a broad range of frequencies are often needed to identify the analytes present.

The first question is usually answered using resonant methods since a change in the resonant response, such as a dip in reflectivity, can be attributed to a known change

in the system, say a change in concentration of an analyte. The work presented in Chapters 3 and 4 belong to this first category.

However the information present in the spoof plasmons is much richer than that. The dispersion relation of a spoof plasmon exists for a broad range of frequencies, not just at the resonant coupling point. If we can couple THz radiation to spoof plasmons over a broad range of frequencies, instead of just one, we can access broadband information about the analytes. This would serve to answer the second question and make SPSs a truly versatile platform on which to conduct THz sensing.

CHAPTER 5

# BROADBAND SENSING WITH SPOOF PLASMON SURFACES

## 5.1 INTRODUCTION

In this chapter, we seek to answer the question of *"what is present?"* when it comes to sensing problems (see Section 4.6). To know what analytes are present in a system, however, presupposes the ability to characterise the substance over a broad range of frequencies (or at least a large number of discrete frequency points). Only then can a *fingerprint* of the substance be obtained. Such fingerprinting, in general, cannot be achieved using the methods proposed in the previous chapters by virtue of the narrowband resonant nature of the sensing mechanism.

Building upon the work presented in Chapter 4 and motivated by the desire to maximise the versatility of spoof plasmons for sensing applications, work was carried out on extracting broadband propagation data from spoof plasmons. Using the scattering edge coupling method [123,172] and short-time Fourier transform (STFT) (see Section 2.6.4), broadband data (0.4 THz to 1.44 THz) was extracted from an SPS consisting of a linear array of subwavelength grooves similar to that of Chapter 4 in a single measurement. Refractive index sensing was then demonstrated for various fluids by monitoring changes in the dispersion as well as attenuation of the spoof plasmons, thus giving access to the real and imaginary parts of the refractive indices of the fluids. This points to the potential for SPSs to fully characterise analytes. At the end of this chapter, a form of THz surface enhanced absorption spectroscopy, using $\alpha$-lactose monohydrate powder as the analyte, is shown as a proof-of-principle demonstration of broadband SPS sensors.

The SPS used in this chapter is similar to that of Chapter 4, with the following geometrical parameters: $P = 60$ $\mu$m, $w_t = 37$ $\mu$m, $w_b = 25$ $\mu$m and $h = 31$ $\mu$m (see Fig. 5.1(a)). The fabrication of the SPS was again undertaken by Dr Jianfeng Wu (National University of Singapore) using the method described in Section 4.3. Figure 5.1(b) shows an optical image of the fabricated SPS.

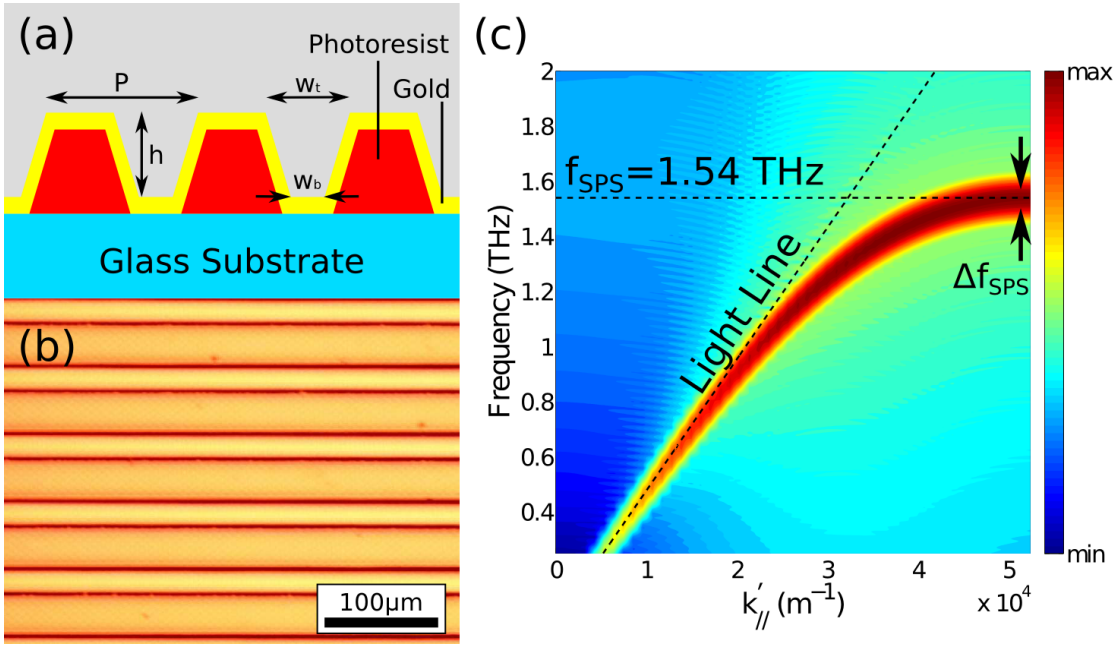



Figure 5.1: (a) Schematic diagram of SPS with $P = 60$ $\mu$m, $h = 31$ $\mu$m, $w_t = 37$ $\mu$m and $w_b = 25$ $\mu$m. The thickness of gold is 600 nm. (b) Optical microscope image of SPS fabricated by photolithography. (c) Calculated bandstructure of SPS. The width of the spoof plasmon mode at the Brillouin Zone edge, $\Delta f_{SPS}$ gives an estimate of the lifetime of the spoof plasmon, $1/\Delta f_{SPS} \approx 20$ ps.

The SPS was designed to operate between 0.2 THz and 2 THz as can be seen by the SPS bandstructure in Fig. 5.1(c). The bandstructure was calculated using the commercial software Lumerical FDTD Solutions and a 2D PEC groove with the same dimensions as our SPS as well as Floquet periodic boundary conditions as the unit cell. Spoof plasmons are excited on the SPS via TM polarised dipole sources placed in the near field of the groove emitting THz radiation between 0.1 THz and

2 THz. Time-domain data, collected using point field monitors located in the near field of the grooves, is then apodized with a Gaussian time window such that the start of the signal, which is due to light not coupled into spoof plasmons, is removed. The remaining time-domain signal is then due to long-lived eigenmodes (i.e. spoof plasmons) and is Fourier transformed to give the frequency of the eigenmodes for a given phase difference between the Flouquet periodic boundaries. As the phase difference is varied from 0 to $\pi/P$ (the first Brillouin zone boundary), the frequency of the eigenmodes can be found to give the bandstructure in Fig. 5.1(c).

From Fig. 5.1(c), we can see that the spoof plasmon dispersion deviates strongly from the light line and saturates at $f_{SPS} = 1.54$ THz, which represents the cutoff frequency of the SPS. Also, the width of the calculated spoof plasmon dispersion at the Brillouin zone edge $\Delta f_{SPS}$, gives us an estimated spoof plasmon lifetime of $1/\Delta f_{SPS} \sim 20$ ps. At lower frequencies, the spoof plasmon dispersion is close to the light line, indicating that the spoof plasmons are ill-confined and propagate close to $c_0$. Another important point, as shall be seen later, is that within our frequency of interest (up to 2 THz), there is only one bound mode supported by our SPS.

## 5.3 SCATTERING EDGE COUPLING TO SPOOF PLASMONS

The scattering edge coupling method is used here to couple THz radiation into spoof plasmons. THz radiation from a THz-TDS is scattered off a sharp razor blade edge and coupled into a spoof plasmon as shown in Fig. 5.2(a). After propagating for a distance $D$, the spoof plasmon is scattered off a second razor blade into free space radiation which is then collected by a detector. An image of the actual scattering edge coupling setup is shown in Fig. A.6(b). This method of coupling is fundamentally different from the Otto prism configuration utilised in Chapter 4 as we are looking at the light that is being coupled into the system by the incident THz radiation and having propagated as spoof plasmons, instead of what is the frequency and amount of light being *taken out* as is the case for the Otto prism. One more thing to note

is that since the characterisation of the SPS is carried out in the time-domain (i.e. the excitation light is a short electromagnetic pulse), the spoof plasmon is in fact also a pulse in time which we shall call a spoof plasmon pulse here for convenience (see Fig. 5.2(b), blue line).

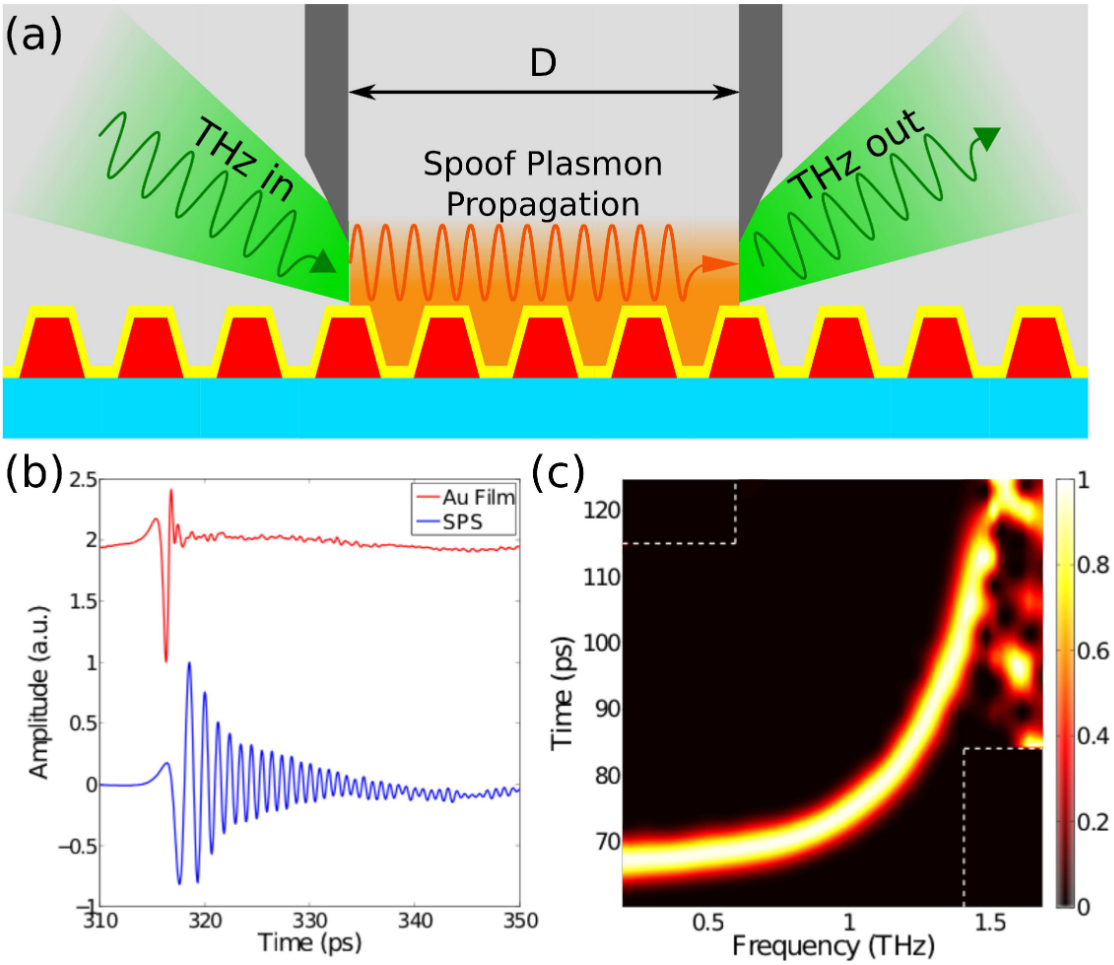



Figure 5.2: (a) Diagram of the scattering edge coupling configuration. (b) Scattering edge coupled time-domain signal of an Au film (red line) and SPS (blue line) with $D = 8$ mm. The time-domain signals are vertically displaced from each other to facilitate easy reading. (c) Filtered spectrogram of SPS with $D = 8$ mm. The time-frequency filters demarcated by the white-dashed lines are applied by setting the enclosed region to zero in order to filter out any signal that is not from the spoof plasmons and improve the visibility of the actual spoof plasmon time-frequency curve.

Figure 5.2(b) shows the time-domain signal collected by the THz-TDS when a thick gold film (approximately 200 nm) and the SPS is placed in the scattering edge

coupling setup. Both time-domain signals were normalised to their respective peak values. Note that the time-domain signals are vertically displaced from each other for clarity of presentation. As can be seen, in the case of the gold film, given by the red line in Fig. 5.2(b), a very short pulse is detected as a result of only unconfined and dispersionless Sommerfeld-Zenneck waves propagating on unstructured metallic surfaces at low frequencies [122], as previously mentioned. In contrast, the signal collected from the SPS is very dispersed, indicating that the frequency components of the spoof plasmon pulse propagate at very different velocities. In our experiments, we have ensured that the separation between the razor blades $D$, is greater or equal to 8 mm (i.e. at least 130 groove periods), to allow the frequency components of the spoof plasmon pulse to be sufficiently separated by the time they reach the second razor blade. The gaps between the razor blades and the SPS (flat gold film) were 60 $\mu$m (250 $\mu$m). THz radiation was incident on the razor blade edges at an angle of 30° from the surface of the SPS. The THz-TDS frequency resolution was set to be approximately 16 GHz.

STFT was then applied to the spoof plasmon pulse to analyse the frequency content of the pulse at each time point (see Section 2.6.4). The results of the STFT constitutes a time-frequency plane called a spectrogram $\bar{S}$ which is given by

$$\bar{S} = |S(\tau, \omega)|^2, \tag{5.1}$$

where $S(\tau, \omega)$ is the STFT of the spoof plasmon pulse signal at time $\tau$ (see Eq. (2.57)).

However, as the THz radiation from the THz-TDS has an inherent spectral power distribution (see Fig. A.5(b)), it will not be immediately apparent from $\bar{S}$ what is the dominant frequency component of the spoof plasmon pulse at each $\tau$. Thus $\bar{S}$ is normalised to its maximum magnitude at each frequency $\omega_i$ to give

$$\bar{S}_{norm} = \frac{|S(\tau, \omega_i)|^2}{\max(|S(\tau, \omega_i)|^2)}, \tag{5.2}$$

where $\bar{S}_{norm}$ is the normalised spectrogram. In this way, the dominant frequency component of the spoof plasmon pulse at time $\tau$ can be easily picked out.

Fig. 5.2(c) shows the normalised spectrogram of the SPS for $D = 8$ mm obtained using a 20 ps Blackmann-Harris 4-term window advanced along the raw time-domain signal in 0.6 ps steps. The length of the window was decided by looking at the lifetime of the spoof plasmon mode at the Brillouin zone edge (see Fig. 5.1(c)). The first feature to note is the main curve in the center of $\bar{S}_{norm}$ extending from approximately 68 ps to 120 ps in time and 0.2 THz to approximately 1.5 THz in frequency. This gives the times $\tau$, and the respective frequencies $\omega$, at which most of the electromagnetic energy carried by the spoof plasmons arrive at the detector. Additionally, the amplitude of the spoof plasmon signal $A(\omega, \tau)$, obtained from the unnormalised spectrogram $\bar{S}$, can be used to calculate the attenuation experienced by the spoof plasmon as it propagates on the SPS, as shall be seen later.

It is clear from Fig. 5.2(c) that the frequency components of the spoof plasmon pulse take different amounts of time to traverse the 8 mm separation between the razor blades. For example, the 0.5 THz frequency component arrives at 68 ps while that of 1.4 THz arrives 32 ps later. From the time difference, we can infer the group velocities of the various frequency components of the spoof plasmon pulse and calculate the dispersion relation as described in the next section. One thing to note is that the time coordinates of the spoof plasmon curve in $\bar{S}_{norm}$ is relative to the start point from which the time-domain data is collected and does not represent the actual time taken for the spoof plasmon to propagate $D$. It is the *difference* in time taken that is important here as it tells us the difference in *group velocities* between the frequency components of the spoof plasmon pulse.

Another thing to point out here is that time-frequency filtering, setting the amplitude of the spectrogram to zero within specific time-frequency windows, is employed to improve the visibility for the spoof plasmon curve. For example, the time-frequency filters are demarcated by white-dashed lines in Fig. 5.2(c). This is required due to contributions to the raw time-domain data from light that is

not coupled into spoof plasmons (see Fig. 5.3(a), in the region $f \geq 1.41$ THz and $t \leq 84$ ps) as well as secondary reflections that occur between the razor blades (see Fig. 5.3(a), in the region $f \leq 0.6$ THz and $t \geq 115$ ps). By filtering out the extraneous data we can then clearly pick out the peaks due to the spoof plasmons propagating on the SPS. This is especially obvious when comparing Fig. 5.3(a) and (b) in the region of $f \geq 1.41$ THz and $t \leq 84$ ps. As can be seen, the time-frequency filter enables us to see the spoof plasmon curve at higher frequencies ($\sim 1.5$ THz) and later times ($\sim 110$ ps) more clearly. A closer look at Fig. 5.3(a), which shows the spectrogram for $D = 8$ mm, also reveals that there is an approximately 53 ps time difference between the onset of the spoof plasmon curve and the secondary reflections ($f \leq 0.6$ THz and $t \geq 115$ ps). This is the time it takes for low frequency spoof plasmons to make a round trip between the razor blades at speeds close to $c_0$ (recall that low frequency spoof plasmons are ill-confined and propagate close to speed of light).

Figure 5.4 shows the normalised spectrograms with $D = 8,\ 10$ and 12 mm, with the appropriate time-frequency filters applied. They show how the spoof plasmon time-frequency curve shifts to later times as the distance between the razor blades is increased. Notably, the onset of the spoof plasmon curve is delayed by approximately 6.7 ps with every 2 mm increase in $D$ as expected for low frequency spoof plasmon propagating close to speed of light. Thus from Figs. 5.3 and 5.4, we can see that the spectrogram is capable of accurately reproducing features that are expected of the SPS and the scattering edge coupling method.

The efficiency of the scattering edge coupling scheme is undeniably low since much of the light from the THz-TDS is blocked by the razor blades. Also, as noted by Saxler *et al.* [172], it is hard, if not impossible, to know *a priori* the actual efficiency of the coupling of the THz radiation to spoof plasmons since it depends on the frequency as well as the size of the coupling gap. Nevertheless, it is shown here that broadband

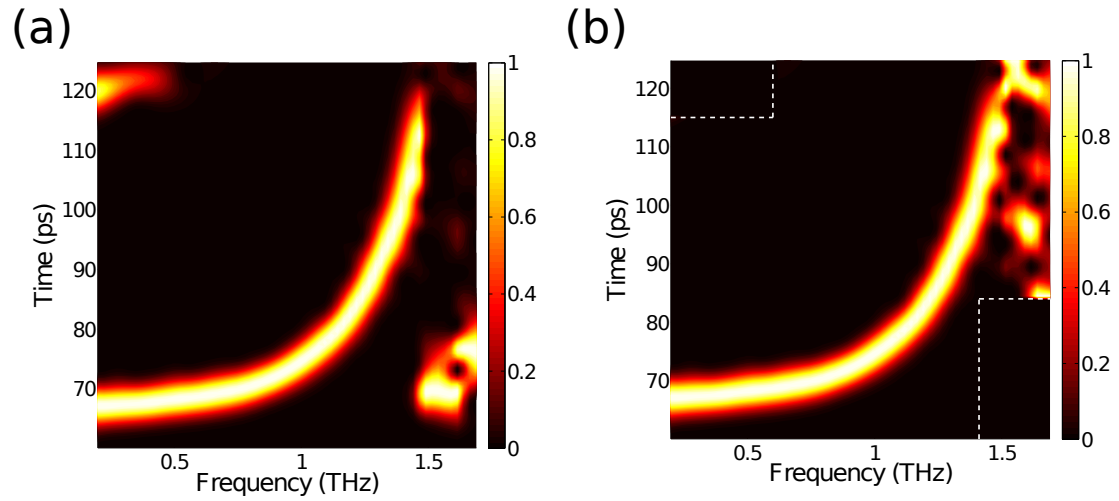



Figure 5.3: The effects of time-frequency filtering is illustrated here. Both spectrograms are for the $D = 8$ mm case. As can be seen, the time difference between the onset of the spoof plasmon curve and the secondary reflections is approximately 53 ps which is the time it takes for the low frequency spoof plasmons to make a round trip between the razor blades at speed of $c_0$. Time-frequency filters were applied in the region of $f \leq 0.6$ THz and $t \geq 115$ ps to filter out the secondary reflections. The peaks at the bottom right corner are due to light not coupled into spoof plasmons near the SPS cutoff frequency, $f_{SPS}$. Time-frequency filters were applied in the region of $f \geq 1.41$ THz and $t \leq 84$ ps to filter out the light not coupled to spoof plasmons near $f_{SPS}$.

information can indeed be obtained and the issue of efficiency can be circumvented by comparing relative changes in spoof plasmon characteristics instead of absolute values. Moreover, the scattering edge coupling scheme is chosen as it allows for the use of a sample with different geometrical parameters without the need for any change to the coupling scheme itself. It is noted, however, that coupling efficiencies could be drastically improved by adopting a microwave engineering approach where the impedance of the SPS is matched to that of an excitation transmission line and would be an important improvement in the future development of practical spoof plasmon sensors [134, 135]. Unfortunately, this is out of the scope of this thesis and can only be developed in future work.

It will also not escape notice that the spoof plasmon curves in the spectrograms shown in Fig. 5.4 all have a time width of $\Delta t$, which is the FWHM of the window

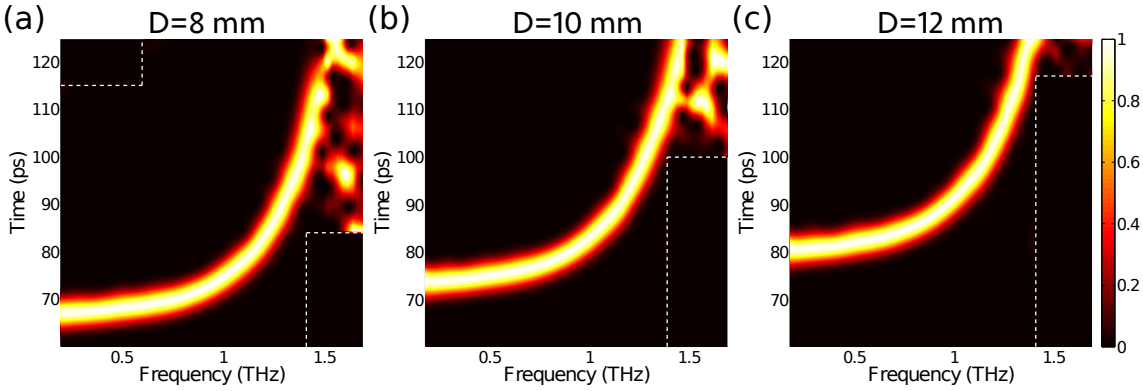



Figure 5.4: Spectrograms of the SPS with (a) $D = 8$ mm, (b) $D = 10$ mm and (c) $D = 12$ mm.

function $w(t)$, as well as a spectral width given by the bandwidth theorem to be $\sim 1/\Delta t$, as a result of the application of the sliding time window. Fortunately, the SPS used here only supports one mode as evidenced by the calculated bandstructure in Fig. 5.1(c). If more than one bound mode were supported on the SPS, the time-frequency width of the STFT would have imposed a finite resolution at which closely spaced modes can be differentiated from each other.

## 5.4 EXTRACTING SPOOF PLASMON DISPERSION RELATIONS

Each of the spectrograms shown in Section 5.3 was obtained in a *single measurement* and yield information about the group velocities of the spoof plasmon over a broad frequency range of 0.2 THz to almost 1.5 THz. This information can then be used to extract the dispersion relation via the method outlined below.

Let us first consider two adjacent frequency components of the spoof plasmon pulse $f_{n-1}$ and $f_n$ where $f_{n-1} < f_n$, as shown in Fig. 5.5. $f_{n-1}$ and $f_n$ propagates on the SPS with group velocities $v_{n-1}$ and $v_n$, respectively, from point A to point B. The separation between A and B is the distance $D$.

The times taken by the frequency components $f_{n-1}$ and $f_n$ to traverse $D$ are $\tau_{n-1} = D/v_{n-1}$ and $\tau_n = D/v_n$, respectively. This means that the difference in time taken

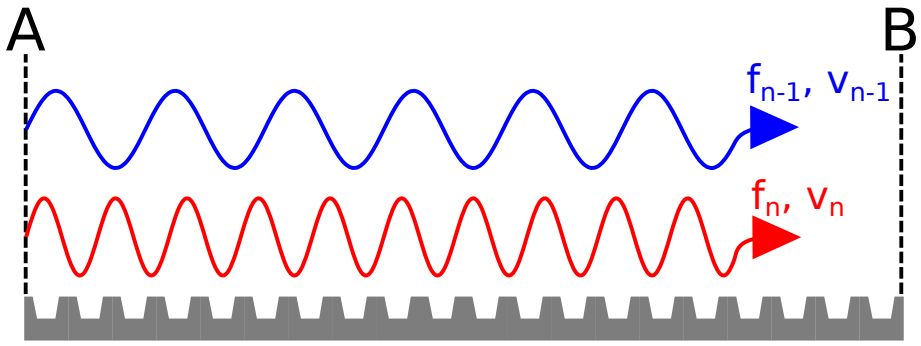



Figure 5.5: Schematic description of dispersion extraction. Here we consider two adjacent spoof plasmon frequency components with frequencies $f_{n-1}$ and $f_n$ travelling with group velocities $v_{n-1}$ and $v_n$, respectively, on the SPS.

is given by

$$\begin{aligned}\Delta\tau_{n,n-1} &= \tau_n - \tau_{n-1} \\ &= \frac{D(v_{n-1} - v_n)}{v_{n-1}v_n},\end{aligned} \tag{5.3}$$

where it is assumed that $v_{n-1} \geq v_n$, which is valid given that the lower frequency components propagate faster for our SPS.

After a slight re-arrangement of the terms, we arrive at

$$v_n = \frac{v_{n-1}D}{\Delta\tau_{n,n-1}v_{n-1} + D}, \tag{5.4}$$

where we have expressed the group velocity of the higher frequency component $f_n$ in terms of that of the lower frequency $f_{n-1}$.

We can then equate Eq. (5.4) to the definition of group velocity

$$\begin{aligned}v_n &= \frac{\partial\omega_n}{\partial k'^{\,n}_{//}} \\ &\approx \lim_{\Delta k'^{\,n}_{//}\to 0} \frac{\Delta\omega_n}{\Delta k'^{\,n}_{//}},\end{aligned} \tag{5.5}$$

where $\omega_n = 2\pi f_n$ and $k'^{\,n}_{//}$ is the real part of the wavevector parallel to the SPS (or the propagation constant) of the spoof plasmon of $f_n$. $\Delta k'^{\,n}_{//}$ is thus defined as $k'^{\,n}_{//} - k'^{\,n-1}_{//}$. Note that since we will be dealing with losses explicitly later on in this

chapter, the complex wavevector of the spoof plasmon parallel to the SPS is defined to be $k_{//} = k'_{//} + i\bar{\alpha}_F/2$ where $\bar{\alpha}_F$ is the power attenuation coefficient of the spoof plasmons.

Equation (5.5) results in

$$\Delta k'^{\,n}_{//} = \Delta\omega_n \left( \frac{\Delta\tau_{n,n-1} v_{n-1} + D}{v_{n-1} D} \right), \tag{5.6}$$

for $n = 1, 2, 3...$, where $\Delta\omega_n = \omega_n - \omega_{n-1}$.

The actual propagation constant of the spoof plasmon spectral component $f_n$ is then given by Equation 5.7

$$k'^{\,n}_{//} = k'^{\,n-1}_{//} + \Delta k'^{\,n}_{//}, \tag{5.7}$$

where $k'^{\,n-1}_{//}$ is the propagation constant of the previous frequency component, $f_{n-1}$.

The lowest frequency maxima at each time point of a spectrogram such as Fig. 5.2(c) can then be picked out, giving a series of time-frequency coordinates $(\tau_i, f_i)$ that can be inputted into the above method to solve for the dispersion relation iteratively. The lowest frequency peak at each time point is related to the spoof plasmon because, as we saw in Fig. 5.1(c), only one bound mode is supported in our frequency range of interest. If more than one bound mode exists, the procedure of picking out the modes belonging to the spoof plasmons would be more complicated. At this point, we are still missing a crucial ingredient: the starting point $k'^{\,0}_{//}$ and $v_0$ for $f_0$.

The starting point is decided by looking at a sufficiently low frequency component $f_0$, such that the group velocity is linear in the vicinity of $f_0$ (see bandstructure in Fig. 4.3(c)). The propagation constant is thus simply given by $k'^{\,0}_{//} = \omega_0/v_0$, where $v_0$ is the initial group velocity of $f_0$.

The initial group velocity $v_0$ is then calculated by comparing the time $\tau_0$, taken by a low frequency spoof plasmon with $f_0$ to travel the distance $D$ on the SPS, to the same time taken on a flat metal surface $\tau_{PEC}$. The group velocity $v_0$, is then given

by

$$v_0 = c_0 - \frac{D(\tau_0 - \tau_{PEC})}{\tau_0 \tau_{PEC}}, \tag{5.8}$$

where $c_0$ is the speed of light in vacuum and $\tau_0$ is simply the time coordinate of $f_0$ obtained from the spectrogram. The $v_0$ values calculated using Eq. (5.8) as well as by looking at the time taken by a low frequency spoof plasmon to travel a given distance in Fig. 5.4 both give $v_0 = 2.95 \times 10^8$ ms$^{-1}$ thus showing that Eq. (5.8) gives an accurate value for the initial group velocity.

The blue crosses in Fig. 5.6 shows the spoof plasmon dispersion extracted via the above-mentioned procedure and is in excellent agreement with the calculated dispersion (red-solid line, extracted from the peaks of Fig. 5.1(c)). As can be seen, the extracted dispersion gives information about the spoof plasmon characteristics from 0.4 THz to 1.44 THz. The dispersion relation could not be extracted all the way to the Brillouin zone edge ($k'_{//} = \pi/P = 5.24 \times 10^4$ m$^{-1}$) because as the theoretical SPS cutoff frequency $f_{SPS} = 1.54$ THz is approached, the signal-to-noise ratio deteriorates rapidly due to a lower coupling efficiency from free space radiation to spoof plasmons.

Using Eq. (2.50), we find that the spoof plasmon can be confined to a region as small as 43 $\mu$m normal to the SPS, representing a field confinement of the order of $\lambda_0/5$. This implies that light-matter interactions are drastically enhanced in the vicinity of the SPS surface. Meanwhile, at low frequencies, such as 0.5 THz, it can be seen that the dispersion is very close to the light line (Fig. 5.6, black-dashed line), indicating poorly confined fields. Of course, this is entirely down to the design of the SPS corrugations. One of the main advantage of using the spoof plasmon approach is that the optical response can be tuned via a change of corrugation design or geometrical parameters. One can imagine a SPS with novel properties such as to have high field confinement in more than one frequency regime as demonstrated by Williams *et al.* by using annular holes as the unit cell [128] or design an SPS with

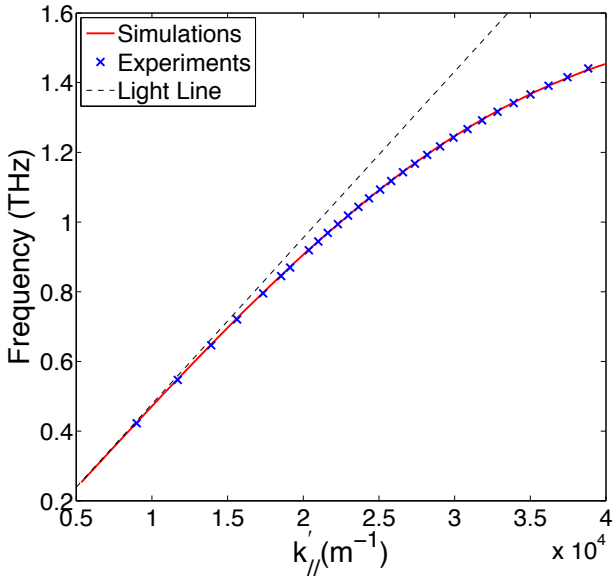



Figure 5.6: Simulated (red solid line) and experimentally extracted (blue crosses) SPS dispersion relation. The light line is given by the black-dashed line.

a spoof plasmon relation that deviates from strongly the light line over a narrower band of frequencies by using grooves with less slanted walls (see Fig. 4.4).

## 5.5 BROADBAND REFRACTIVE INDEX SENSING

So far, we have established that the scattering edge coupling method, together with STFT analysis, allows us to extract broadband information about the spoof plasmons. In this section, the enhanced light-matter interaction, expected to occur in the vicinity of the SPS, will be utilised to conduct broadband refractive index sensing. The SPS grooves are filled with various fluids, namely air ($n = 1$, control), diesel ($n \sim 1.45$), liquid paraffin ($n \sim 1.47$), olive oil ($n \sim 1.51$) and glycerin ($n \sim 1.85$), and changes in the spoof plasmon dispersion relation as well as attenuation are monitored. This gives information on both the *real* and *imaginary* parts of the refractive indices of the fluids and points to the SPS's potential to fully characterise fluids. It is noted here that the fluids used have a smoothly varying refractive index profile without any sharp spectral features (see Fig. 5.7).

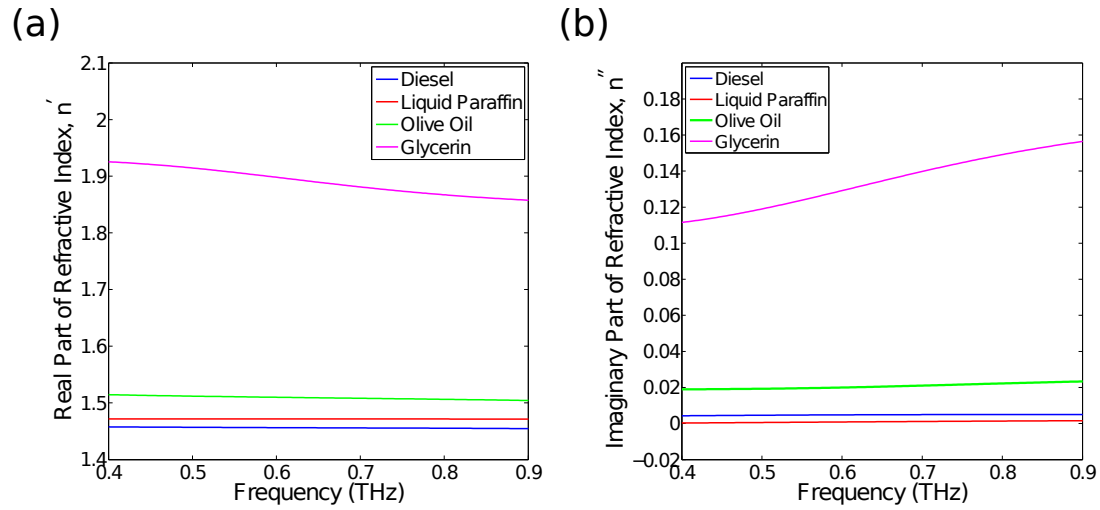



Figure 5.7: The real (a) and imaginary (b) parts of the refractive indices of diesel (blue), liquid paraffin (red), olive oil (green) and glycerin (magenta) are shown here from 0.4 THz to 0.9 THz.

The SPS grooves are filled by first covering the entire SPS with the above fluids. Any excess fluid is then gently removed using a thin plastic sheet. Care is taken to remove any fluid on the SPS that is not in the groove. The SPS is rinsed with toluene and distilled water, and a reference measurement is taken between each fluid measurement to ensure that the SPS is clean and there is no change in the optical properties of the SPS.

Figure 5.8(a) shows how the spoof plasmon dispersion relation is red-shifted as the real part of the refractive index of the fluids filling the grooves is increased. For example, at $k_{//}/k_0 = 1.25$, the spoof plasmon frequencies for air, diesel, liquid paraffin, olive oil and glycerin are 1.4 THz, 1.19 THz, 1.16 THz, 1.14 THz and 0.99 THz, respectively. This is attributed to an increase in the effective refractive index of the SPS due to the presence of the fluids. The dispersion relation of the spoof plasmons when the SPS grooves are filled with various fluids, simulated with measured bulk fluid dielectric constants, are shown in Fig. 5.8(b). The experiments are in good agreement with the simulation results. The fluid refractive indices

used in the simulations are extracted from transmission THz-TDS measurements via the method described by Duvillaret et al [155] using a Matlab code written by Dr. Stephen Hanham. The x-axes in Fig. 5.8 are normalised to $k_0$, meaning that the light line now corresponds to a vertical line at $k'_{//}/k_0 = 1$. The reason behind this normalisation is because the real part of the refractive indices of diesel, liquid paraffin and olive oil are very similar and the dispersion relations would overlap if plotted in the conventional units of $\mathrm{m}^{-1}$. Thus the normalisation to $k_0$ acts to accentuate the differences between the dispersion curves and facilitate comparison between simulation and experiment.

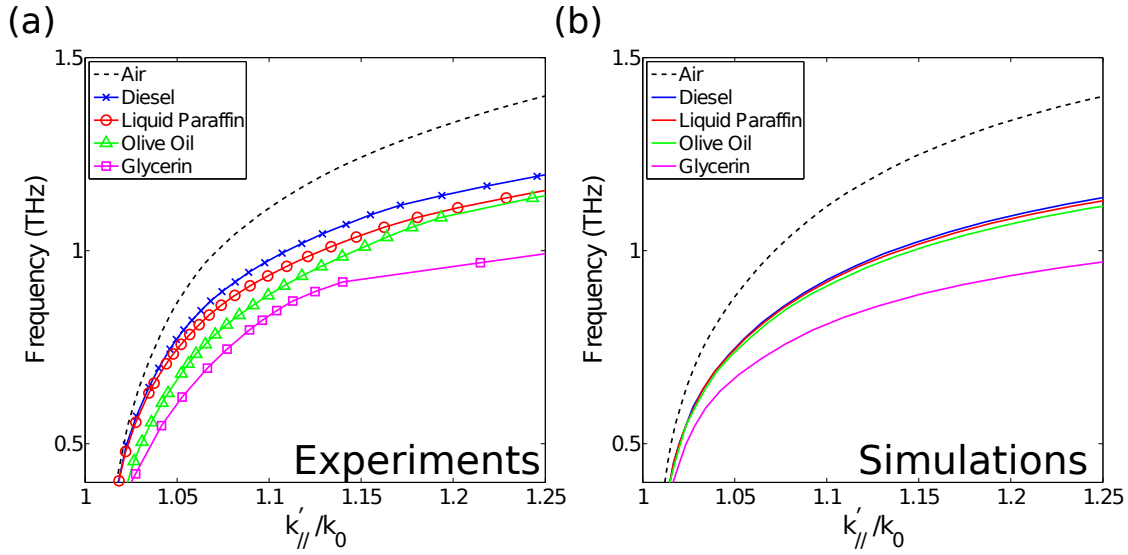



Figure 5.8: Dispersion of the SPS obtained from (a) experiments and (b) simulations when its grooves are filled with various fluids. The x-axis is normalised to the free-space wavevector $k_0$, to facilitate comparison of experimental and simulation results.

Similar to Fig. 5.6, the dispersion relations could not be extracted all the way to the Brillouin zone edge due to a deterioration in signal-to-noise ratios as the $f_{SPS}$ for the individual fluids are approached in each case. This problem is aggravated when we recall that the fluids are not lossless and the absorption of electromagnetic energy by the fluids will result in further degradation of the signal strength.

While changes in the broadband dispersion allows us to detect changes in the re-

fractive index of the fluid filling the grooves, we would ideally like to be able to fully characterise the dielectric properties of the analytes in the grooves by accessing information about the imaginary part of the refractive indices or losses. This can be obtained by comparing the amplitude of the spoof plasmon arriving at the second razor blade over two separate $D$ values, namely $D = 8$ mm and $D = 12$ mm. Straightforwardly, the power attenuation coefficient of the spoof plasmons can be written as

$$\alpha_F^{SPS} = -\frac{1}{\Delta D} \ln \left( \frac{|A(\omega)_{D=12\ \mathrm{mm}}|^2}{|A(\omega)_{D=8\ \mathrm{mm}}|^2} \right), \tag{5.9}$$

where the subscript $F$ denotes the fluid in the groove, $\Delta D$ is the difference in the two $D$ values (4 mm in this case) and $A(\omega)$ is the amplitude of the spoof plasmon peak in the unnormalised spectrogram $\bar{S}$, at $\omega$. $\alpha_F^{SPS}$ represents the attenuation of the spoof plasmon caused by the fluids and the SPS itself. Losses from the SPS (i.e. the intrinsic SPS attenuation) are caused predominantly by increased scattering from spoof plasmons to free space radiation due to surface imperfections as well as ohmic losses. A further discussion on the intrinsic SPS loss will be presented later in this section.

In order to isolate the influence of fluid absorption on the spoof plasmon, the intrinsic SPS attenuation with air filling the grooves $\alpha_{Air}^{SPS}$, is subtracted from the attenuation coefficients of the other fluids to give the propagation loss due to the fluids

$$\bar{\alpha}_F = \alpha_F^{SPS} - \alpha_{Air}^{SPS}, \tag{5.10}$$

where the subscript $F$ now represents the fluids with the exception of air. This experimentally accessible magnitude gives us a quantitative measure of the absorptive character of the target fluids. The spoof plasmon attenuation with air as the dielectric, $\alpha_{Air}^{SPS}$, is around 0.5 cm$^{-1}$ from 0.4 THz to 0.9 THz.

Figure 5.9(a) shows $\bar{\alpha}_F$ plotted over a frequency range of 0.4 THz to 0.9 THz. Comparing Fig. 5.9(a) to the imaginary parts of the refractive indices of the fluids, $n''$ shown in Fig. 5.7(b), we can see that $\bar{\alpha}_F$ follows a similar trend to the actual

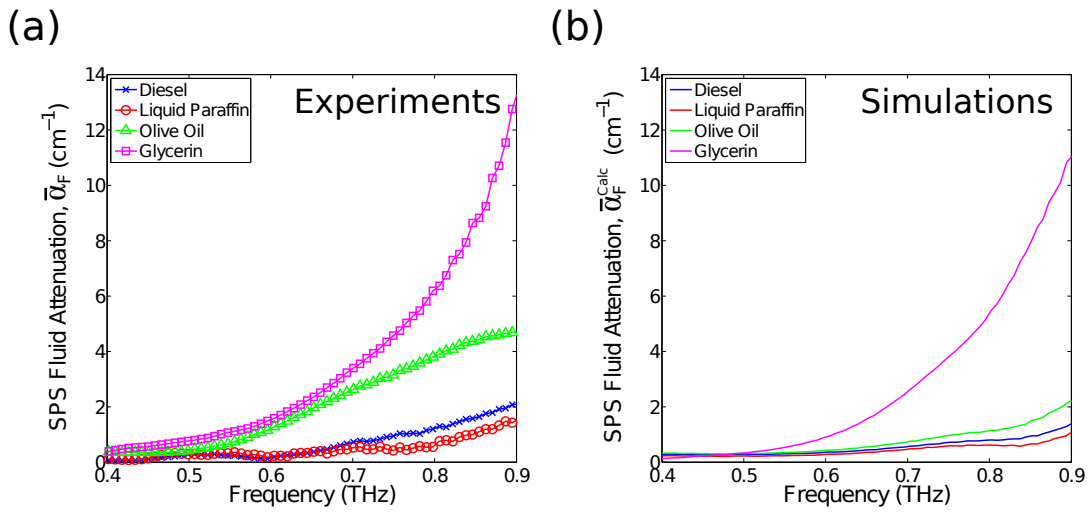



Figure 5.9: Attenuation coefficients of the spoof plasmon due to fluids obtained from (a) experiment, $\bar{\alpha}_F$ and (b) simulation, $\bar{\alpha}_F^{Calc}$.

fluid parameters, with glycerin having the highest loss, followed by olive oil, diesel and liquid paraffin. At 0.4 THz, when the fields are poorly confined, it can be seen that $\bar{\alpha}_F$ of the various fluids are very close to each other since the fields will not be sensitive to perturbations in refractive index of the SPS groove. On the other end of the spectrum at 0.9 THz, however, a marked difference is observed in $\bar{\alpha}_F$ values due to the stronger field confinement at higher frequencies. Most notably, even in the cases of liquid paraffin and diesel, which have very close $n''$ values (see Fig. 5.7(b)), there is an apparent difference in $\bar{\alpha}_F$.

Moreover, if we look back to Fig. 5.8, we can see that the dispersion relations of diesel, liquid paraffin and olive are actually very similar to each other. However, when we look at the losses they induce on the spoof plasmons, we can easily tell the difference between the three fluids. The ability to obtain loss information thus provides us with an additional avenue via which analytes can be studied and differentiated from one another.

To show that the experimental results are in line with theoretical predictions, a spoof plasmon pulse is simulated on a 2D version of our SPS via a TM polarised dipole

source with a frequency range of 0.1 THz to 2 THz in Lumerical FDTD Solutions. Time-domain data is collected in the simulation via two point monitors at a distance of 8 mm and 12 mm from the dipole source and processed in the same way as the experimental data for the various fluids. Again, the fluid refractive indices used were the ones experimentally obtained as shown in Fig. 5.7. Figure 5.9(b) shows the calculated power attenuation coefficient of the spoof plasmons $\bar{\alpha}_F^{Calc}$. As can be seen, the simulated spectra corroborates the experimental results, with higher field confinements (at higher frequencies) leading to greater sensitivity to the fluids.

At this point, a comment on the procedure of subtracting $\alpha_{Air}^{SPS}$ from the fluid attenuation is pertinent. It is noted that the intrinsic SPS attenuation is not in general constant and metallic losses increase as the confinement of the spoof plasmon increases [134]. This is because as the field confinement increases the current density within the metal necessarily increases; hence there will be greater metallic losses in the case where there is high field confinement, even though metallic losses at low frequencies are often considered negligible due to a diminishing skin depth. However, it is found from complex eigenfrequency calculations that increases in intrinsic SPS losses as the SPS grooves are filled with lossless dielectrics with $n = 1$ to 2 are small compared to $\bar{\alpha}_F$ within the frequency range considered here. For example, even in the case of glycerin with $n \sim 1.8$ (which has the highest refractive index and the strongest spoof plasmon confinement among the results presented here) the increase in metallic losses contributes to less than 5% of the extracted spoof plasmon attenuation at 0.9 THz (the maximum frequency considered). Note that this is the most extreme case considered in our experiments. For the other fluids this increase in intrinsic loss even less. Not to mention, at lower frequencies where there is less field confinement, this increase in intrinsic loss would also be smaller. This is why $\bar{\alpha}_F$ is attributed mainly to fluid loess. Nevertheless, it must be borne in mind that metallic losses can become a non-negligible factor in special scenarios such as when there is very high field confinement or when the fluid has a very high real part of

the refractive index and very low loss.

The comparison of $\bar{\alpha}_F$ across all the fluids is done from 0.4 THz to 0.9 THz because the SPS response of glycerin cuts off at approximately 1 THz as shown in Fig. 5.8(a) and the data becomes very noisy near $f_{SPS}$. However it is noted that broadband data (a bandwidth of 0.5 THz) is obtained here using only two measurements per fluids. This not only minimises sample handling processes but is also advantageous when compared to resonant sensing methods when it comes to identifying substances via spectroscopic features. Additionally, the interaction volume of the fluid and the spoof plasmon is estimated to be of the order of microlitres. For example, in the case of $D = 8$ mm, there are 133 grooves between the razor blades, corresponding to an interaction volume of just 600 nL given that the THz beam diameter is approximately 5 mm. This is far lower than the volume required for traditional THz spectroscopy methods (such as transmission spectroscopy used to extract the bulk dielectric constants in Fig. 5.7) which is of the order of millilitres. The mentioned interaction volume is by no means the best. It can surely be reduced by tailoring the SPS to specific sensing applications. One can also see how the SPS can be integrated with microfluidics to perform high sensitivity broadband refractive index sensing in a lab-on-chip type of environment; where the analytes can be delivered to the SPS via microfluidic channels for *non-destructive* THz characterisation then sent for further analyses by other methods.

Though out of the scope of this thesis, it is conceivable to use the SPS data obtained to retrieve the broadband refractive index of the fluids using the coupled mode method [143] since the dispersion and attenuation coefficients are related to the complex refractive indices of the fluids filling the grooves. However, such parameter retrieval is non-trivial since the SPS parameters are not simply related to the real or imaginary parts of the refractive index and the electromagnetic field modes are not easily defined for our SPS grooves which have slanted walls. For instance, the

propagation constant generally depends on *both* the real and imaginary parts of the refractive index of the fluid, and to understand how the fields interact with the sensed samples we would need to be able to consider all the electromagnetic modes existing in the metallic corrugations. The calculations very quickly become involved as more diffraction orders and waveguide modes need to be taken into account (see Section 2.5). A more practical approach might be to use simulation methods to pre-calculate the $k_{//}$ for a range of complex refractive index values. In this way, experimentally obtained $k_{//}$ can then be conveniently related back to a given refractive index within the pre-calculated set.

## 5.6 THz surface-enhanced absorption spectroscopy

The ability to extract broadband data also means that sharp spectral features in a material's dielectric properties can be identified. As a final demonstration of broadband spoof plasmon sensing, THz surface-enhanced absorption spectroscopy via spoof plasmons is presented in this section. Here, the enhanced field confinement on the SPS is used to identify substances with spectral features such as absorption peaks. In this way, we can truly answer the question of *"what is present?"*, since a spectral fingerprint will allow us to uniquely identify a substance.

In particular, $\alpha$-lactose monohydrate with absorption peaks at 0.53 THz and 1.37 THz, as shown in Fig. 5.10, was used as the analyte because its absorption peaks lie nicely within the operating frequency range of our SPS. The absorption spectrum of $\alpha$-lactose monohydrate was obtained via THz transmission measurements of the lactose powder loosely packed in a 1 mm thick sample cell. The positions of the absorption peaks matches exactly those reported in previous literature [22, 173]. Note that the y-axis is quoted in arbitrary units as the absolute magnitude of the peaks depends strongly on factors such as how tightly the powder is packed and the thickness of the sample cell.

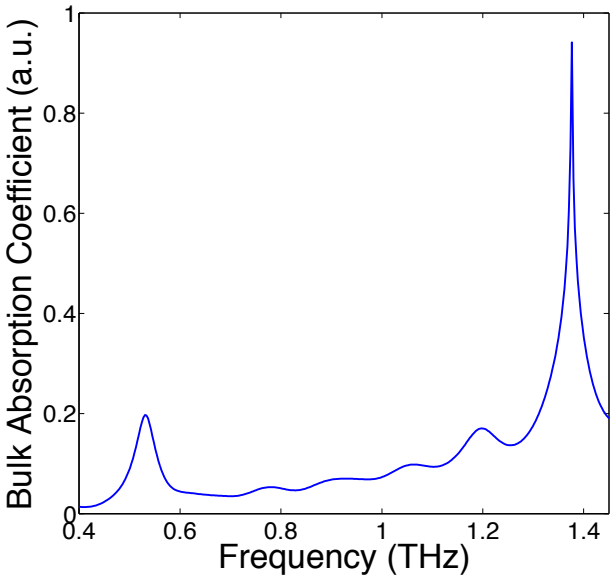



Figure 5.10: Absorption spectrum of $\alpha$-lactose monohydrate.

A thin layer of $\alpha$-lactose monohydrate powder is deposited on the SPS by uniformly dispersing the powder via compressed air in a chamber and allowing it to settle on the SPS over 5 mins. The surface mass density of the lactose powder was estimated to be $(300 \pm 5\%)$ ng/mm$^2$ by weighing the sample before and after the deposition.

For this set of measurements, $D$ was kept constant at 10 mm and care was taken to make sure that any secondary reflections between the razor blades were not recorded in the raw time-domain signal. The Fourier transform spectrum of the SPS time-domain signal with the lactose powder was normalised to that without the lactose powder to give the power transmission across the SPS over a distance of 10 mm, $T^{SPS}$. An extinction coefficient $\Gamma$, is then defined as

$$\Gamma = -\ln(T^{SPS})/D, \tag{5.11}$$

where $\Gamma$ tells us how much energy from the spoof plasmons is lost due to the presence of the lactose powder on the SPS.

The reason why a simple Fourier transform was used instead of the STFT is because

STFT tends to smear out sharp changes in the amplitude due to the application of the time window $w(t)$. Moreover, while it is easy to pick out the peaks in the spectrogram (see Section 5.4), it is not a simple task in *picking out* dips in amplitude resulting from increased absorption of spoof plasmon energy due to analyte absorption peaks. An examination of the unfiltered normalised spectrogram of lactose powder deposited on the SPS, shown in Fig. 5.11 will show that most of the energy around 1.37 THz (demarcated by the white-dashed line) is coupled into spoof plasmons. Thus any spectral features observed in the Fourier transform can only be attributed to the spoof plasmons.

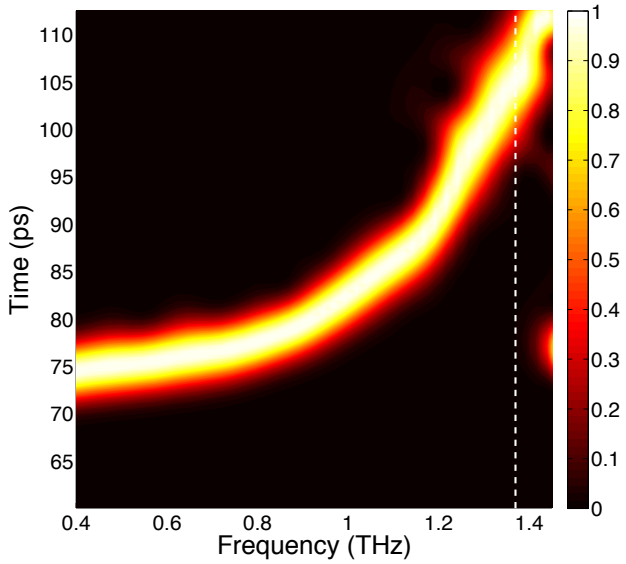



Figure 5.11: Normalised spectrogram of $\alpha$-lactose monohydrate powder on the SPS. The white-dashed line demarcates 1.37 THz where $\alpha$-lactose monohydrate has an absorption peak.

The blue-solid line in Fig. 5.12 shows the $\Gamma$ spectrum of the case of $\alpha$-lactose monohydrate deposited on SPS. The black-dashed line shows the absorption peak of the lactose powder at 1.37 THz. As can be seen, there is a sharp peak in $\Gamma$ at 1.36 THz which is attributed to an increase in the absorption of spoof plasmon due to the presence of the lactose powder, given the 16 GHz frequency resolution of the THz-TDS. A higher spectral resolution would of course be preferable, however, we are limited

by the length of the time pulse that could be recorded (recall from Section 2.6.3 that the frequency resolution is given by $1/2NT$). A measurement method with higher spectral resolution such as frequency-domain THz spectrometry [44, 45] could also be used to improve upon this. The lower frequency absorption peak of the $\alpha$-lactose monohydrate powder was not observed due to the lack of field confinement at the lower frequency regimes for the SPS used here.

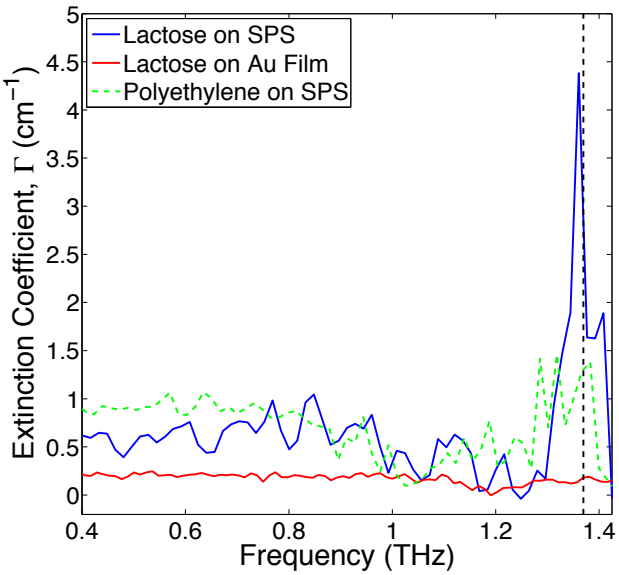



Figure 5.12: $\Gamma$ spectra for $\alpha$-lactose monohydrate deposited on SPS (blue-solid line) and Au film (green-dashed line), and polyethylene powder deposited on SPS (red-solid line).

To further justify the claim that the observed peak in $\Gamma$ is indeed due to an enhanced interaction between the lactose powder and the tightly confined fields, two other cases are explored. First, $\alpha$-lactose monohydrate powder was deposited on a flat gold film to see what happens when the fields are no longer tightly confined. Second, polyethylene powder was deposited on the SPS to see the effect on $\Gamma$ if the analyte had no absorption peak. In both cases, similar surface mass densities of lactose and polyethylene powders were deposited to ensure that comparisons were reliable.

The $\Gamma$ spectrum for the $\alpha$-lactose deposited on a flat gold film case is featureless as shown by the red line in Fig. 5.12. This is because the fields on the gold film

are very poorly confined as only Sommerfeld-Zenneck waves propagate on it (see Section 2.4). Thus the fields interact only very weakly with the lactose. For the case where polyethylene powder was deposited on the SPS (Fig. 5.12, green-dashed line) it can also be seen that the $\Gamma$ spectrum is featureless despite the confined fields of the spoof plasmons as the analyte present now has no absorption peaks.

Another thing to note is that the baseline value for $\Gamma$ is higher in both of the SPS cases ($\Gamma \sim 0.5 - 1$ cm$^{-1}$) as compared to the flat gold film case ($\Gamma \sim 0.2$ cm$^{-1}$). This is because the tightly confined fields on the SPS are more sensitive to surface perturbations than those on the gold film. The powder particles can act as scatters which out-couple spoof plasmons to free space radiation resulting in a larger baseline extinction coefficient. Additionally, the $\Gamma$ spectra is noisier for the SPS cases because of a lower signal-to-noise ratio compared to the gold film.

Nonetheless, by comparing the three cases and taking into account the observation of the $\Gamma$ peak only in the case of lactose deposited on the SPS, it can be concluded that the $\Gamma$ peak is indeed due to an increased interaction between the lactose and the spoof plasmon fields. More importantly, it shows that the spoof plasmon sensing method proposed here is capable of detecting spectral signatures that lie within its operating frequency range where there is strong field confinement, enabling us to take a more spectroscopic approach to THz sensing.

## 5.7 SPOOF PLASMON SENSING: ARE WE THERE YET?

In this chapter, spoof plasmon sensing is expanded from the narrowband operation presented in Chapter 4 to broadband sensing. It is shown that the scattering edge coupling method, together with STFT analysis, is capable of yielding broadband information, allowing for the extraction of spoof plasmon dispersion from 0.4 THz to 1.44 THz in a *single measurement*. Broadband refractive index sensing is then shown via monitoring changes in the dispersion relations and attenuation coeffi-

cients of the spoof plasmons. The attenuation coefficients can be obtained with a minimum of two measurements and gives access to information about fluid losses. This means that spoof plasmon sensors can potentially be used to fully characterise substances. Most notably, the volume of the analytes needed is of the order of microlitres, far less then traditionally required. Finally, it is shown that the SPS is capable of detecting substances with spectral features such as absorption peaks, thus opening spoof plasmon sensor up to applications in fingerprint identification of unknown substances, much like how traditional transmission spectroscopy is used in gas sensing [21].

The tightly confined fields of the spoof plasmons is shown to increase light matter interactions thus helping to circumvent issues in THz sensing such as the lack of source power and field confinement, as mentioned in Chapter 1. The potential of integrating spoof plasmon sensors with microfluidics and surface functionalisation also means that such sensors can be placed in a lab-on-chip environment for multi-modal sensing applications. Going back to the most charming aspect of metamaterials, the ability to engineer the optical properties and the myriad of SPS geometries give engineers enormous flexibility to design solutions to sensing problems over a wide range of frequencies.

In this thesis, the potential for SPSs to conduct THz sensing was showcased by subjecting an SPS of a generic design to a wide range of sensing parameters and scenarios. However, there is no *one-size fits all* solution. Every sensor has to be tailored to a specific application. Thus the performance results presented here are by no means the pinnacle of SPS sensing. More work can be done to tailor each SPS to a particular sensing purpose. The question that now remains is, *"are we there yet?"*. What more can be done to push spoof plasmon sensing to actual real-world applications? Unfortunately, this is not a question that will be answered in this thesis. That being said, certain research directions that can be pursued to achieve

the practical spoof plasmon sensors will be outlined in the concluding chapter.

CHAPTER 6

# CONCLUSIONS & FUTURE WORK

Right from the outset of this thesis, the aim of the work presented was to see how far metamaterials, in particular spoof plasmons, can go in overcoming some of the challenges in THz sensing research. It is hoped that by taking the first steps in applying SPSs to actual sensing situations, the idea of spoof plasmon sensing could begin to gain traction and help propel metamaterial-based sensors one step closer to real-world applications where the benefits of THz characterisation can be brought out fully.

The first project undertaken in this PhD used lattice resonances in diffractively coupled metallic antennas as the sensing mechanism [151]. A sensing Figure-of-Merit of 3.80, the highest for THz metamaterial sensing at the time of publication, was achieved for the refractive index sensing of 50 $\mu$m thick fluid samples. More importantly, the conclusions of this project highlighted certain key factors in THz metamaterials sensing:

- Need for high field confinement.
- Simplicity of readout response.
- Potential for easy integration into lab-on-chip.

Recognising that SPSs can potentially address the above issues, ways in which spoof plasmon sensing can be conducted were investigated in Chapters 4 and 5. Narrow-band SPS sensing was first presented in Chapter 4 [167]. A Figure-of-Merit as high as 49 was achieved using phase jumps as a readout response, meaning that small

dielectric changes could be sensed using spoof plasmons. One can imagine how such narrowband spoof plasmon sensing method can be used in industries such as oil and gas where the fluids dealt with are generally low loss in the terahertz regime and needs to be differentiated from other high loss materials such as water.

This is then followed up by broadband spoof plasmon sensing work in Chapter 5. Broadband refractive index sensing, accessing information on both the real and imaginary parts of the fluid refractive index, was demonstrated on microlitre volumes of fluids. A proof-of-principle demonstration of THz surface-enhanced absorption was also shown using $\alpha$-lactose monohydrate powder deposited on the SPS. This shows that SPSs can potentially be used in the fingerprinting of substances; thus showing that spoof plasmons sensors are capable of addressing the main questions posed in sensing problems of *how much* and *what is* present (see Section 4.6).

On the whole, the tightly confined fields on the SPS lead to sensitivity to dielectric changes in its vicinity, allowing for sensing of small volumes of analytes while side-stepping problems such as the lack of powerful sources. In particular, it is shown that by using different coupling methods (Otto prism and scattering edge coupling), the rich information contained in a spoof plasmon pulse can be exploited for a variety of sensing applications.

Moreover, it is easy to see how SPSs can be coupled with microfluidics and surface functionalization for multi-modal sensing in a lab-on-chip environment. The grooves of the SPS could, for example, act as the microfluidic channels for sample delivery. The gold surface could be functionalized for efficient capture of specific analytes to increase the interactions between the spoof plasmon and the analyte. Lastly, it is noted that the performance metric values reported in this thesis are by no means the pinnacle of SPS performance. There is no *one-size fits all* solution to sensing; every sensor needs to be tailored to specific sensing applications. By fine-tuning the SPS parameters, coupling mechanism and operation frequency, much better

sensing performance could be achieved. What is demonstrated in this thesis is the possibility of using metamaterials creatively to address real-world sensing problems, which is in no way remote considering the results presented here. Moving on from this thesis, there are four areas of further development that would be interesting for spoof plasmon sensing.

Firstly, work can be done to compare spoof plasmon sensing with traditional characterisation methods such as THz absorption spectroscopy. Thus far, THz sensing/spectroscopy experiments have been targeted at particular substances such as lactose or water using conventional methods such as transmission spectroscopy. Comparatively, work done on THz *metamaterial* sensing have been focussed on detecting refractive index changes caused by using different materials to come into contact with the metamaterial sensor. This is because THz metamaterial sensing is only in the initial phases of development and experiments are conducted in a very controlled manner where the figure-of-merit is determined in terms of refractive index change. If THz metamaterial sensing were to progress further towards real-world applications, it would need to prove its worth against established methods under practical scenarios. A systematic study of the sensing performance of THz metamaterial approaches needs to be conducted by using substances already characterised by traditional THz spectroscopy to see which performs better. This would be a first step towards establishing THz metamaterial sensing. For example, in the field of gas sensing, one could perhaps ask what is the concentration of a particular gas, say dichloromethane, that metamaterial sensors can detect compared to traditional gas sensors? The key here is to close the gap in knowledge on the detection limits and sensitivity of metamaterial sensors in terms *real-world units*, such as parts per million or percentage volume, instead of simple refractive index change.

Another area in which additional research can be carried out is the efficient excita-

tion of spoof plasmons. This is motivated by the work in Chapter 5 which revealed that the scattering edge coupling method, while flexible, is quite inefficient and results in much of the THz radiation being *thrown away* at the razor blades. Figure 6.1 presents two possible methods via which the spoof plasmon efficiency can be improved. The concept shown in Fig. 6.1(a) is inspired by approaches taken in microwave engineering [135]. It is essentially a tapered waveguide which provides impedance matching from the source in free space to the SPS. A second method of efficiently coupling to spoof plasmons would be to integrate a dipole source, such as a photoconductive antenna, in the near field of the SPS, as shown in Fig. 6.1(b). In this way, all the radiation from the source would be available to interact with the SPS while at the same time the THz radiation would have the momentum characteristics to couple into spoof plasmons since the photoconductive antenna is essentially a point source.

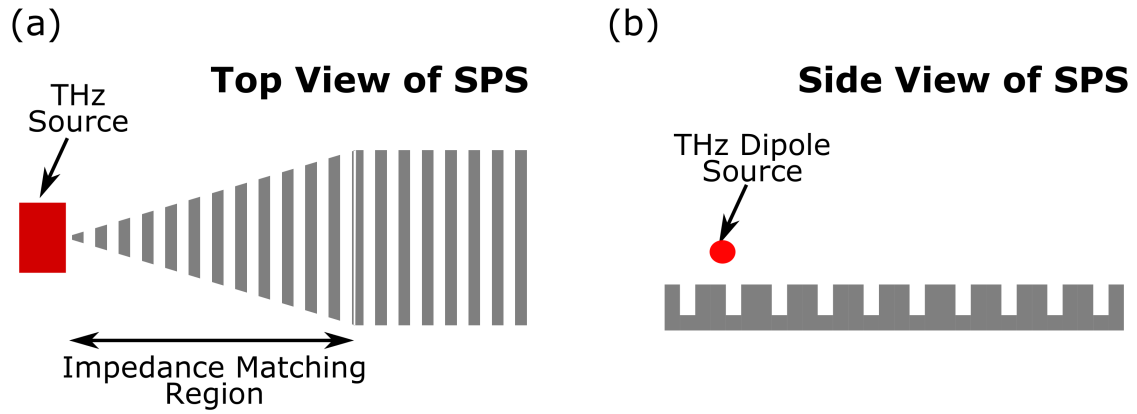



Figure 6.1: Alternative spoof plasmon excitation methods. (a) A tapered waveguide could be use to provide better impedance matching between a THz source and the SPS. (b) A THz dipole source, such as photoconductive antennas, could be incorporated into the THz SPS sensor to better excite the spoof plasmons.

The third research direction would be to incorporate microfluidic channels onto the SPS sensor as shown in Fig. 6.2. The grooves of the SPS could act as the microfluidic channels for analyte delivery with reservoirs on either side of the SPS. Analytes such as cancer cells or gases can then be flowed through the channels and detected using

the tightly confined spoof plasmon fields. This would be a necessary development when it comes to integrating SPS sensors on to lab-on-chip devices.

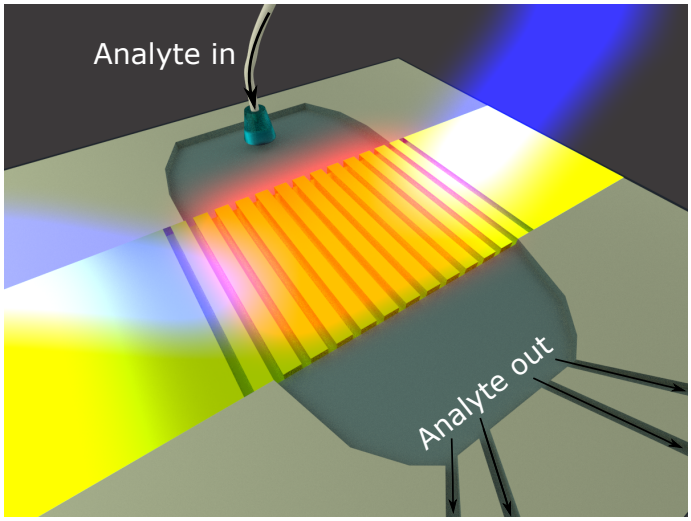



Figure 6.2: Concept drawing of SPS sensor incorporated with microfluidic channels.

Lastly, novel methods of extracting data from spoof plasmons can be explored. One particularly interesting idea is the spoof plasmon interferometer proposed by Xu and Mazumder [174]. Figure 6.3 shows a schematic diagram of such an interferometer. Spoof plasmons entering the interferometer will be split into two arms. One is the reference arm (see Fig. 6.3, blue box), the other is the sample arm (see Fig. 6.3, red box). The reference and sample analytes can be delivered via microfluidic channels to the respective arms. Spoof plasmons, after propagating through both SPS arms will interfere at the output end and detected. Such a measurement method will allow for more flexibility in taking data as well as allow for different sample analytes to be simultaneously compared to each other. One could even measure temporal changes since the spoof plasmons will take different amounts of time to travel through the reference and sample arms. Of course, this is only a suggestion of a new method of measuring spoof plasmon sensing data, there is no doubt that many more ways could be found via the creative use of metamaterials and spoof plasmon surfaces.

The above proposed directions of research will explore applications of spoof plasmon

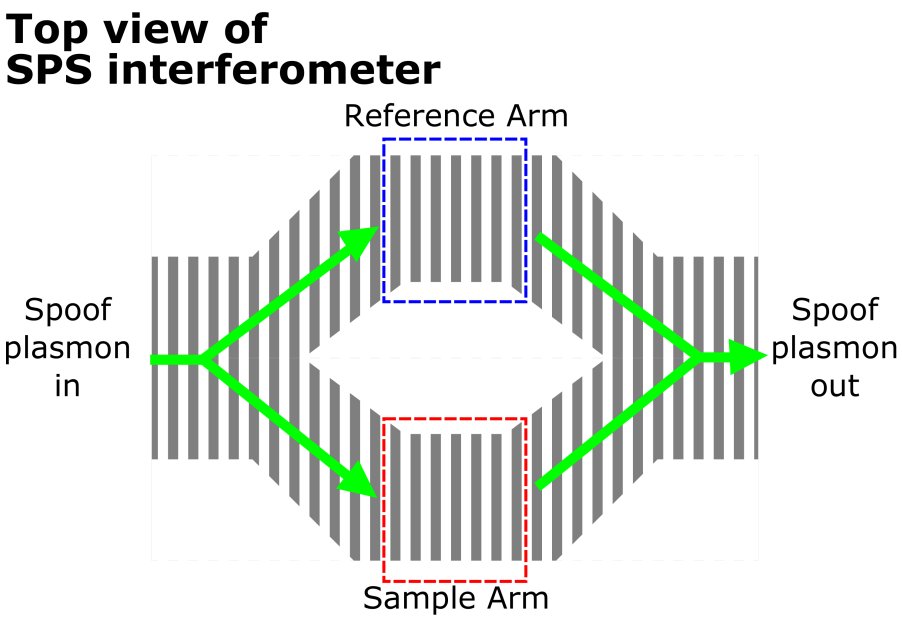



Figure 6.3: Schematic of SPS interferometer. The top arm indicated by the blue box is the reference arm while the bottom arm indicated by the red box is the sample arm.

sensors in actual biochemical-analysis scenarios, establish whether spoof plasmons can outperform established methodologies and find new ways of making even better use of the information held by spoof plasmons.

# BIBLIOGRAPHY


[1] T. Phillips and J. Keene. "Submillimeter Astronomy." Proc. IEEE, **80** (1992), 1662.

[2] C. Kulesa. "Terahertz Spectroscopy for Astronomy: From Comets to Cosmology." IEEE Trans. Terahertz Sci. Technol., **1** (2011), 232.

[3] P. H. Siegel. "Terahertz technology." IEEE T. Microw. Theory, **50** (2002), 910.

[4] T. Nagatsuma, S. Horiguchi, Y. Minamikata, Y. Yoshimizu, S. Hisatake, S. Kuwano, N. Yoshimoto, J. Terada and H. Takahashi. "Terahertz Wireless Communications based on Photonics Technologies." Opt. Express, **21** (2013), 23736.

[5] X. Li, J. Yu, J. Zhang, Z. Dong, F. Li and N. Chi. "A 400G Optical Wireless Integration Delivery System." Opt. Express, **21** (2013), 18813.

[6] R. Appleby and H. B. Wallace. "Standoff Detection of Weapons and Contraband in the 100 GHz to 1 THz Region." IEEE T. Antenn. Propag., **55** (2007), 2944.

[7] H. J. Hansen. "Standoff Detection using Millimeter and Submillimeter Wave Spectroscopy." Proc. IEEE, **95** (2007), 1691.

[8] A. Davies. "Terahertz Spectroscopy of Explosives and Drugs." Mater. Today, **11** (2008), 18.

[9] H. Liu, H. Zhong, N. Karpowicz, Y. Chen and X. Zhang. "Terahertz Spectroscopy and Imaging for Defense and Security Applications." Proc. IEEE, **95** (2007), 1514.

[10] K. Kawase, Y. Ogawa, Y. Watanabe and H. Inoue. "Non-destructive Terahertz Imaging of Illicit Drugs using Spectral Fingerprints." Opt. Express, **11** (2003), 2549.

[11] E. Pickwell and V. P. Wallace. "Biomedical Applications of Terahertz Technology." J. Phys. D - Appl. Phys., **39** (2006), R301.

[12] X. Xin, H. Altan, A. Saint, D. Matten and R. R. Alfano. "Terahertz Absorption Spectrum of Para and Ortho Water Vapors at Different Humidities at Room Temperature." J. Appl. Phys., **100** (2006), 094905.

[13] R. T. Hall and J. M. Dowling. "Pure Rotational Spectrum of Water Vapor." J. Chem. Phys., **47** (1967), 2454.

[14] R. A. Cheville and D. Grischkowsky. "Far-infrared Foreign and Self-broadened Rotational Linewidths of High-temperature Water Vapor." J. Opt. Soc. Am. B, **16** (1999), 317.

[15] R. J. Falconer and A. G. Markelz. "Terahertz Spectroscopic Analysis of Peptides and Proteins." J. Infrared Millim. Te., **33** (2012), 973.

[16] L. Thrane, R. H. Jacobsen, P. Uhd Jepsen and S. R. Keiding. "THz reflection Spectroscopy of Liquid Water." Chem. Phys. Lett., **240** (1995), 330.

[17] C. Ronne and S. Keiding. "Low Frequency Spectroscopy of Liquid Water using THz-Time Domain Spectroscopy." J. Mol. Liq., **101** (2002), 199.

[18] A. Markelz. "Terahertz Dielectric Sensitivity to Biomolecular Structure and Function." IEEE. J. Sel. Top. Quant., **14** (2008), 180.

[19] A. Markelz, A. Roitberg and E. Heilweil. "Pulsed Terahertz Spectroscopy of DNA, Bovine Serum Albumin and Collagen between 0.1 and 2.0 THz." Chem. Phys. Lett., **320** (2000), 42.

[20] E. R. Brown, E. A. Mendoza, D. Xia and S. R. J. Brueck. "Narrow THz Spectral Signatures Through an RNA Solution in Nanofluidic Channels." IEEE Sens. J., **10** (2010), 755.

[21] P. F. Taday. "Applications of Terahertz Spectroscopy to Pharmaceutical Sciences." Philos. T. R. Soc. A, **362** (2004), 351.

[22] J. A. Zeitler, K. Kogermann, J. Rantanen, T. Rades, P. F. Taday, M. Pepper, J. Aaltonen and C. J. Strachan. "Drug Hydrate Systems and Dehydration Processes studied by Terahertz Pulsed Spectroscopy." Int. J. Pharm., **334** (2007), 78.

[23] U. Jepsen, P, U. Moller and H. Merbold. "Investigation of Aqueous Alcohol and Sugar Solutions with Reflection Terahertz Time-domain Spectroscopy." Opt. Express, **15** (2007), 14717.

[24] M. Walther, P. Plochocka, B. Fischer, H. Helm and P. Uhd Jepsen. "Collective Vibrational Modes in Biological Molecules Investigated by Terahertz Time-domain Spectroscopy." Biopolymers, **67** (2002), 310.

[25] H.-B. Liu and X.-C. Zhang. "Dehydration Kinetics of D-glucose Monohydrate studied using THz Time-domain Spectroscopy." Chem. Phys. Lett., **429** (2006), 229.

[26] J. T. Kindt and C. A. Schmuttenmaer. "Far-Infrared Dielectric Properties of Polar Liquids Probed by Femtosecond Terahertz Pulse Spectroscopy ." J. Phys. Chem., **100** (1996), 10373.

[27] B. Fischer, M. Hoffmann, H. Helm, G. Modjesch and P. U. Jepsen. "Chemical Recognition in Terahertz Time-domain Spectroscopy and Imaging." Semicond. Sci. Tech., **20** (2005), S246.

[28] Y. Hu, P. Huang, L. Guo, X. Wang and C. Zhang. "Terahertz Spectroscopic Investigations of Explosives." Phys. Lett. A, **359** (2006), 728.

[29] J. Li. "Optical Parameters of Vegetable Oil studied by Terahertz Time-domain Spectroscopy." Appl. Spectrosc., **64** (2010), 231.

[30] J. Li and X. Li. "Determination Principal Component Content of Seed Oils by THz-TDS." Chem. Phys. Lett., **476** (2009), 92.

[31] S. Gorenflo, U. Tauer, I. Hinkov, A. Lambrecht, R. Buchner and H. Helm. "Dielectric Properties of OilWater Complexes using Terahertz Transmission Spectroscopy." Chem. Phys. Lett., **421** (2006), 494.

[32] R. M. Woodward, B. E. Cole, V. P. Wallace, R. J. Pye, D. D. Arnone, E. H. Linfield and M. Pepper. "Terahertz Pulse Imaging in Reflection Geometry of Human Skin Cancer and Skin Tissue." Phys. Med. Biol., **47** (2002), 3853.

[33] S. J. Oh, J. Choi, I. Maeng, J. Y. Park, K. Lee, Y.-M. Huh, J.-S. Suh, S. Haam and J.-H. Son. "Molecular Imaging with Terahertz Waves." Opt. Express, **19** (2011), 4009.

[34] G. W. Chantry. Long-wave Optics (The Science and Technology of Infrared and Near-millimetre Waves): Applications. Academic Press, London (1984).

[35] R. E. Miles, X.-C. Zhang, H. Eisele and A. Krotkus (Eds.). Terahertz Frequency Detection and Identification of Materials and Objects. Springer, Dordrecht, The Netherlands (2007).

[36] S. L. Dexheimer (Ed.). Terahertz Spectroscopy: Principles and Applications. CRC Press, Boca Raton (2008).

[37] W. Withayachumnankul, G. M. Png, X. Yin, S. Atakaramians, I. Jones, H. Lin, B. S. Y. Ung, J. Balakrishnan, B. W.-H. Ng, B. Ferguson, S. P. Mickan, B. M. Fischer and D. Abbott. "T-Ray Sensing and Imaging." Proc. IEEE, **95** (2007), 1528.

[38] M. C. Beard, G. M. Turner and C. A. Schmuttenmaer. "Terahertz Spectroscopy." J. Phys. Chem. B., **106** (2002), 7146.

[39] P. H. Siegel. "Terahertz Technology in Biology and Medicine." IEEE T. Microw. Theory, **52** (2004), 2438.

[40] C. A. Schmuttenmaer. "Exploring Dynamics in the Far-infrared with Terahertz Spectroscopy." Chem. Rev., **104** (2004), 1759.

[41] G. L. Carr, M. C. Martin, W. R. McKinney, K. Jordan, G. R. Neil and G. P. Williams. "High-power Terahertz Radiation from Relativistic Electrons." Nature, **420** (2002), 153.

[42] M. Tonouchi. "Cutting-edge Terahertz Technology." Nat. Photonics, **1** (2007), 97.

[43] B. S. Williams. "Terahertz Quantum-cascade Lasers." Nat. Photonics, **1** (2007), 517.

[44] F. Hindle, A. Cuisset, R. Bocquet and G. Mouret. "Continuous-wave Terahertz by Photomixing: Applications to Gas Phase Pollutant Detection and Quantification." C. R. Phys., **9** (2008), 262.

[45] J. Demers, R. Logan and E. Brown. "An Optically Integrated Coherent Frequency-domain THz Spectrometer with Signal-to-noise Ratio up to 80 dB." Microwave Photonics, 2007 IEEE International Topical Meeting on, (2007), 92.

[46] J.-I. Nishizawa, T. Sasaki and T. Tanno. "Coherent Terahertz-wave Generation from Semiconductors and its Applications in Biological Sciences." J. Phys. Chem. Solids, **69** (2008), 693.

[47] G. Haran, W. Sun, K. Wynne and R. Hochstrasser. "Femtosecond Far-infrared Pump-probe Spectroscopy: A New Tool for Studying Low-frequency Vibrational Dynamics in Molecular Condensed Phases." Chem. Phys. Lett., **274** (1997), 365.

[48] R. McElroy and K. Wynne. "Ultrafast Dipole Solvation Measured in the Far Infrared." Phys. Rev. Lett., **79** (1997), 3078.

[49] "Learn.Genetics." `http://learn.genetics.utah.edu/content/cells/scale/`, (2014).

[50] H. Hirori, K. Yamashita, M. Nagai and K. Tanaka. "Attenuated Total Reflection Spectroscopy in Time Domain Using Terahertz Coherent Pulses." Jpn. J. Appl. Phys., **43** (2004), L1287.

[51] H. Hirori, M. Nagai and K. Tanaka. "Destructive Interference Effect on Surface Plasmon Resonance in Terahertz Attenuated Total Reflection." Opt. Express, **13** (2005), 10801.

[52] A. J. Ward and J. B. Pendry. "Refraction and Geometry in Maxwell's Equations." J. Mod. Optic., **43** (1996), 773.

[53] J. Pendry, A. Holden, D. Robbins and W. Stewart. "Magnetism from Conductors and Enhanced Nonlinear Phenomena." IEEE T. Microw. Theory, **47** (1999), 2075.

[54] J. B. Pendry, A. J. Holden, D. J. Robbins and W. J. Stewart. "Low Frequency Plasmons in Thin-Wire Structures." J. Phys. - Condens. Mat., **10** (1998), 4785.

[55] J. B. Pendry. "Negative Refraction Makes a Perfect Lens." Phys. Rev. Lett, **85** (2000), 3966.

[56] J. B. Pendry. "A Chiral Route to Negative Refraction." Science, **306** (2004), 1353.

[57] S. Linden, C. Enkrich, M. Wegener, J. Zhou, T. Koschny and C. M. Soukoulis. "Magnetic Response of Metamaterials at 100 Terahertz." Science, **306** (2004), 1351.

[58] C. Enkrich, M. Wegener, S. Linden, S. Burger, L. Zschiedrich, F. Schmidt, J. F. Zhou, T. Koschny and C. M. Soukoulis. "Magnetic Metamaterials at Telecommunication and Visible Frequencies." Phys. Rev. Lett., **95** (2005), 5.

[59] G. Dolling, C. Enkrich, M. Wegener and S. Linden. "Low-loss Negative-index Metamaterial at Telecommunication Wavelengths." Opt. Lett., **31** (2006), 1800.

[60] U. K. Chettiar, A. V. Kildishev, T. A. Klar and V. M. Shalaev. "Negative Index Metamaterial Combining Magnetic Resonators with Metal Films." Opt. Express, **14** (2006), 7872.

[61] J. Valentine, S. Zhang, T. Zentgraf, E. Ulin-Avila, D. A. Genov, G. Bartal and X. Zhang. "Three-dimensional Optical Metamaterial with a Negative Refractive Index." Nature, **455** (2008), 376.

[62] S. Xi, H. Chen, T. Jiang, L. Ran, J. Huangfu, B.-I. Wu, J. A. Kong and M. Chen. "Experimental Verification of Reversed Cherenkov Radiation in Left-Handed Metamaterial." Phys. Rev. Lett., **103** (2009), 194801.

[63] S. N. Galyamin, A. V. Tyukhtin, A. Kanareykin and P. Schoessow. "Reversed Cherenkov-Transition Radiation by a Charge Crossing a Left-Handed Medium Boundary." Phys. Rev. Lett., **103** (2009), 194802.

[64] S. Anantha Ramakrishna and J. B. Pendry. "Spherical Perfect lens: Solutions of Maxwells Equations for Spherical Geometry." Phys. Rev. B., **69** (2004), 115115.

[65] M. Tsang and D. Psaltis. "Magnifying Perfect Lens and Superlens Design by Coordinate Transformation." Phys. Rev. B., **77** (2008), 035122.

[66] V. G. Veselago. "The Electrodynamics of Substances with Simultaneously Negative Values of $\epsilon$ and $\mu$." Uspekhi Fizicheskikh Nauk, **10** (1968).

[67] A. Alù and N. Engheta. "All Optical Metamaterial Circuit Board at the Nanoscale." Phys. Rev. Lett., **103** (2009), 143902.

[68] B. Edwards, A. Alù, M. Young, M. Silveirinha and N. Engheta. "Experimental Verification of Epsilon-Near-Zero Metamaterial Coupling and Energy Squeezing Using a Microwave Waveguide." Phys. Rev. Lett., **100** (2008), 033903.

[69] B. Edwards and N. Engheta. "Experimental Verification of Displacement-Current Conduits in Metamaterials-Inspired Optical Circuitry." Phys. Rev. Lett., **108** (2012), 193902.

[70] M. Silveirinha and N. Engheta. "Tunneling of Electromagnetic Energy through Subwavelength Channels and Bends using $\epsilon$-Near-Zero Materials." Phys. Rev. Lett., **97** (2006), 157403.

[71] N. Engheta, A. Salandrino and A. Alù. "Circuit Elements at Optical Frequencies: Nanoinductors, Nanocapacitors, and Nanoresistors." Phys. Rev. Lett., **95** (2005).

[72] D. Schurig, J. J. Mock, B. J. Justice, S. A. Summer, J. B. Pendry, A. F. Starr and D. R. Smith. "Metamaterial Electromagnetic Cloak at Microwave Frequencies." Science, **314** (2006), 977.

[73] B. Baumeier, T. Leskova and A. Maradudin. "Cloaking from Surface Plasmon Polaritons by a Circular Array of Point Scatterers." Phys. Rev. Lett., **103** (2009), 246803.

[74] Y. Lai, H. Y. Chen, Z.-Q. Zhang and C. Chan. "Complementary Media Invisibility Cloak that Cloaks Objects at a Distance Outside the Cloaking Shell." Phys. Rev. Lett., **102** (2009), 093901.

[75] T. Ergin, N. Stenger, P. Brenner, J. B. Pendry and M. Wegener. "Three-Dimensional Invisibility Cloak at Optical Wavelengths." Science Express, (2010).

[76] H. Chen, B. Zheng, L. Shen, H. Wang, X. Zhang, N. I. Zheludev and B. Zhang. "Ray-optics Cloaking Devices for Large Objects in Incoherent Natural Light." Nat. Commun., **4** (2013), 2652.

[77] S. Zhang, W. Fan, B. K. Minhas, A. Frauenglass, K. J. Malloy and S. R. J. Brueck. "Midinfrared Resonant Magnetic Nanostructures Exhibiting a Negative Permeability." Phys. Rev. Lett., **94** (2005), 1.

[78] S. Zhang, J. Zhou, Y.-S. Park, J. Rho, R. Singh, S. Nam, A. K. Azad, H.-T. Chen, X. Yin, A. J. Taylor and X. Zhang. "Photoinduced Handedness Switching in Terahertz Chiral Metamolecules." Nat. Commun., **3** (2012), 942.

[79] O. Paul, C. Imhof, B. Lägel, S. Wolff, J. Heinrich, S. Höfling, A. Forchel, R. Zengerle, R. Beigang and M. Rahm. "Polarization-independent Active Metamaterial for High-frequency Terahertz Modulation." Opt. Express, **17** (2009), 819.

[80] Z. C. Chen, N. R. Han, Z. Y. Pan, Y. D. Gong, T. C. Chong and M. H. Hong. "Tunable Resonance Enhancement of Multi-layer Terahertz Metamaterials Fabricated by Parallel Laser Micro-lens Array Lithography on Flexible Substrates." Opt. Mat. Express, **1** (2011), 151.

[81] H. T. Chen, J. F. O'Hara, A. K. Azad and A. J. Taylor. "Manipulation of Terahertz Radiation using Metamaterials." Laser Photon. Rev., **5** (2011), 513.

[82] Q.-Y. Wen, H.-W. Zhang, Y.-S. Xie, Q.-H. Yang and Y.-L. Liu. "Dual Band Terahertz Metamaterial Absorber: Design, Fabrication, and Characterization." Appl. Phys. Lett., **95** (2009), 241111.

[83] E. Plum, V. A. Fedotov, A. S. Schwanecke, N. I. Zheludev and Y. Chen. "Giant Optical Gyrotropy due to Electromagnetic Coupling." Appl. Phys. Lett., **90** (2007), 223113.

[84] E. Plum, V. A. Fedotov and N. I. Zheludev. "Extrinsic Electromagnetic Chirality in Metamaterials." J. Opt. A - Pure Appl. Op., **11** (2009), 074009.

[85] J. Wu, B. Ng, S. P. Turaga, M. B. H. Breese, S. A. Maier, A. A. Bettiol and H. O. Moser. "Free-standing Terahertz Chiral Meta-foils Exhibiting Strong Optical Activity and Negative Refractive Index." Appl. Phys. Lett., **103** (2013), 141106.

[86] H. Tao, A. C. Strikwerda, K. Fan, C. M. Bingham, W. J. Padilla, X. Zhang and R. D. Averitt. "Terahertz Metamaterials on Free-standing Highly-flexible Polyimide Substrates." J. Phys. D - Appl. Phys., **41** (2008), 232004.

[87] N. R. Han, Z. C. Chen, C. S. Lim, B. Ng and M. H. Hong. "Broadband Multi-layer Terahertz Metamaterials Fabrication and Characterization on Flexible Substrates." Opt. Express, **19** (2011), 6990.

[88] R. Melik, E. Unal, N. Kosku Perkgoz, C. Puttlitz and H. V. Demir. "Flexible Metamaterials for Wireless Strain Sensing." Appl. Phys. Lett., **95** (2009), 181105.

[89] F. Miyamaru, M. Wada Takeda and K. Taima. "Characterization of Terahertz Metamaterials Fabricated on Flexible Plastic Films: Toward Fabrication of Bulk Metamaterials in Terahertz Region." Appl. Phys. Express, **2** (2009), 042001.

[90] R. Singh, I. a. I. Al-Naib, M. Koch and W. Zhang. "Asymmetric Planar Terahertz Metamaterials." Opt. Express, **18** (2010), 13044.

[91] R. Singh, I. A. I. Al-Naib, M. Koch and W. Zhang. "Sharp Fano Resonances in THz Metamaterials." Opt. Express, **19** (2011), 6312.

[92] H. Tao, A. C. Strikwerda, M. Liu, J. P. Mondia, E. Ekmekci, K. Fan, D. L. Kaplan, W. J. Padilla, X. Zhang, R. D. Averitt and F. G. Omenetto. "Performance Enhancement of Terahertz Metamaterials on Ultrathin Substrates for Sensing Applications." Appl. Phys. Lett., **97** (2010), 261909.

[93] B. Reinhard, K. M. Schmitt, V. Wollrab, J. Neu, R. Beigang and M. Rahm. "Metamaterial Near-field Sensor for Deep-subwavelength Thickness Measurements and Sensitive Refractometry in the Terahertz Frequency Range." Appl. Phys. Lett., **100** (2012), 221101.

[94] J. F. O'Hara, R. Singh, I. Brener, E. Smirnova, J. Han, A. J. Taylor and W. Zhang. "Thin-film Sensing with Planar Terahertz Metamaterials: Sensitivity and Limitations." Opt. Express, **16** (2008), 1786.

[95] B. Luk'yanchuk, N. I. Zheludev, S. A. Maier, N. J. Halas, P. Nordlander, H. Giessen and C. T. Chong. "The Fano Resonance in Plasmonic Nanostructures and Metamaterials." Nat. Mater., **9** (2010), 707.

[96] N. Verellen, Y. Sonnefraud, H. Sobhani, F. Hao, V. V. Moshchalkov, P. Van Dorpe, P. Nordlander and S. A. Maier. "Fano Resonances in Individual Coherent Plasmonic Nanocavities." Nano Lett., **9** (2009), 16631667.

[97] F. Hao, Y. Sonnefraud, P. Van Dorpe, S. A. Maier, N. J. Halas and P. Nordlander. "Symmetry Breaking in Plasmonic Nanocavities: Subradiant LSPR Sensing and a Tunable Fano Resonance." Nano Lett., **8** (2008), 3983.

[98] J. B. Lassiter, H. Sobhani, J. A. Fan, J. Kundu, F. Capasso, P. Nordlander and N. J. Halas. "Fano Resonances in Plasmonic Nanoclusters: Geometrical and Chemical Tunability." Nano Lett., **10** (2010), 3184.

[99] Z. Liao, B. C. Pan, X. Shen and T. J. Cui. "Multiple Fano Resonances in Spoof Localized Surface Plasmons." Opt. Express, **22** (2014), 15710.

[100] B. Pradarutti, G. Torosyan, M. Theuer and R. Beigang. "Fano Profiles in Transmission Spectra of Terahertz Radiation through One-dimensional Periodic Metallic Structures." Appl. Phys. Lett., **97** (2010), 244103.

[101] L. Deng, J. Teng, H. Liu, Q. Y. Wu, J. Tang, X. Zhang, S. a. Maier, K. P. Lim, C. Y. Ngo, S. F. Yoon and S. J. Chua. "Direct Optical Tuning of the Terahertz Plasmonic Response of InSb Subwavelength Gratings." Adv. Opt. Mat., **1** (2013), 128.

[102] V. Giannini, A. Berrier, S. A. Maier, J. A. Sánchez-Gil and J. G. Rivas. "Scattering Efficiency and Near Field Enhancement of Active Semiconductor Plasmonic Antennas at Terahertz Frequencies." Opt. Express, **18** (2010), 2797.

[103] V. A. Markel. "Coupled-dipole Approach to Scattering of Light from a One-dimensional Periodic Dipole Structure." J. Mod. Optic., **40** (1993), 2281.

[104] V. A. Markel. "Divergence of Dipole Sums and the Nature of Non-Lorentzian Exponentially Narrow Resonances in One-dimensional Periodic Arrays of Nanospheres." J. Phys. B - At. Mol. Opt., **38** (2005), L115.

[105] S. Zou, N. Janel and G. C. Schatz. "Silver Nanoparticle Array Structures that Produce Remarkably Narrow Plasmon Lineshapes." J. Chem. Phys., **120** (2004), 10871.

[106] B. Auguié and W. Barnes. "Collective Resonances in Gold Nanoparticle Arrays." Phys. Rev. Lett., **101** (2008), 143902.

[107] G. Vecchi, V. Giannini and J. Gómez Rivas. "Surface Modes in Plasmonic Crystals Induced by Diffractive Coupling of Nanoantennas." Phys. Rev. B, **80** (2009), 201401.

[108] G. Vecchi, V. Giannini and J. Gómez Rivas. "Shaping the Fluorescent Emission by Lattice Resonances in Plasmonic Crystals of Nanoantennas." Phys. Rev. Lett., **102** (2009), 146807.

[109] V. Giannini, G. Vecchi and J. Gómez Rivas. "Lighting Up Multipolar Surface Plasmon Polaritons by Collective Resonances in Arrays of Nanoantennas." Phys. Rev. Lett., **105** (2010), 266801.

[110] T. Ebbesen, H. Lezec, H. Ghaemi, T. Thio and P. Wolff. "Extraordinary Optical Transmission through Sub-wavelength Hole Arrays." Nature, **391** (1998), 667.

[111] L. Martín-Moreno, F. García-Vidal, H. Lezec, K. Pellerin, T. Thio, J. B. Pendry and T. Ebbesen. "Theory of Extraordinary Optical Transmission through Subwavelength Hole Arrays." Phys. Rev. Lett., **86** (2001), 1114.

[112] H. J. Lezec, A. Degiron, E. Devaux, R. A. Linke, L. Martin-Moreno, F. J. Garcia-Vidal and T. W. Ebbesen. "Beaming Light from a Subwavelength Aperture." Science, **297** (2002), 820.

[113] W. L. Barnes, W. A. Murray, J. Dintinger, E. Devaux and T. W. Ebbesen. "Surface Plasmon Polaritons and Their Role in the Enhanced Transmission of Light through Periodic Arrays of Subwavelength Holes in a Metal Film." Phys. Rev. Lett., **92** (2004), 107401.

[114] J. Bravo-Abad, A. Degiron, F. Przybilla, C. Genet, F. J. García-Vidal, L. Martín-Moreno and T. W. Ebbesen. "How Light Emerges from an Illuminated Array of Subwavelength Holes." Nat. Phys., **2** (2006), 120.

[115] F. J. Garcia-Vidal, T. W. Ebbesen and L. Kuipers. "Light Passing through Subwavelength Apertures." Rev. Mod. Phys., **82** (2010), 729.

[116] J. B. Pendry, L. Martín-Moreno and F. J. Garcia-Vidal. "Mimicking surface plasmons with structured surfaces." Science, **305** (2004), 847.

[117] F. García-Vidal and L. Martín-Moreno. "Transmission and Focusing of Light in One-dimensional Periodically Nanostructured Metals." Phys. Rev. B., **66** (2002), 155412.

[118] A. I. Fernández-Domínguez, E. Moreno, L. Martín-Moreno and F. García-Vidal. "Guiding Terahertz Waves Along Subwavelength Channels." Phys. Rev. B, **79** (2009), 233104.

[119] F. de León-Pérez, G. Brucoli, F. J. García-Vidal and L. Martín-Moreno. "Theory on the Scattering of Light and Surface Plasmon Polaritons by Arrays of Holes and Dimples in a Metal Film." New J. Phys., **10** (2008), 105017.

[120] L. Martín-Moreno and F. J. García-Vidal. "Minimal Model for Optical Transmission through Holey Metal Films." J. Phys.: Condens. Matter, **20** (2008), 304214.

[121] A. P. Hibbins, E. Hendry, M. J. Lockyear and J. R. Sambles. "Prism Coupling to 'Designer' Surface Plasmons." Opt. Express, **16** (2008), 20441.

[122] G. Goubau. "Surface Waves and Their Application to Transmission Lines." J. Appl. Phys., **21** (1950), 1119.

[123] C. R. Williams, S. R. Andrews, S. A. Maier, A. I. Fernández-Domínguez, L. Martín-Moreno and F. J. García-Vidal. "Highly Confined Guiding of Terahertz Surface Plasmon Polaritons on Structured Metal Surfaces." Nat. Photonics, **2** (2008), 175.

[124] L. Shen, X. Chen and T. J. Yang. "Terahertz Surface Plasmon Polaritons on Periodically Corrugated Metal Surfaces." Opt. Express, **16** (2008), 3326.

[125] A. I. Fernandez-Dominguez, L. Martin-Moreno, F. J. Garcia-Vidal, S. R. Andrews and S. A. Maier. "Spoof Surface Plasmon Polariton Modes Propagating Along Periodically Corrugated Wires." IEEE J. Sel. Top. Quant., **14** (2008), 1515.

[126] K. Song and P. Mazumder. "Active Terahertz Spoof Surface Plasmon Polariton Switch Comprising the Perfect Conductor Metamaterial." IEEE T. Electron Dev., **56** (2009), 2792.

[127] M. Navarro-Cia, M. Beruete, S. Agrafiotis, F. Falcone, M. Sorolla and S. A. Maier. "Broadband Spoof Plasmons and Subwavelength Electromagnetic Energy Confinement on Ultrathin Metafilms." Opt. Express, **17** (2009), 18184.

[128] C. R. Williams, M. Misra, S. R. Andrews, S. A. Maier, S. Carretero-Palacios, S. G. Rodrigo, F. J. Garcia-Vidal and L. Martin-Moreno. "Dual Band Terahertz Waveguiding on a Planar Metal Surface Patterned with Annular Holes." Appl. Phys. Lett., **96** (2010), 011101.

[129] A. Rusina, M. Durach and M. I. Stockman. "Theory of Spoof Plasmons in Real Metals." Appl. Phys. A, **100** (2010), 375.

[130] N. Yu, Q. J. Wang, M. A. Kats, J. A. Fan, S. P. Khanna, L. Li, A. G. Davies, E. H. Linfield and F. Capasso. "Designer Spoof Surface Plasmon Structures Collimate Terahertz Laser Beams." Nat. Mater., **9** (2010), 730.

[131] M. A. Kats, D. Woolf, R. Blanchard, N. Yu and F. Capasso. "Spoof Plasmon Analogue of Metal-Insulator-Metal Waveguides." Opt. Express, **19** (2011), 14860.

[132] J. J. Wood, L. A. Tomlinson, O. Hess, S. A. Maier and A. I. Fernández-Domínguez. "Spoof plasmon polaritons in slanted geometries." Phys. Rev. B, **85** (2012), 075441.

[133] T. J. Constant, T. S. Taphouse, H. J. Rance, S. C. Kitson, A. P. Hibbins and J. R. Sambles. "Surface Plasmons on Zig-Zag Gratings." Opt. Express, **20** (2012), 23921.

[134] R. E. Collin. Field Theory of Guided Waves. 2nd edition. Wiley-IEEE, New York (1990).

[135] C. A. Balanis. Antenna Theory: Analysis and Design. 3rd edition. Wiley, New Jersey (2005).

[136] J. D. Jackson. Classical Electrodynamics. 3rd edition. Wiley, New York (1998).

[137] L. Rayleigh. "On the Dynamical Theory of Gratings." Proceedings of the Royal Society of London. Series A, Containing Papers of a Mathematical and Physical Character, **79** (1907), 399.

[138] E. G. Loewen and E. Popov. Diffraction Gratings and Applications. Marcel Dekker, New York (1997).

[139] A. Hessel and A. A. Oliner. "A New Theory of Woods Anomalies on Optical Gratings." Appl. Opt., **4** (1965), 1275.

[140] R. H. Ritchie, E. T. Arakawa, J. J. Cowan and R. N. Hamm. "Surface-plasmon Resonance Effect in Grating Diffraction." Phys. Rev. Lett., **21** (1968), 1530.

[141] S. A. Maier. Plasmonics: Fundamentals and Applications. Springer, New York (2007).

[142] A. I. Fernández-Domínguez, F. García-Vidal and L. Martín-Moreno. "Resonant Transmission of Light through Finite Arrays of Slits." Phys. Rev. B, **76** (2007), 235430.

[143] F. J. Garcia-Vidal, L. Martín-Moreno and J. B. Pendry. "Surfaces with Holes in Them: New Plasmonic Metamaterials." J. Opt. A - Pure Appl. Op., **7** (2005), S97.

[144] A. Maradudin (Ed.). Structured Surfaces as Optical Metamaterials. 1st edition. Cambridge University Press, Cambridge (2011).

[145] F. García de Abajo. "Colloquium: Light Scattering by Particle and Hole Arrays." Rev. Mod. Phys., **79** (2007), 1267.

[146] A. I. Fernandez-Domínguez. "Electromagnetic Phenomena based on Surface Modes and their Transfer to Atom Optics." Ph.d., Universidad Autonoma de Madrid (2009).

[147] M. L. Boas. Mathematical Methods in the Physical Sciences. 3rd edition. Wiley, New York (2005).

[148] A. V. Oppenheim, R. W. Schafer and J. R. Buck. Discrete-Time Signal Processing. Prentice-Hall, New Jersey (1998).

[149] F. J. Harris. "On the Use of Windows for Harmonic Analysis with the Discrete Fourier Transform." Proc. IEEE, **66** (1978), 51.

[150] R. Bretzlaff and T. Bahder. "Apodization Effects in Fourier Transform Infrared Difference Spectra." Revue Phys. Appl., **21** (1986), 833.

[151] B. Ng, S. M. Hanham, V. Giannini, Z. C. Chen, M. Tang, Y. F. Liew, N. Klein, M. H. Hong and S. A. Maier. "Lattice Resonances in Antenna Arrays for Liquid Sensing in the Terahertz Regime." Opt. Express, **19** (2011), 14653.

[152] L. J. Sherry, S.-H. Chang, G. C. Schatz, R. P. Van Duyne, B. J. Wiley and Y. Xia. "Localized Surface Plasmon Resonance Spectroscopy of Single Silver Nanocubes." Nano Lett., **5** (2005), 2034.

[153] C. Debus and P. H. Bolivar. "Frequency Selective Surfaces for High Sensitivity Terahertz Sensing." Appl. Phys. Lett., **91** (2007), 184102.

[154] B. Auguié, X. Bendaña, W. Barnes and F. García de Abajo. "Diffractive Arrays of Gold Nanoparticles near an Interface: Critical Role of the Substrate." Phys. Rev. B., **82** (2010), 155447.

[155] L. Duvillaret, F. Garet and J.-L. Coutaz. "A Reliable Method for Extraction of Material Parameters in Terahertz Time-Domain Spectroscopy." IEEE J. Sel. Top. Quant., **2** (1996), 739.

[156] T. Driscoll, G. O. Andreev, D. N. Basov, S. Palit, S. Y. Cho, N. M. Jokerst and D. R. Smith. "Tuned Permeability in Terahertz Split-ring Resonators for Devices and Sensors." Appl. Phys. Lett., **91** (2007), 062511.

[157] C.-Y. Chen, I.-W. Un, N.-H. Tai and T.-J. Yen. "Asymmetric Coupling between Subradiant and Superradiant Plasmonic Resonances and its Enhanced Sensing Performance." Opt. Express, **17** (2009), 15372.

[158] A. I. Fernandez-Dominguez, C. R. Williams, F. J. Garcia-Vidal, L. Martin-Moreno, S. R. Andrews and S. A. Maier. "Terahertz Surface Plasmon Polaritons on a Helically Grooved Wire." Appl. Phys. Lett., **93** (2008), 141109.

[159] F. Miyamaru, S. Hayashi, C. Otani, K. Kawase, Y. Ogawa, H. Yoshida and E. Kato. "Terahertz Surface-wave Resonant Sensor with a Metal Hole Array." Opt. Lett., **31** (2006), 1118.

[160] T. Jiang, L. Shen, X. Zhang and L. Ran. "High-order Modes of Spoof Surface Plasmon Polaritons on Periodically Corrugated Metal Surfaces." Prog. Electromagn. Res., **8** (2009), 91.

[161] A. Otto. "Excitation of Nonradiative Surface Plasma Waves in Silver by the Method of Frustrated Total Reflection." Z. Phys. A - Hadron Nucl., **216** (1968), 398.

[162] H. Raether. Surface Plasmons on Smooth and Rough Surfaces and on Gratings. Springer-Verlag, Berlin and Heidelberg (1988).

[163] R. Ulrich and M. Tacke. "Submillimeter Waveguiding on Periodic Metal Structure." Appl. Phys. Lett., **22** (1973), 251.

[164] C. Rau, G. Torosyan, R. Beigang and K. Nerkararyan. "Prism Coupled Terahertz Waveguide Sensor." Appl. Phys. Lett., **86** (2005), 211119.

[165] J. O'Hara, R. Averitt and A. Taylor. "Prism Coupling to Terahertz Surface Plasmon Polaritons." Opt. Express, **13** (2005), 6117.

[166] Y. S. Joe, A. M. Satanin and C. S. Kim. "Classical Analogy of Fano Resonances." Physica Scripta, **74** (2006), 259.

[167] B. Ng, J. Wu, S. M. Hanham, A. I. Fernández-Domínguez, N. Klein, Y. F. Liew, M. B. H. Breese, M. H. Hong and S. A. Maier. "Spoof Plasmon Surfaces: A Novel Platform for THz Sensing." Adv. Opt. Mat., **1** (2013), 543.

[168] H. Yoshida, Y. Ogawa, Y. Kawai, S. Hayashi, A. Hayashi, C. Otani, E. Kato, F. Miyamaru and K. Kawase. "Terahertz Sensing Method for Protein Detection using a Thin Metallic Mesh." Appl. Phys. Lett., **91** (2007), 253901.

[169] S.-Y. Chiam, R. Singh, J. Gu, J. Han, W. Zhang and A. A. Bettiol. "Increased Frequency Shifts in High Aspect Ratio Terahertz Split Ring Resonators." Appl. Phys. Lett., **94** (2009), 064102.

[170] H. T. Chen, J. F. O'Hara, A. J. Taylor, R. D. Averitt, M. Lee, C. Highstrete and W. J. Padilla. "Complementary Planar Terahertz Metamaterials." Opt. Express, **15** (2007), 1084.

[171] H. Zhao, K. Zhao, L. Tian, Q. Miao and H. Ni. "Optical Property of Biodiesel and its Base Stock in Terahertz Region." Front. Optoelectron., **5** (2012), 214.

[172] J. Saxler, J. Gómez Rivas, C. Janke, H. Pellemans, P. Bolívar and H. Kurz. "Time-domain Measurements of Surface Plasmon Polaritons in the Terahertz Frequency Range." Phys. Rev. B., **69** (2004), 155427.

[173] S. Yamauchi, S. Hatakeyam, Y. Imai and M. Tonouchi. "Terahertz Time-Domain Spectroscopy to Identify and Evaluate Anomer in Lactose." American Journal of Analytical Chemistry, **4** (2013), 756.

[174] Z. Xu and P. Mazumder. "Bio-Sensing by MachZehnder Interferometer Comprising Doubly-Corrugated Spoofed Surface Plasmon Polariton (DC-SSPP) Waveguide." IEEE Trans. Terahertz Sci. Technol., **2** (2012), 460.

[175] M. L. T. Asaki, A. Redondo, T. A. Zawodzinski and A. J. Taylor. "Dielectric Relaxation of Electrolyte Solutions using Terahertz Transmission Spectroscopy." J. Chem. Phys., **116** (2002), 8469.

[176] R. Stratt and M. Maroncelli. "Nonreactive Dynamics in Solution: The Emerging Molecular View of Solvation Dynamics and Vibrational Relaxation." J. Phys. Chem., **100** (1996), 12981.

[177] C. Winnewisser, P. Uhd Jepsen, M. Schall, V. Schyja and H. Helm. "Electro-optic Detection of THz Radiation in $LiTaO_3$, $LiNbO_3$ and ZnTe." Appl. Phys. Lett., **70** (1997), 3069.

[178] P. C. M. Planken, H. K. Nienhuys, H. J. Bakker and T. Wenckebach. "Measurement and Calculation of the Orientation Dependence of Terahertz Pulse Detection in ZnTe." J. Opt. Soc. Am. B, **18** (2001), 313.

[179] EKSPLA. "THz Time-Domain Spectroscopy System: Technical Description and User's Manual." Technical report, EKSPLA (2009).

[180] "Conformal FDTD Mesh Technology Delivers Subcell Accuracy." `https://www.lumerical.com/solutions/innovation/fdtd_conformal_mesh_whitepaper.html`, (2014).

APPENDIX A

# THZ TIME-DOMAIN SPECTROSCOPY: A SHORT OVERVIEW

## A.1 INTRODUCTION

THz-TDS is the main method used for the optical characterisation of the metamaterials described in this thesis. Quick acquisition of broadband data without the need for cryogenic cooling and the ready availability of phase data as an additional source of information as compared to frequency domain methods are but a few of its advantages [3, 36, 40, 48]. THz-TDS allows for the calculation of material dielectric constants without the need for Kramers-Kronig relations [16, 30, 155, 171, 175], the probing of charge and solvation dynamics [36, 176] as well as the ability to conduct more advanced data post-processing such as short-time Fourier transforms (see Chapter 5). Given the centrality of this measurement technique to this thesis, a brief description of the working principles of THz-TDS will be given here in order to facilitate the exposition of the work presented in this thesis. On top of that, details of the quasi-optical and the commercial THz-TDS used for the work conducted in this thesis will also be listed.

## A.2 BASIC OPERATING PRINCIPLES

THz-TDS works on a pump-probe principle where the electric field strength of a picosecond (ps) light pulse is probed at various time points such that the electric field magnitude and direction is recorded over the duration of the pulse to give a complete time domain signal. Frequency domain spectra are then readily available via discrete Fourier transforms. A schematic diagram of a typical THz TDS is shown in Fig. A.1. The spectrometer is pumped by femtosecond (fs) laser pulse.

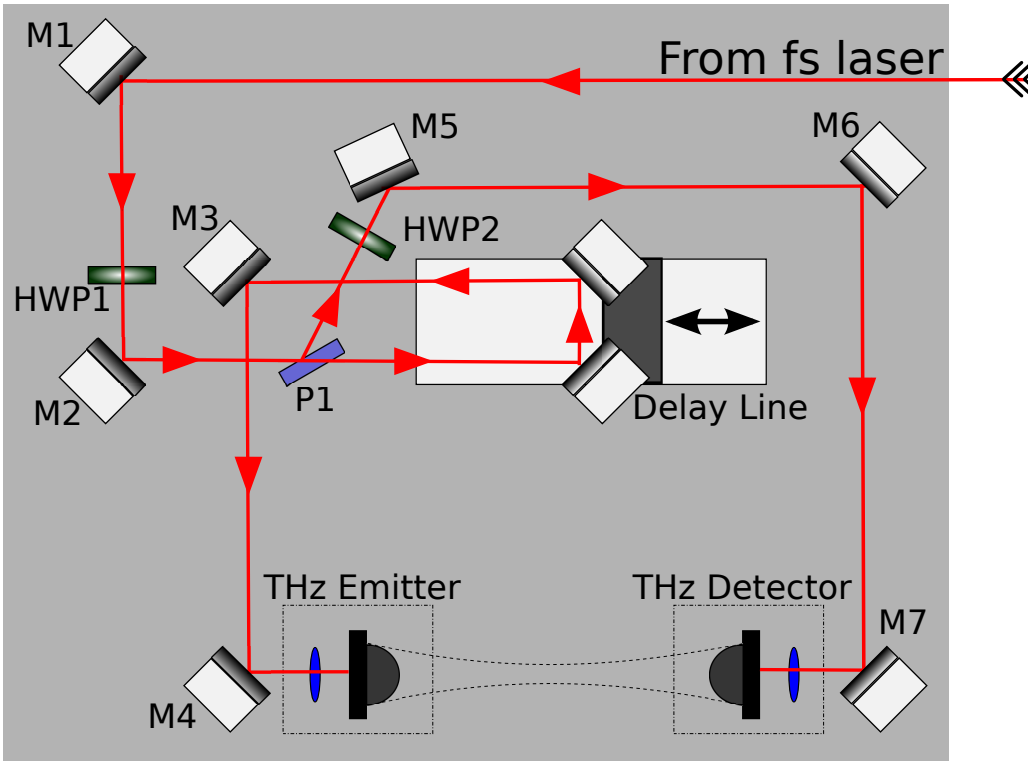



Figure A.1: A schematic diagram of the THz Time-Domain Spectrometer (THz-TDS).

Upon entering the spectrometer, the input beam is split into two: one goes to the emitter ($M1 \rightarrow M2 \rightarrow$ Delay Line $\rightarrow M3 \rightarrow M4 \rightarrow$ Emitter) and the other goes to the detector ($M1 \rightarrow M2 \rightarrow P1 \rightarrow M5 \rightarrow M6 \rightarrow M7 \rightarrow$ Detector) (see Fig. A.1). This beam splitting can be achieved via the use of two half wave plates (*HWP1* and *HWP2*) and a beam-splitting polarizer (*P1*).

Photoconductive antennas fabricated on low-temperature grown gallium arsenide (LT-GaAs) are responsible for the emission and detection of THz light pulses in our THz TDS. These antennae are simply metallic electrodes pointed towards each other with a gap of a few tens of micrometers between them as shown in Fig. A.2. The process of THz light pulse emission is shown in the left panel of Fig. A.3. Light from the fs laser is focused to a point between the electrodes and creates charge carriers in the LT-GaAs which are accelerated towards the metal electrodes via a voltage bias. The accelerating charges emits THz radiation in the form of a picosecond

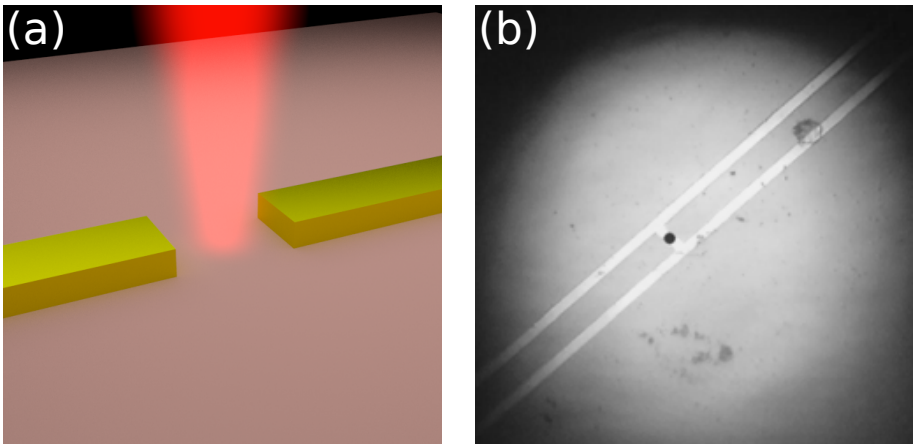



Figure A.2: (a) A close up 3D render of photoconductive antenna. (b) Photo of photoconductive antenna. Reprinted from [179].

pulse. The process of of THz radiation detection is the reversal of the emission process (see right panel of Fig. A.3). Charge carriers, generated by the fs laser pulse, are pushed towards the electrodes by incoming THz radiation resulting in a current. The magnitude and direction of the current corresponds to the magnitude and direction of the incident electric field. Since the excitation of charge carriers is very abrupt and the carrier lifetimes are short, only the electric field at a particular time point is probed with each fs laser pulse. By varying the relative path lengths of the fs laser beam in the emitter and detector arm using an optical delay line (shown in Fig. A.1), electric field data can be collected over the entire time duration of the THz pulse giving a complete picture of the THz time domain signal. Hemispherical high-resistivity silicon lenses are used to focus and direct the light from the emitter to the detector. The other main method of THz pulse emission and detection is through the use of non-linear optical processes in crystals such as lithium niobate ($LiNbO_3$) and zinc telluride (ZnTe) [177, 178].

The LT-GaAs substrate for the photoconductive antennas is made using molecular beam epitaxy with an excess of As flux at temperatures ranging from 180°C to 300°C followed by annealing [40]. This is because GaAs has a carrier lifetime of the order of nanoseconds and would not support a picosecond electromagnetic pulse

on its own. The annealing process results in As clusters in the GaAs substrate acting as *charge sinks* that take away the excited charge carriers very quickly upon application of a voltage bias. The carrier lifetime of the LT-GaAs is reduced to picoseconds timescales allowing for the generation and detection of a picosecond pulse.

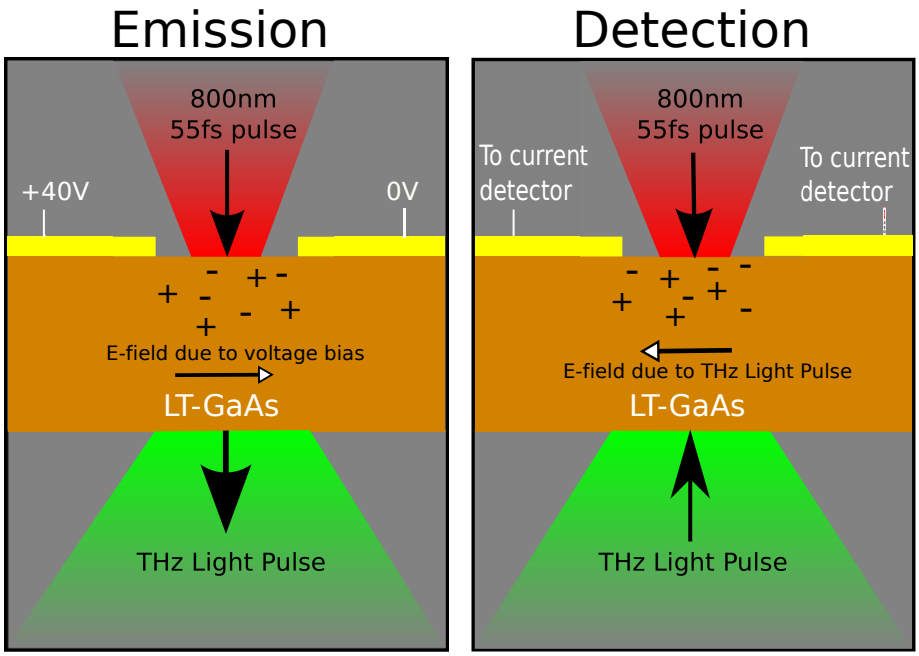



Figure A.3: A diagram explaining the processes of THz light emission and detection using photoconductive antennas on low-temperature grown gallium arsenide (LT-GaAs). **(Left)** Process of emission: 800nm fs laser pulse generates electron-hole pairs in the LT-GaAs which are then accelerated towards the photoconductive antennae via a voltage bias. The accelerating charges results in the emission of a ps pulse. **(Right)** Process of detection: Similar to the emission process, charge carriers are generated in the LT-GaAs by the fs laser pulse. The charges are then pushed towards the photoconductive antennae by the incoming ps pulse resulting in a current which is proportional to the incident electric field. By measuring the current at various time points over the whole duration of the pulse, a time domain signal can be obtained.

A lock-in amplifier is used to significantly reduce background noise in the THz-TDS. This is important because THz photon energies are comparable to $k_BT$ and without the lock-in amplifier, the actual THz pulse would be indiscernible in the environmental thermal noise and noise generated by the laser probe. The THz emitter is modulated at a particular frequency, say 30 kHz, and the received signal

is de-modulated and integrated over a length of time by the lock-in amplifier. This integration process will pick out the signal at the modulation frequency while signal at other frequencies due to noise will be averaged to zero. Typical integration times are between 30 ms to 100 ms. It is precisely this coherent detection scheme that allows the system to be used at room temperature without the use of specialized detectors such as liquid helium cooled bolometers [40].

## A.3 QUASI-OPTICAL TERAHERTZ TIME-DOMAIN SPECTROMETER

A quasi-optical setup was used to conduct the work done in A*STAR (Singapore), as shown in Fig. A.4. The quasi-optical THz-TDS is pumped with a 800 nm Ti:Sapphire laser (Spectra-Physics, Tsunami) with a pulse width of 55 fs at 80 mW and a 40 V bias is applied across the emitter photoconductive antennas. A typical time pulse and frequency spectrum is shown in Fig. A.5 (a) and (b), respectively. As can be seen, the time pulse is approximately 2 ps and a bandwidth of approximately 4 THz with a dynamic range of roughly 60 dB. The sharp dips in the frequency spectrum is due to absorption by water vapour and can be removed by making the measurements in a nitrogen purged chamber.

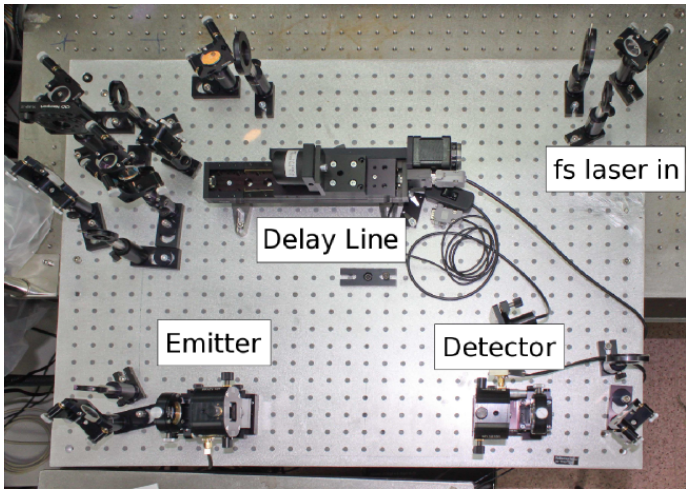



Figure A.4: Photograph of the quasi-optical THz-TDS

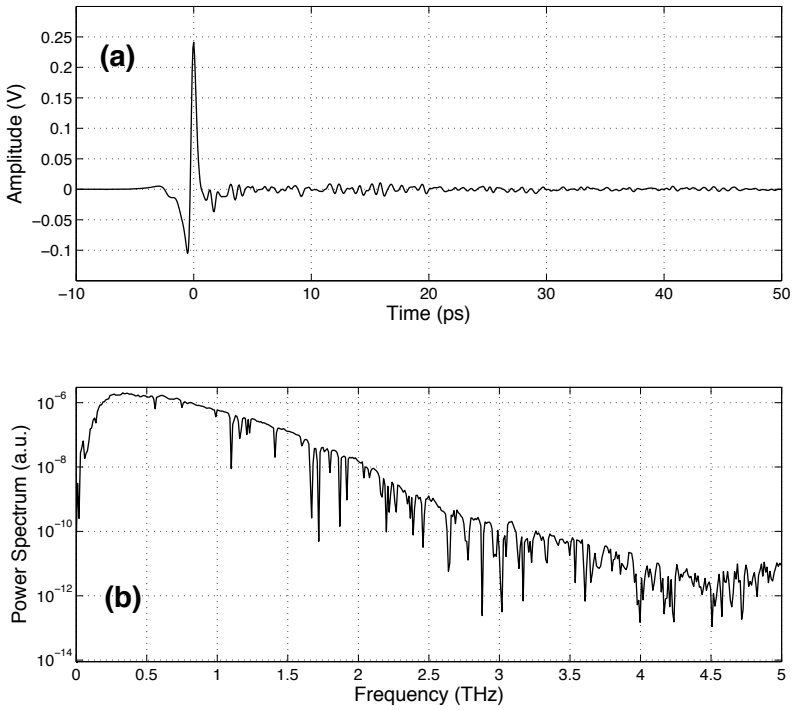



Figure A.5: Time-domain signal (a) and frequency spectrum (b) of the quasi-optical THz-TDS.

## A.4 TERAVIEW SPECTRA 3000

For the work conducted at Imperial College London, a commercial THz-TDS (Teraview Spectra 3000) was used (see Fig. A.6(a)). The THz signal is similar to that shown in Fig. A.5. Most notably, the Teraview Spectra 3000 has a rapid scan delay line and fibre-coupled remote THz emitter and detector. The rapid scan delay line is capable of acquiring time-domain data over a 40 ps time window at a rate of 30 Hz to 100 Hz, allowing us to average our readings over many measurements very quickly and observe *almost live* changes in signal. The fibre-coupled remote emitter and detector (see Fig. A.6(b)) enables the flexible placement and direction of the THz radiation such as the scattering edge coupling setup seen in Chapter 5. The fs laser pulse is guided via optical fibres encased in flexible metallic tubes to

miniaturised THz source and detector operating on the photoconductive antenna principle described in Appendix A.2. The THz light is then focused via polymer lenses with a focal length of approximately 5 cm.

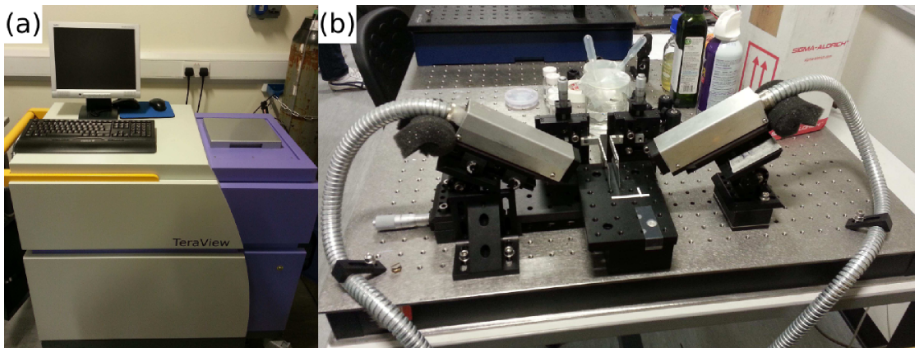



Figure A.6: (a) Photograph of Teraview Spectra 3000 THz-TDS. (b) Photograph of remote THz emitter and detector heads used in the scattering edge coupling scheme for the broadband SPS experiments.

APPENDIX B

# SIMULATION METHODS

## B.1 INTRODUCTION

A number of simulation methodologies were used during the course of this PhD to model the experiments and to see if theoretical predictions match up to experimental results. These methodologies include the Finite-Difference Time-Domain method (FDTD), Finite-Element Analysis method (FEA) and analytical approach. On certain occasions, one method was used over another due to the availability of software. Most of the time, however, it is the relative strength of the particular method over the others that results in its employment. Here, the strengths and weaknesses of the above modelling approaches will be described from a *user's perspective*. It would be impossible to make a comprehensive exposition of all the above methods when each of them has been the subject of such intensive study.

## B.2 FINITE-DIFFERENCE TIME-DOMAIN

FDTD as its name suggests solves the Maxwell's equations in time. An example of a software package utilising FDTD is Lumerical FDTD Solutions. Basically, when using this simulation method, the simulation unit cell is divided into a regular rectangular grid (a.k.a. staircase mesh), as shown by the left panel in Fig. B.1. Light is then injected into the system at a particular time, say $t_0$, as an electromagnetic pulse. The electromagnetic fields at each mesh point in the simulation unit cell are then solved, according to the Maxwell's equations, for each time point (e.g. $t_1$, $t_2$, $t_3$...) as the electromagnetic pulse passes through the system. Thus, each mesh point records the electromagnetic fields at that point over time.

The first advantage of the FDTD method is its broadband nature. This is because light is injected as an electromagnetic pulse which contains frequency content over a broad range for frequencies (see Section 2.6). The time-domain data recorded by each mesh point can be Fourier transformed to give broadband frequency information. The second advantage relevant to the work in this thesis is that the transient nature of the FDTD is akin to THz-TDS. Thus the results obtain in experiments can be very closely modelled using FDTD. For example, FDTD was use to replicate the experiments in Chapter 5 to obtain the $\bar{\alpha}_F^{Calc}$ values.

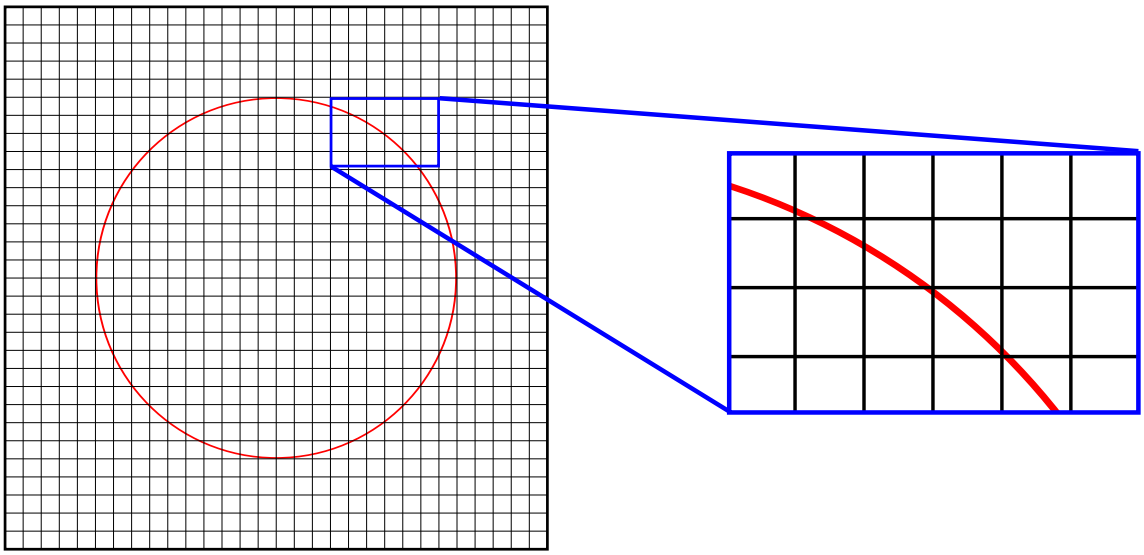


Figure B.1: (Left) An example of a staircase mesh. The simulation geometry is divided into a rectangular mesh. (Right) A closer look at the staircase mesh. As can be seen, curvature is not well described by the mesh unless when using very fine mesh.

However, the FDTD method is not without its drawbacks. First of all, the staircase mesh is unable to fully replicate geometries with curvature or slanted edges. This is demonstrated in the right panel of Fig. B.1 which takes a closer look at the edges of the red circle. As can be seen, not all the mesh points lie on the edge of the circle thus leading to the "staircase" effect where curvature is described like a staircase in the simulation since the simulation is insensitive to changes in material properties between mesh points. This problem is somewhat alleviated by innovative

meshing methods such as the conformal mesh used in Lumerical FDTD Solutions [180]. Secondly, FDTD requires the temporal response of materials to the light pulse. Hence while it is common to think of material properties in the frequency domain, for example $\mathbf{D}(\omega) = \epsilon_o \epsilon(\omega)\mathbf{E}(\omega)$, in FDTD, this would result in a convolution of $\epsilon$ and $\mathbf{E}$ in time (i.e. $\mathbf{D} = \epsilon_0 \int_{-\infty}^{t} \epsilon(t - t')\mathbf{E}(t')dt'$). The numerical calculation of this convolution is non-trivial and care as to be taken to make sure that the sampled material properties (often given in frequency) are well described in the FDTD software.

## B.3 FINITE-ELEMENT ANALYSIS

The FEA method divides the simulation geometry using triangular (2D) or tetrahedral (3D) mesh cells as can be seen in Fig. B.2. The electromagnetic fields are solved for in the frequency domain (i.e. $f_0$, $f_1$, $f_2$...). In many ways, it is natural to think of FEA as the complementary of FDTD since they work in the Fourier domains of each other. While FDTD gives broadband data, FEA calculates the fields at each frequency individually, making it slower than FDTD if many frequency points are required. Also, the transient response of the system is not readily available from FEA.

However, the use of a non-rectangular mesh in FEA allows it to fully describe curvature as can be seen in Fig. B.2 where the mesh points are always able to lie on the edges of the curved geometry. Also, solving the Maxwell's equations in the frequency domain makes the use of sampled material property data easy since, as mentioned before, material properties such as the relative permittivity can be simply multiplied to the fields in the frequency domain. This circumvents the need for the convolution operation in FDTD and ensures that the simulated material properties are exactly the same as the experimental sampled data. FEA also allows for the use of boundary conditions such as the Surface Impedance Boundary Condition (SIBC), precisely for this reason since at each frequency point the material properties are well defined.

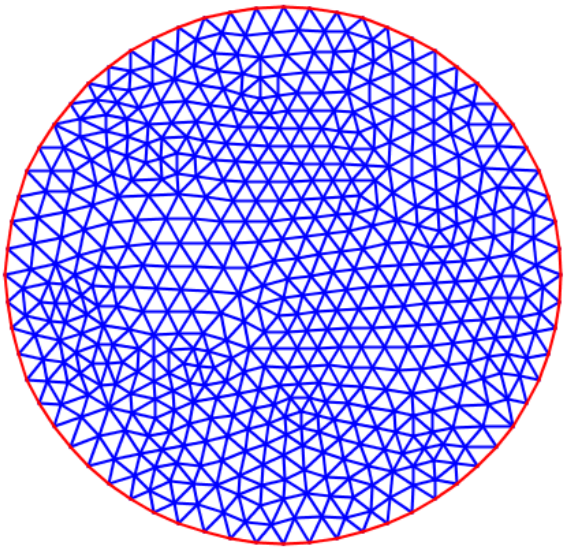


Figure B.2: Example of triangular mesh

For example, the SIBC was used to simulate the grooves when calculating the reflectivity spectrum in Chapter 4. Lastly, FEA can take into account other physical phenomena such as heat transfer and fluid motion, making it a more flexible tool if one were to consider problems such as radiation heating. An example of an FEA software package is COMSOL Multiphysics.

## B.4 ANALYTICAL APPROACH

Little needs to be said about the benefits of taking an analytical approach. The physical insights that can be gained from deriving the equations that describe even a simplified system can be worth more than many rounds of simulation. For example, the Coupled Mode Method (CMM) outlined in Section 2.5 was used to understand the general behaviour of the SPS used in Chapters 4 and 5. It gives a definite relation between all the geometrical parameters of the SPS and the SPS optical properties and allows us to come up with a rough idea of how the SPS will look like and behave without the need to go through numerous rounds of simulation.

That being said, the implementation of the analytical approach to describe the modelled system fully can be extremely tedious when compared to commercial software packages such as COMSOL Multiphysics and Lumerical FDTD Solutions. Taking CMM as an example again, in order to fully describe the SPS properties, one has to consider multiple diffraction orders and waveguide modes and their coupling to each other, as mentioned in Chapter 5. This makes the numerical calculations very involved. The problem is aggravated when the geometry in question is not regular and the electromagnetic modes in the geometry cannot be easily described such as the slanted-walled grooves of our SPS (see Fig. 4.4). Lastly, the visualisation of the electromagnetic fields might be easier using commercial software which already has built-in visualisation tools.

APPENDIX C

# ADVANCED OPTICAL MATERIALS VOL. 1 AUGUST ISSUE COVER PAGE

